UNIVERSIDADE DE LISBOA
FACULDADE DE CIÊNCIAS
DEPARTAMENTO DE GEOLOGIA

Comprehensive characterization of the Volcanic-Sedimentary Complex section at Monte das Mesas prospect and assessment of its potential to host massive sulphide mineralization

Gabriella Michel Carpinteira

Mestrado em Geologia Económica
Especialização em Prospeção Mineral

Relatório de Estágio orientado por:
António Manuel Nunes Mateus
Nelson Amável Cabaço Martins

2020

À Nossa Vó Mélia

Acknowledgements

The present work was possible thanks to ESAN, I deeply appreciate the opportunity, this partnership, particularly the granted internship, was a unique opportunity to learn and grow as a geologist.

Regarding my time during the internship, I would like to especially thank several amazing colleagues: em especial ao meu orientador Nelson Martins, pela disponibilidade e preocupação constante em especial ao longo da reclassificação de sondagens e amostragem; Ilkay Çevik for being so extraordinarily welcoming, for every constructive discussion, and of course, for all (very useful!) turkish words I still remember; ao Jorge Hilário por todo o suporte técnico, e claro, por todas as risadas; Anil Ozturk for all the support and concern; ao Pedrito (aka Pedrão!) pela lufada de ar fresco que trazias (quase) todas as semanas, sempre cheio de boa disposição e animação; e por último ao Filipe Ribeiro, por fazeres a minha vida um inferno com o teu constante bullying, obrigada também pelo constante apoio, criticas construtivas (às vezes nem tanto), e por puxares (muitas vezes à força) pela geóloga que há em mim.

Um agradecimento muito especial ao meu orientador Professor António Manuel Nunes Mateus, pela astronómica paciência, durante estes dois (muito longos) anos, mas principalmente por toda a compreensão, força e motivação que sempre me transmitiu quando mais precisava, acreditando sempre em mim, obrigada!

À Doutora Cyntia Mourão pela disponibilidade e produção de lâminas delgadas polidas e ao Doutor Pedro Rodrigues pela ajuda na obtenção, análise e processamento dos dados de química mineral.

Aos seguintes: André Cravinho, Beatriz Antunes, Diogo Ribeiro, Eduardo Jorge, Filipa Luz, Filipe Ribeiro, Ivo Martins, João Santos, José Roseiro, Manuel Silva, Maria Dias, Pedro Santos, Rita Pereira, Rita dos Santos e Samuel Ramos, prometido é devido; graças a vocês termina aqui esta etapa que tanto suor e lágrimas me custou, felizmente muitas destas últimas de alegria por estar rodeada de pessoas fantásticas como vocês! Espero ser merecedora da vossa amizade e de tudo o que por mim fizeram. Foram a minha luz ao fundo do túnel, hoje reconheço que sou uma jovem cheia de **SORTE**!

À Ana Mafalda Inácio Santos e à Inês Filipa Carvalho Pereira, pela constante preocupação, pelos desabafos e momentos de descontração, longe da geologia, obrigada por terem estado sempre presentes!

À minha benjamin button, Linda Viduedo, que à tanto me acompanha nestas jornadas, vai ser estranho fazer geologia e complicado saber das minhas tralhas sem ti daqui em diante! À Rita Pereira, por tentares meter juízo na minha cabeça, nem sempre bem-sucedida, felizmente(!), para bem de tantas risadas. E à Filipa Luz pelas palavras certas nas alturas certas, e equilíbrio que sempre me transmitiste. Obrigada meninas, pelo apoio enorme, os desabafos, a disponibilidade constante, mas sobretudo a amizade incondicional ao longo destes anos!

Aos meus boys, Diogo Ribeiro, pela confiança e encorajamento que sempre me transmitiste, pela disponibilidade enorme que sempre tiveste para as minhas dúvidas existenciais (umas mais geológicas que outras), pelas críticas (sempre!) construtivas, e claro pela amizade e carinho que nunca faltou; e Ivo *Slices* Dias Martins, o meu compincha, obrigada por me manteres mentalmente e emocionalmente sã ao longo destes anos com toda a doideira e parvoíce incessante e todos os abraços, e não, "eu não te odeio!!".

Ao meu *power couple* favorito, Beatriz Antunes e João Santos, obrigada do fundo do coração pela companhia, preocupação e cusquices que nunca faltaram, por favor adotem-me!

Ana Jesus, André Cravinho e Eduardo Soares, obrigada por estarem sempre disponíveis para discutir vetores de substituição, melts, clorites, riólitos e tantos outros bichos estranhos, e a pensar para além do óbvio.

Ao meu Fábio, foste a motivação e força que precisava para terminar, não consigo agradecer o suficiente todo o apoio, confiança, compreensão e sobretudo o enorme otimismo e boa-disposição com que me contagiaste diariamente.

Por fim, quero ainda agradecer à minha família; aos meus pais Michel e Gaspar, a quem devo tudo o que sou hoje, por acreditarem sempre em mim, aturarem as minhas neuras, falta de paciência, má disposição matinal e ritmo acelerado, sempre stressada, especialmente insuportável ao longo destes dois anos, obrigada; à pessoa mais forte e inspiradora que conheço, a minha vó Amélia, que apesar de só entender que estudo pedras e ainda hoje não saber bem o que faço, nunca faltou carinho e aquela preocupação incessante que lhe é característica; and last but not least, ao meu irmão Lilo, por me enervares ainda mais que a tese, mas estares sempre lá.

Obrigada a todos!

Resumo

A Faixa Piritosa Ibérica é uma das províncias metalogenéticas mundiais mais estudadas e a sua prospecção e exploração extensivamente documentadas. Mesmo após mais de 5000 anos de contínua exploração mineira, as reservas demonstradas continuam excepcionalmente altas, embora confinadas a alguns sectores, estando os recursos conhecidos distribuídos por mais de 90 depósitos de sulfuretos maciços. É devido à intensa e exaustiva investigação, nas mais variadas áreas da geologia, e não só na metalogenia, que os recursos e reservas da FPI continuam a aumentar, crescendo também o número de descobertas.

Aljustrel é um dos maiores depósitos de sulfuretos maciços na FPI, contendo diversos corpos mineralizados que, em conjunto, representam mais de 250 milhões de toneladas. A concessão de Monte das Mesas localiza-se a aproximadamente 5 km a WNW de Aljustrel. As sondagens previamente realizadas nesta concessão mostraram características macroscópicas promissoras, frequentemente utilizadas como guias de prospeção mineral na FPI. Estas particularidades justificaram o presente trabalho, o qual procurou estudar e examinar em detalhe as sucessões do Complexo Vulcano-sedimentar (CVS) intersectado por algumas das sondagens, avaliando o seu potencial para hospedar mineralização/sulfuretos maciços. Tendo em conta o objetivo fundamental, foram realizadas as seguintes actividades: (1) revisão bibliográfica e compilação de dados anteriores; (2) classificação e/ou re-classificação de sondagens; (3) produção de cortes geológicos (2D) interpretativos; (4) interpretação e correlação das colunas litoestratigráficas de Monte das Mesas e Aljustrel; (5) estudos petrográficos; (6) estudos de química mineral, referentes às associações mineralógicas primárias e secundárias, de modo a verificar a existência (ou não) de variações composicionais significativas e o seu significado metalogenético; (7) interpretação integrada de todos os resultados obtidos, visando a comparação direta com Aljustrel e a avaliação global do potencial de Monte das Mesas como hospedeiro de mineralização/sulfuretos maciços.

A sequência interpretada como CVS intersectado na área de Monte das Mesas é genericamente constituída por metapelitos (negros, cinzentos, verdes e roxos), rochas vulcanoclásticas de natureza variada, rochas lávicas félsicas, máficas e intermédias e rochas intrusivas máficas. Nas sondagens realizadas na zona Norte da concessão, as rochas lávicas de natureza riolítica predominam; pelo contrário, nas sondagens realizadas na zona Sul, a natureza riodacítica prevalece. As características macro- e microscópicas observadas permitem a identificação de dois centros vulcânicos distintos e independentes. No entanto, o seu alinhamento, relação espacial e cronológica permanecem desconhecidos, razão pela qual se propõem duas colunas litoestratigráficas distintas. Estas colunas não se correlacionam diretamente com as previamente propostas por vários autores para Aljustrel (*e.g.* Shermerhorn, 1971; Barriga, 1983; Relvas, 1991; Dawson e Caessa, 2003; Leitão, 2014). Com efeito, as colunas litoestratigráficas de Monte das Mesas denotam carácter predominantemente distal e sugerem a existência de um episódio extrusivo máfico precoce (CVS médio-inferior), não documentado na literatura. A inferência de dois centros vulcânicos distintos é corroborada pelos dados de FRXp, os quais sugerem que apenas as rochas do centro vulcânico intersetadas a Sul apresentam afinidade quimio-estratigráfica com os dados publicados para Aljustrel (Dawson and Caessa, 2003; Barrett, 2008; Barrett, 2009). Adicionalmente, indicam que os episódios vulcânicos intersectados na zona Norte da concessão se relacionam com magmas com afinidade toleiítica, enquanto as sucessões intersectadas na zona Sul mostram afinidade calco-alcalina.

A rochas félsicas de natureza riolítica em ambos os eixos vulcânicos (apesar de em proporções diferentes), não se relacionam através fenómenos de cristalização fracionada, nem refletem graus de diferenciação diferentes de produtos magmáticos basálticos. As diferentes assinaturas geoquímicas que

caracterizam estas litologias, evidenciadas pelas razões de elementos imóveis, sugerem diferentes graus de fusão crustal continental (quartzo-feldspática) sem misturas ou assimilações significativas. Adicionalmente, a existência de rochas riodacíticas, dacíticas e "intermédias" sugere mistura de magmas basálticos com *melts* félsicos derivados de fusão crustal, indicando um processo geodinâmico multifásico envolvendo ascenção e instalação (em diferentes níveis crustais) de magmas basálticos mantélico-derivados, variavelmente modificados por contaminação crustal (e.g. Munhá, 1983; Thiéblemont *et al*., 1998; Mitjavilla *et al*., 1997; Carvalho *et al*., 1999; Sisson *et al*., 2005; Annen *et al*., 2006; Martin-Izard *et al*., 2015, 2016; Codeço *et al*., 2018).

O adelgaçamento crustal em zona de colisão oblíqua contribuiu para o desencadeamento de processos de fusão mantélica capazes de alimentar a produção ciclíca de grandes volumes de magmas basálticos e, simultaneamente, manter um regime térmico elevado ao longo de milhões de anos. Todo este processo levou ao desenvolvimento de processos capazes de fusão parcial de crosta continental e/ou contaminação crustal de magmas basálticos que ascenderam controlados por fraturas e posteriormente se instalaram (e.g. Jesus *et al*., 2007; Ribeiro *et al*., 2007, 2010; Codeço *et al*., 2018).

As rochas lávicas de natureza félsica mostram textura microporfirítica, constituída por micro-fenocristais euédricos a subeuédricos de quartzo e feldspato *s.l.* dispersos numa matriz muito fina, também quartzo-feldspática. No entanto, a proporção entre quartzo, plagioclase e feldspato-K levaram à distinção entre riólitos, riodacitos e dacitos. O complexo vulcano-sedimentar intersetado na área Norte da concessão apresenta carácter predominantemente riolítico, enquanto o CVS intersectado pelas sondagens realizadas na zona Sul da concessão, revela caráter maioritariamente riodacítico.

A associação mineral secundária é constituída por feldspato-K, filossilicatos (sericite >> clorite), epídoto, titanite, carbonatos com quantidades acessórias de sulfuretos (*e.g.* pirite, pirrotite, esfalerite, galena e calcopirite). Ambos os centros vulcânicos mostram evidências de alteração hidrotermal nomeadamente, sericitização, cloritização, carbonatação e silicificação, em proporções relativas distintas, no entanto, sempre com intensidades baixas a moderadas. A zona Norte da concessão de Monte das Mesas manifesta cloritização mais intensa, quando comparada com a zona Sul da concessão, onde a alteração hidrotermal predominante é a sericitização.

O estudo de química mineral englobou os seguintes grupos minerais: feldspatos, piroxenas, anfíbolas, micas potássicas dioctaédricas, clorite, epídoto, zircão, titanite, carbonatos, fosfatos, óxidos e sulfuretos. Os resultados analíticos obtidos para a clorite mostram variações composicionais ao longo da solução sólida clinocloro-chamosite. As clorites ricas em Fe (mais próximas da composição ideal da chamosite) são subordinadas relativamente às clorites magnesianas (mais próximas da composição ideal do clinocloro). As clorites cujas análises mostram enriquecimento em Fe são exclusivas de duas amostras Z2#15 e MdM02#72. Na amostra MdM02#72, as clorites, apesar de raras, associam-se a (muito raros e finos) sulfuretos, nomeadamente galena e calcopirite; esta associação mineral secundária observada num metapelito fortemente silicificado, indicia alteração hidrotermal mineralizante. Por outro lado, na amostra Z2#15, as clorites ricas em Fe observam-se em diversos contextos texturais, acompanhadas por pirite e pirrotite, pelo que estes enriquecimentos relativos em Fe podem refletir a influência de gradientes químicos locais favorecendo a partição do Fe na estrutura cristalina da clorite.

De acordo com os geotermómetros da clorite de Jowett (1991), Bourdelle *et al*., (2015), and Vidal *et al*., (2001), as temperaturas de formação da clorite pré-pico metamórfico rondam os ~220-380°C, 280-470°C e 135-400°C, respetivamente. Contudo, o geotermómetro de base termodinâmica de Vidal *et al*., (2001) individualiza duas temperaturas de formação distintas 390-400°C e 135-180°C; este subgrupo com intervalo de temperatura mais baixo poderá ser interpretado como o resultado de reajustes químicos locais tardios.

As razões Mg/Fe e consequentes temperaturas de formação da clorite presente em Monte das Mesas foram comparadas com os dados referentes aos depósitos de Feitais e Gavião, disponíveis na literatura. De facto, a composição química e os valores de temperaturas de formação da clorite pré-deformação é, de modo geral, concordante com os dados referentes às clorites de alteração regional metassomática de Feitais e Gavião. Contrariamente, as amostras Z2#15 e MdM02#72 apresentam razões Mg/Fe e temperaturas compatíveis com aquelas referentes a episódio de alteração hidrotermal mineralizante.

Luz *et al*., (2019) apresenta resultados de geoquímica de metassedimentos da sondagem MdM02 estratigraficamente compatíveis com a amostra MdM02#72 que podem traduzir alteração hidrotermal: (i) potencialmente síncrona da formação de sulfuretos maciços; e/ou (ii) propagação/reativação de falhas de desligamento durante o tardi-Varisco. As clorites da amostra MdM02#72 traduzem temperaturas ligeiramente abaixo dos valores documentados para a recristalização metamórfica Varisca, podendo indicar um evento hidrotermal pré-pico metamórfico, atendendo à sua deformação. Assim, estas clorites podem sugerir a ocorrência de um evento hidrotermal mineralizante estratigraficamente acima da mineralização conhecida, Formação do Paraíso. Esta inferência baseia-se na interpretação realizada para os cortes geológicos disponíveis no capítulo VI.

Concluindo, não é possível fazer um paralelismo simples entre as sucessões do CVS de Aljustrel e Monte das Mesas, as quais denunciam contextos geológicos independente. Os dados compilados para Monte das Mesas não sugerem qualquer proximidade a um *massive sulfide feeder zone*; contudo, as evidências de alteração hidrotermal mineralizante distal devem ser futuramente investigadas.

Palavras-chave: Monte das Mesas; CVS; FPI; depósitos de sulfuretos maciços.

Abstract

The IPB ores have one of the best-documented written records of historical exploration and mining of massive sulfide deposits in the world. Even after continuous metal extraction for more than 5000 years, the demonstrated metal reserves are still exceptionally large, although confined to some sectors, and the known resources are distributed over 90 massive sulfide deposits. The sulfide ores have been continuously explored and studied and, therefore, the IPB resources and reserves are being continuously increased with new discoveries. Aljustrel is one of the largest massive sulfide mining centers in the IPB, with several orebodies combining nearly 250 million tonnes of reserves. At Monte das Mesas prospect area, located 5 km to WNW of Aljustrel, the drilled succession of the Volcanic-Sedimentary Complex (VSC) display promising macroscopic features commonly used as guides in mineral exploration surveys in the IPB. The ultimate purpose of the present study is to examine in detail and better assess these features and their intrinsic value, contributing to the assessment of the potential of Monte das Mesas area to host massive sulfide mineralization. For this purpose, the following activities were performed: logging and/or re-logging of existing cores, reproduction of 2D interpretative geological cross-sections, lithostratigraphic interpretation and correlation exercises, petrography studies, mineral chemistry analysis of primary and secondary mineral assemblages, and PXRF data analysis.

The Monte das Mesas prospect area includes two distinct and independent volcanic centers; however, their alignment, spatial and chronological relationship remains unknown. The VSC at the northern and southern sectors are represented by bimodal volcanism, comprising different types of felsic and mafic (with minor intermediate) rocks. The distinguishing macro and microscopic characteristics, between both sectors, lead to the proposal of two distinct litho-stratigraphic columns. These columns show no direct correlation with any previously suggested columns for the Aljustrel area. They denote a more distal character and include a much earlier (mid-lower VSC) extrusive mafic volcanic episode. These conclusions are supported by the PXRF data studies which also suggest that the drilled VSC succession in the northern sector is related to tholeiitic magmas, whereas the VSC succession drilled at south shows a calc-alkaline magmatic affinity. Concluding, the Monte das Mesas volcanic succession at north shows no relationship with either the succession observed at the southern sector sequence or with that documented for Aljustrel. The volcanic succession in the southern sector of Monte das Mesas shows very mild similarities with the Aljustrel chemostratigraphy.

The majority of the volcanic rocks, independently of the sampled sector of Monte das Mesas, denote mineralogical evidence of metasomatic and/or hydrothermal activity prior to the Variscan orogeny. The typical secondary mineral assemblage is composed of k-feldspar, phyllosilicates (sericite>>chlorite), epidote, carbonates and minor to trace amounts of sulfides (*e.g.* pyrite, pyrrhotite, sphalerite, galena, and chalcopyrite). According to the chlorite-based geothermometers of Jowett (1991), Bourdelle *et al*., (2015), and Vidal *et al*., (2001), pre-deformation chlorite formation temperatures are between ~220-380°C, 280-470°C and 135-400°C, respectively. The higher temperatures (~370-430º) are confined to Fe-enriched chlorites (closer to the chamosite ideal composition), which are subordinate relatively to Mg-rich chlorites (clinochlore). These *Fe*-rich chlorites are exclusively observed in two samples. In one of them, the *Fe*-rich chlorites, although very rare, come along with (also very rare and fine-grained) sulfides, namely galena and chalcopyrite; this secondary mineral assemblage, observed in a highly silicified black metapelite, represents an evidence of ore-bearing hydrothermal alteration that should be studied in detailed in the future. Also, post-deformation (non-oriented) chlorite aggregates were examined; the chlorite geothermometer of Vidal *et al*., (2001) indicate quite low temperatures (130-180°C) for some of these late-formed chlorites, which can be interpreted as local chemical readjustements.

The data obtained throughout this work indicate that no close parallelism can be made between the VSC drilled at Monte das Mesas and Aljustrel, denoting an independent geologic setting that do not preserve fingerprints of a (typical) massive sulfide feeder zone. However, the meaning and spatial distribution of distal signs of hydothermal alteration/mineralization should be futher investigated.

Key-words: Monte das Mesas; VSC; IPB; metallogeny.

Index

Acronyms and Abbreviations

Minerals

actinolite	Act	ferosilite	Fs
albite	Ab	galena	Gn
amesite	Am	hedenbergite	Hd
anorthite	An	hematite	Hm
apatite	Ap	illite	Ilt
arsenopyrite	Apy	leucophilite	Lc
augite	Aug	orthoclase	Or
biotite	Bt	phengite	Ph
calcite	Cal	plagioclase	Pl
carbonate	Cb	pyrite	Py
chalcopyrite	Ccp	pyrrhotite	Po
chamosite	Chm	pyrophyllite	Prl
chlorite	Chl	quartz	Qz
clinopyroxene	Cpx	sphalerite	Sp
diopside	Di	sudoite	Sud
enstatite	En	titanite	Ttn
epidote	Ep	wollastonite	Wo
feldspar	Fds	zircon	Zrn
feriphengite	FPh		

Geology-various

albite-phyric rhyolitic formation	ALF	Paraiso Formation	PF
atoms per unit formula	apuf	parts per million	ppm
Baixo-Alentejo Flysh Group	BAFG	Phyllite Quartzite Group	PQG
Basic Volcanic Formation	BVF	portable x-ray fluorescence	PXRF
chlorite-carbonate-pyrite Index	CCPI	quartz-feldspatic rhyolite formation	QLF
correction factor	CF	relative difference	Diff
East	E	relative standard deviation	RSD
energy-dispersive spectrometer	EDS	resistivity deep images	RDI
Iberian Pyrite Belt	IPB	South	S
Ishikawa Alteration Index	AI	Southeast	SE
long core axis	LCA	Southwest	SW
massive sulfides	MS	South Portuguese Zone	SPZ
Mértola formation	MF	volcanic hosted massive sulfide	VHMS
million tonnes	Mt	volcanic massive sulfide	VMS
North	N	Volcanic Sedimentary Complex	VSC
Northeast	NE	x-ray fluorescence	XRF
Northwest	NW	wavelength dispersion spectrometers	WDS
Ossa-Morena Zone	OMZ	weight percent	wt%

Institutional

Commission on New Minerals and Mineral Names of the International Mineralogical Association	CNMMN-IMA
Empresa de Desenvolvimento Mineiro	EDMA
Faculdade de Ciências da Universidade de Lisboa	FCUL
Serviço de Fomento Mineiro	SFM
Sociedade Mineira de Santiago	SMS

Others

exempli graia / example	*e.g.*	*sensu lato* / broad sense	*s.l.*
id est / This is	*i.e.*	*sensu strictu* / strict sense	*s.s.*

List of Figures

List of Tables

I. Introduction

Minerals and metals are essential to human life. They are required by every sector of our global economy. Without them, there would be no modern agriculture, no means of transportation, no energy production and distribution, no information and communication technologies, no military defense, no roads and other infrastructures, no satellites and even no modern medicine. Mining was one of the first mankind activities and, together with agriculture, represent the industry's mainstay of civilization. With modern times, the estimated growth of the world population from 7.3 billion in 2015 to 9.7 billion by 2050, an increase of 33%, the demand for metals increased and will continue to increase immeasurably (United Nations Population Division, 2015, median scenario). Mining must continue and grow for the foreseeable future to ensure that minerals and metals remain available to society. For this reason, mineral exploration hastening is inevitable and necessary. Global reserves and resources for some commodities are sufficient for several decades; however, the ore grades are declining and the search for mineable deposits in depth is increasing due to depletion of high-grade surface deposits. Additional resources will be identified by ongoing "greenfield exploration" and also by deeper discoveries from known mineral districts "brownfield exploration". All these discoveries will become a major new source of future mineral supply (Gandhi *et al*., 1993).

The ultimate purpose of the present study is to contribute for the assessment of the potential of Monte das Mesas area to host massive sulfide mineralization. The area is located to the WNW of Aljustrel, within the Iberian Pyrite Belt, one of the largest massive sulfide provinces of the world.

The Iberian Pyrite Belt (IPB) contains over 90 massive sulfide deposits, containing more than 1700 million tonnes (Mt), with 14.6 Mt Cu, 34.9 Mt Zn, 13.0 Mt Pb, 46,100 t Ag 880 t Au and many other metals (Inverno *et al*., 2015). The belt includes several giant and supergiant deposits such as Riotinto, Tharsis, La Zarza, Sotiel-Migollas, Aznalcóllar-Los Frailes and Masa Valverde in Spain, and Neves Corvo and Aljustrel in Portugal.

The IPB ores have one of the best documented written record of historical exploration and mining of massive sulfide deposits in the world. Even after continuous metal extraction for more than 5000 years, the demonstrated metal reserves are still exceptionally large. The sulfide ores have been continuously explored and studied and, as a consequence, the IPB resources and reserves are being continuously increased with new discoveries. Nonetheless, many questions regarding their genesis remain open, despite of many years of research (*e.g.* Straus and Madel, 1974; Carvalho, 1979; Barriga, 1983; Barriga, 1990; Relvas, 1991; Leistel *et al*., 1994; Sáez *et al.*, 1996; Leistel *et al*., 1998a; Thieblemont *et al*., 1998; Almodóvar *et al*., 1998; Tornos *et al*., 1999; Jorge, 2000; Relvas, 2000; Tornos *et al*., 2005; Sáez, *et al*., 2011). Genetic models have varied through time; currently, different styles of mineralization, reflecting different geological settings and genesis, are commonly accepted. According to some authors (Tornos *et al*., 2003; Solomon *et al*., 2004; Tornos *et al*., 2015), shale-hosted orebodies are interpreted as formed in sub-oxic to anoxic third order basins, where upwelling deep sulfur-depleted fluids mixed with modified seawater rich in biogenically reduced sulfur lead to the precipitation of the massive sulfides on the seafloor (*e.g.* Aznalcóllar-Los Frailes, Sotiel-Migollas, Valverde, Tharsis and Neves Corvo). Felsic volcanic (massive or volcaniclastic) hosted deposits (*e.g.* La Zarza, Aljustrel and Rio Tinto) have been a matter of great controversy and many authors favor a hydrothermal model whereby convective circulation of sea water through permeable footwall rocks, driven with heat from below (magma chambers, intrusions), eventually modifies sea water into hot, reduced, acidic, mineralized brine which, upon return flow to the ocean and given appropriate conditions at the site of discharge, may lead to the fast and concentrated precipitation of metal sulfides (Barriga, 1993; Tornos *et al*., 2006).

Aljustrel is one of the largest massive sulfide mining centers in the IPB, with several orebodies combining nearly 250 million tonnes of reserves. The area is excellently geologically mapped (Schermerhorn and Stanton, 1969; Freire d'Andrade and Schermerhorn, 1971) and contains large massive sulfide deposits hosted in volcanic rocks depicting clear signs of having been affected by the mineralizing fluids, thus leading to distinct hydrothermal alteration haloes (*e.g.* Barriga, 1983, Barriga and Fyfe, 1988, Relvas, 1991; Barrett *et al*., 2008; Relvas *et al*., 2011). At the Monte das Mesas prospect several lines of evidence so far gathered show that the drilled sequence of the Volcanic-Sedimentary Complex (VSC) display promising macroscopic features commonly used as guides in mineral exploration surveys in the IPB. However, many of these features must be examined in detail to better assess their intrinsic value.

From this comprehensive characterization, additional geological information is expected to improve present knowledge on the drilled VSC lithostratigraphic column, therefore supporting correlation exercises with lithostratigraphic units of other mineralized sectors of IPB, namely the sequence hosting the massive sulfide ore-bodies of Aljustrel. The intended new information is crucial to the definition of lithological/mineralogical/geochemical vectors towards mineralization.

Considering the main purpose of this work, the following activities were performed: (1) review of the literature and existing data; (2) logging and/or re-logging of existing cores; (3) schematic reproduction of 2D interpretative cross-sections; (4) lithostratigraphic interpretation and correlation; (5) petrography studies; (6) mineral chemistry studies of primary and secondary mineral assemblages to verify the existence, or not, of significant compositional variations and there metallogenetic meaning; (7) PXRF data analysis; and (8) an overall interpretation of obtained results and comparison with similar data obtain for other volcanic sequences in the IPB.

The research activities were performed under the scope of a Confidentially Agreement established with ESANMET and so only a summary of the most relevant data are presented in this report.

II. Geological Setting

II.1.Regional Geology

The Monte das Mesas prospect covers an area of ≈ 29715 km^2 to the west of the known massive sulfide deposits of Aljustrel/Gavião in the Iberian Pyrite Belt (IPB), part of the South Portuguese Zone (SPZ), *i.e.* the southernmost paleogeographic and paleotectonic unit of the Iberian Variscides (*e.g.* Ribeiro and Silva 1983; Ribeiro *et al*., 1990; Silva and Pereira, 2004). The southern and western contacts of SPZ with Meso-Cenozoic sedimentary (mostly marine) sequences correspond to an angular discordance or are outlined by fault zones; the northwest and southeast contacts are covered by sedimentary deposits that infill the Sado and Guadalquivir Cenozoic basins, respectively (Oliveira *et al*., 2013). The northern contact between SPZ and Ossa-Morena Zone (OMZ) follows an orogenic suture decorated by exotic terrains (*e.g.* Ribeiro *et al*., 1990; Eden *et al*., 1991; Fonseca and Ribeiro, 1993; Quesada *et al*., 1994), namely the Ophiolite Complex of Beja-Acebuches and the Pulo do Lobo Terrain (which represents an accretionary prism).

The SPZ is structurally subdivided into two main domains, from northeast to the southwest: the Iberian Pyrite Belt and the SW Portuguese domain (Oliveira, 1990; Eden *et al*., 1991; Oliveira *et al*., 2006; Oliveira *et al*., 2013). The outcropping SPZ rocks are dated from middle Devonian to late Carboniferous (*e.g.* Leistel *et al*., 1998; Oliveira *et al*., 2013).

II.1.1. Iberian Pyrite Belt

The IPB is approximately 250 km long, from Sevilla (Spain) to Marateca (Portugal) and 25 to 70 km wide (Leistel *et al*., 1998). It displays an open curvature along its extension with orientation close to E-W in the Spanish territory and NW-SE in the Portuguese domain. According to conventional works, the deformation intensity tends to increase towards north; however, the accommodation of deformation is quite heterogeneous, depending mostly on the contrasting rheologic behavior of different rock types and local spatial arrangements, making the IPB subdivision in two branches (north and south) based only in deformation intensity debatable (Silva *et al*., 1990).

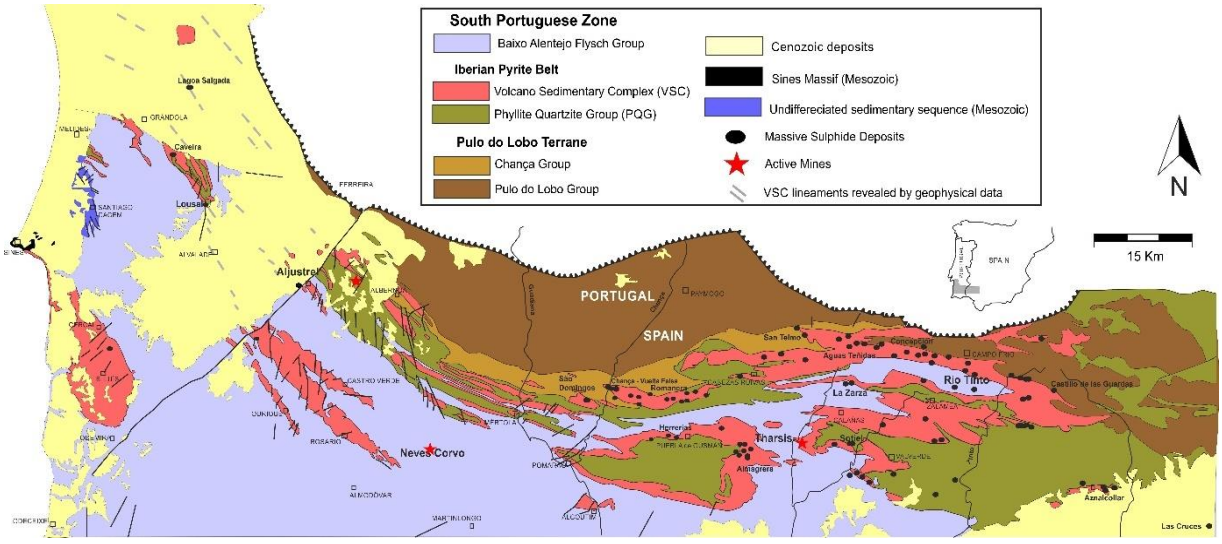

Figure II.1 Simplified geological map of the Iberian Pyrite Belt (Luz *et al*., 2019).

II.1.2. Stratigraphy

The IPB is composed of three major lithostratigraphic units: the Phyllite Quartzite Group (PQG), the Volcanic Sedimentary Complex (VSC) and the Baixo-Alentejo Flysch Group (BAFG) (*e.g.* Schermerhorn, 1971; Oliveira, 1983; Oliveira, 1990):

Phyllite Quartzite Group (PQG)

The PQG is the lowermost lithostratigraphic unit in IPB dated of mid Givetian to mid Famennian (mid to late Devonian) by ammonoids, conodonts, and palynomorphs (*e.g.* Boogaard and Schermerhorn, 1981; Oliveira *et al*, 2013). It forms a detrital succession composed mostly of dark phyllites, quartzites, metaconglomerates and rare metalimestone lenses and nodules at the top (Oliveira, 1990) Inverno *et al*, 2015). The PQG base is still not defined and its thickness spreads for many hundreds of meters (Oliveira, 1983; Silva *et al*., 1990; Oliveira *et al*., 2013).

The PQG shows notable differences between both IPB branches. In the northern branch of IPB, the PQG successions are organized in allochthonous tectonic sheets and the primary sandstones (now quartzites) are commonly disrupted in lenses and blocks of variable size (Oliveira 1990; Inverno *et al*., 2015). In the southern branch of IPB, the PQG is organized in very thick successions where the quartz-rich sandstones are increasingly more abundant to the top. A decametric unit composed of dark shales with intercalations of limestone lenses and nodules is distinctive of PQG forming the IPB southern branch (Inverno *et al*., 2015).

Volcanic Sedimentary Complex (VSC)

The VSC has been dated by several methods, such as: (i) rare conodonts and well-preserved assemblages of palynomorphs in some pelite layers (*e.g.* Pereira *et al*., 2014); (ii) U/Pb in zircons from different volcanic rocks (*e.g.* Barrie *et al*., 2002; Rosa *et al*., 2009); and (iii) Re/Os and Pb/Pb in sulfide ores (*e.g.* Mathur *et al*., 1999; Munhá *et al*., 2005). The obtained results all converge to ages around 360-340 Ma, *i.e.* late Famennian (late Devonian) to late Visean (middle Carboniferous). The VSC thickness varies across the basin and can reach 1300 m near volcanic centers.

The VSC is composed of intercalations between metapelites, thin-bedded metasiltstones and thin-bedded metavolcaniclastic rocks that resulted from fragmentation and sedimentary reworking (of variable extent) of several intrusive and extrusive volcanic rocks (*e.g.* Oliveira *et al*., 2013). The preponderance of sedimentary (siliciclastic) over volcanic-derived material depends on the distance to a volcanic center. Near volcanic centers, volcanic rocks will prevail over siliciclastic rocks, recording the importance of episodic magmatic activity to the build-up of local stratigraphic columns.

At a regional scale, at least three felsic and two mafic volcanic episodes are distinguished (Sáez *et al*., 1999). The felsic volcanic rocks (rhyolites, rhyodacites, and dacites) represent about 70% of the accessible occurrences (outcrops and drill-holes), relatively to mafic rocks (basalts, spilites, and dolerites) and minor intermediate ("andesite-like") rock types (*e.g.* Schermerhorn 1971; Munhá, 1981). The bimodal character of volcanism is not related by differentiation: whereas basaltic lavas are related to heterogeneous mantle sources, felsic volcanic rocks have a calc-alkaline affinity due to partial melting of the crust, most conceivable induced by high geothermal gradients related to the rise of mafic magmas; this is confirmed by isotopic data (Rb/Sr, Sm/Nd and Pb) and other information independently gathered (*e.g.* Thieblemont *et al*., 1994, 1998; Mitjavila *et al*., 1997; Munhá, 1981; Munhá, 1983a; Carvalho *et al*., 1999; Codeço *et al*., 2018).

The metapelites present in the upper part of VSC are composed of thick intercalations between purple, green and grey shales that occur at the same stratigraphic position throughout the IPB being considered a marker for lateral correlation. Jaspers and cherts are also present, interfingered with the former rock types (*e.g.* Oliveira *et al.*, 2013; Luz *et al*., 2019).

When present, the massive sulfides and related hydrothermal systems typically: (i) occur amongst felsic rocks (often forming the base sequences) and a relatively thin layer of jasper/carbonates (at top), usually associated with black shales (*e.g.* Leca *et al*., 1983); or (ii) are hosted in piles of felsic volcanic facies that commonly include thin pelitic layers (*e.g.* Leistel *et al*., 1997). No massive sulfides are found lying directly on the basic rocks (with the exception of S. Domingos), although these facies are in places cut by feeder stockworks (Leistel *et al*., 1997).

The lithostratigraphic relation between the ore bodies and the hosting rocks differ among the known deposits of IPB. Very significant syn-sedimentary tectonic movements shifted some of these ore bodies away from where they were formed. Carvalho (1979), classified these massive sulfide lenses as autochthonous, transitional and allochthonous (Lousal, Sotiel and Tharsis, respectively); only autochthonous masses are directly above their feeder zone, whereas the allochthonous ones are positioned away from the stockwork; all intermediate situations are possible and expected.

Baixo Alentejo Flysch Group (BAFG) or Post-volcanic lower-Carboniferous Group (Culm group)

The BAFG, also known as Culm, is a thick (over 1500 m) marine sedimentary sequence of flysch type and dated of late Carboniferous (Pereira *et al*. 2008) that represents the infill of a foreland basin with multiple sources along the IPB and the OMZ (*e.g.* Oliveira *et al*., 1979; Silva *et al*., 1990; Jorge *et al*., 2012).

The BAFG is sub-divided in 3 different Formations: (i) Mértola, Late Visean in age, composed of (centimetric a metric) intercalations between metagraywackes, metapelites, impure quartzites, metasiltstones, and metaconglomerates; (ii) Mira, Late Serpukhovian to Bashkirian in age, composed of finely laminated turbidites with occasionally richer successions in metagraywackes and rare metaconglomerates; and (iii) Brejeira, dated from Middle-upper Bashkirian to Early Moscovian, with impure quartzites, metaquartzgreywacke and metapelite intercalations (Oliveira, 1990; Oliveira *et al*., 2015). The deposition of these sedimentary sequences is concurrent of the tectonic inversion of the basin occurred in late Paleozoic times, thus related to the Variscan orogeny progression (after the completion of the oblique continental collision; see below).

II.1.3. Tectonics

The IPB is interpreted as a group of pull-apart basins generated by left-lateral strike-slip faulting of a stretched continental margin, triggered by the oblique collision (Silva *et al.*, 1990; Jesus *et al*., 2007; Ribeiro *et al*., 2007). These first-order marine basins were segmented by east-west tectonics, originating second-order basins, where E-W to NE-SW local-scale faults might have delimited sub-basins, creating half-grabens geometries and differential subsidence (*e.g.* Oliveira, 1990; Tornos *et al*., 2005). The early stages of volcanic development (and associated massive sulfide deposits) are concurrent of the basins compartmentation, depending on each sub-basins evolution (*e.g.* Sáez *et al*., 1999).

The compressive pulses, roughly oriented NE-SW (with variable magnitude in time), originated asymmetric folds verging to SW, where the schistosity often transposes the bedding in the short limbs, producing an imbricated “thin-skinned” complex of stacked thrust faults, detached from the pre-

Devonian basement, resembling a "piggy-back" type sequence (Ribeiro and Silva, 1983; Silva *et al*., 1990; Sáez *et al*., 1999).

Three main stages of deformation have been described. D1 (Upper Visean) was, by far, the one that most contributed to IPB's current arrangement, whereas D2 (Middle to Upper Muscovian) and D3 slightly modified the previous structures (*e.g.* Schermerhorn, 1971;-Sáez *et al*., 1999).

The early stages of D1 generated large-lying folds locally followed by sub-horizontal sin-sedimentary low angle thrusts (Silva, 1983); later, these structures were squeezed and folded, respectively, along with the development of a penetrative schistosity, creating folds always verging SW (Silva, 1989; Silva *et al*., 1990). Lately, several strike-slip fault systems were originated or reactivated. These fault systems run approximately NNW-SSE to N-S (dextral) and NE-SW (sinistral), with large offsets, up to 5 km (*e.g.* Carvalho *et al*., 1979); the N-S oriented fault zones are quite relevant in Aljustrel, cutting the main sulfide ore bodies.

Concurrent with deformation, low grade (40-50°C/km) isochemical regional metamorphism affected all the IPB rock successions, resulting in different metamorphic facies increasing to the north: zeolitic, prehnite-pumpellyite and greenschist (*e.g.* Schermerhorn, 1975; Munhá, 1976, 1983).

II.1.4. Hydrothermal Alteration

The hydrothermal alteration haloes are easier to detect than the ore bodies, mostly due to its much larger volume and, therefore, very useful in the search for new deposits. These alteration haloes are controlled by physicochemical parameters related to the host rock composition, temperature, water/rock ratio, etc. Two different alteration types coexist:

(1) At a regional scale, low-temperature seawater metasomatism affected mafic (*e.g.* basalts) and felsic (*e.g.* rhyolites) rocks, converting them into "spilites" and "quartz keratophyres", respectively. In mafic rocks, this process produces secondary mineral assemblages that include chlorite, carbonates, epidote, albite and actinolite, involving extensive Na-K exchange, hydration, oxidation and carbonatization (*e.g.* Munhá, 1990). In felsic rocks, the most common metasomatic processes are albitization, sericitization, chloritization and silicification (Munhá and Kerrich 1980; Barriga and Kerrich 1981, 1984; Barriga, 1983, 1990). Metasediments are also affected by these low-temperature processes, but the macroscopic recognition of effects due to their progression is not so easy due to the lower chemical contrast between the intervening fluids and siliciclastic sediments; nonetheless, at micro-scale, several mineral transformations or neoformations can be ascribed to this early seawater metasomatism (*e.g.* Luz *et al*., 2019).

(2) At a local scale, higher-temperature hydrothermal alteration related to the development of orebodies can be recognized (*e.g.* Inverno *et al*., 2015; Sáez *et al.*, 1995; Munhá, 1990). The local ore-zone alteration results from the rise of metalliferous hydrothermal fluids, mainly derived from modified seawater. The convective regime that results from the circulation of seawater through the permeable rocks, driven energetically by geothermal gradients (thermal flow in the oceanic crust, emplacement of intrusive and extrusive igneous rocks), warms and chemically transforms the seawater, which gradually becomes reduced, slightly acidic and enriched in metals as a result of leaching processes affecting crustal rocks. When these modified fluids rise, they become a powerful solubilizing and transporting agent of metals (*e.g.* Franklin *et al*., 1981; Barriga, 1983). The convection occurs through the underlying permeable rocks, from the VSC to the PQG. Some authors advocate that the commonly reduced

thickness presented by the VSC (less than 600 m) may imply the PQG as the main source of the metals (Barriga, 1983; Tornos *et al*., 2005; Jorge, 2000; Jorge *et al*., 2007).

The interaction between the metal-rich modified seawater and the host-rock generates several secondary mineralogical assemblages. These mineral assemblages develop alteration haloes, which typically produce a concentric pattern around the hydrothermal feeding zone (stockwork). The most common secondary mineral assemblages form two distinct haloes (Carvalho, 1976; Barriga 1983; Toscano *et al*., 1993; Sáez, 1996, 1999):

(1) "Alteration type 1", generally featured by chlorite + quartz + sericite + pyrite (± carbonates ± chalcopyrite ± sphalerite ± galena ± estannite) and representing the core of the hydrothermal system. Characterized by an extreme leaching of the Ca, Na and K and relative enrichments in Al, Fe and Mg

(2) "Alteration type 2", generally typified by sericite + quartz + pyrite + chlorite (± carbonates ± chalcopyrite) and indicating a leaching of Na and Ca coupled by significant enrichments in K and Al.

In Aljustrel (particularly at the Gavião deposit), hydrothermal zoning is also marked by a progressive decrease of the Mg/(Mg+Fe) ratio in chlorites, which is minimum in the inner, high-grade chloritic zones (Barriga 1983; Relvas, 1991; Ruiz de Almodóvar *et al.*, 1994). The change of phyllosilicate compositions, also reflecting differences in alteration intensities, is frequently used as a geochemical proxy. For example, according to some authors, Na-sericites are characteristic of ultra-peripheral zones, occurring more than 1 km away from the sulfide ore bodies, with an overall removal of alkalis from the internal zone, fixing K(+Ba) in the intermediate zone documented by the presence of Ba-rich sericites, also called "alteration type 3" (*e.g.* Relvas 1991; Massano *et al*., 1991; Barriga and Relvas 1993; Leistel *et al*., 1994).

The sulfide assemblage consists predominantly of pyrite, sphalerite, galena and chalcopyrite, with tetrahedrite-tenantite, pyrrhotite, cassiterite as accessory phases along with trace amounts of electrum (*e.g.* Leistel *et al*., 1998).

II.2. Local Geology

The Monte das Mesas prospect, covering an area of 29715 km^2, is located 5 km to the WNW of the Aljustrel town. Although no massive sulfide deposits have been intersected to date, the geological setting, placed to the NW extension of the volcanic axes hosting several massive sulfide deposits, confer great potential to the area, considering the offset imposed by the Messejana strike-slip fault zone. For this reason, it is plausible to tentatively frame the Monte das Mesas geological setting with the Aljustrel area.

Throughout this brief sub-chapter, the main structural and litho-stratigraphic features of the area of Aljustrel will be highlighted; for more detailed information the reader should check the works of Schermerhorn and Stanton, 1969; Ribeiro and Silva, 1983; Barriga, 1983; Relvas, 1991; Relvas *et al*., 2011.

At Aljustrel, six main ore bodies occur within an area of 5x2 km: Feitais, Estação, Algares, São João, Moinho and Gavião. Several estimations for known resources (of massive sulfide ore) were attempted (*e.g.* Inverno *et al*., 2008) totaling 190 million metric tons (Mt) (not considering stockwork ores) and

grading from 45 to 47 wt% S, 38 to 41 wt% Fe, 3.4 wt% Zn, 1.2 wt% Pb, 0.8 wt% Cu, 36 g/t Ag, and 1 g/t Au; Barrett (2009) reports at least 230 Mt of pyrite-rich massive sulfides.

The Aljustrel area consists of an elongated anticlinoral structure with general orientation N145º, in which the VSC forms a "semi-klippe" detached and stacked from NE to SW, showing tight isoclinal folds over the Baixo Alentejo Flysch Group. The ore bodies lie on the limbs of four SW-verging second-order folds: (i) Feitais anticline, (ii) Central anticline, (iii) S. João sincline, and (iv) the SW anticline. The north-east, south and south-west boundaries contact with turbidites of the Flysch Group, hidden by the Cenozoic cover, whereas the north-west boundary is crisscrossed and displaced by the Messejana Fault (Schermerhorn and Stanton, 1969).

The Aljustrel stratigraphy is very similar to the generic IPB mentioned earlier, although recording a large textural and mineralogical heterogeneity due mostly to secondary processes (as regional metasomatism and superimposed hydrothermal alteration). The PQG was not so far intersected in Aljustrel, being the VSC (occupying the center of the anticlines) the base of Aljustrel lithostratigraphy column. The VSC includes a relatively thin (<600 m) succession of metavolcanic rocks covered by metasediments and a discontinuous layer of meta-jaspes/cherts that together form the Paraíso Formation. This unit underlies the Flysch Group sequence. Barrie *et al*. (2002) dated the hydrothermally altered green felsic volcaniclastic host rocks from the Algares ore body, and the yielded U-Pb zircon ages range from 349.8 ± 0.9 to 356.2 ± 0.7 Ma.

Two different strike-slip fault families coexist in the Aljustrel area: (1) running ENE-WSW to E-W (sinistral), producing relatively small offsets, and (2) running N-S to NNE-SSW (dextral) and dipping 70-80ºSE, comprising considerable extension and offsets, displaying a very small vertical (normal) component (Ribeiro and Silva, 1983).

The Gavião deposit is composed of two ore bodies. The NE ore body is interpreted as the extension of the S.João-Moinho-Algares ore bodies, lying on the reverse limb of the Central anticline but in the same stratigraphic position, whereas the SW orebody has no known continuation to the south of the Messejana fault; furthermore, Gavião portrays the highest average copper grade of the whole Aljustrel area (1.5% Cu; 4.0% Zn; 1.6% Pb; 0.9 g/t Au, 48.3 g/t Ag; Relvas *et al*., (2011), making Monte das Mesas prospect area significantly interesting.

III. Methodology

This section aims to portray the various stages of sample collection and preparation, and further analytical work carried out during the internship, thus providing the data here presented and discussed.

III.1. Drill core re-logging

A total of 8 drill cores were selected for re-logging and sampling: Z1, Z2, MM01, MM02, MM05, MdM01, MdM02 and MdM05. These drillings form two distinct clusters: (i) near the NW corner of the Monte das Mesas prospect area (MM05, MdM01 and MdM02), and (ii) close to the SE corner (Z1, Z2, MM01, MM02 and MdM05).

The selection was carried out considering the main goals of this work, in particular the spatial distribution of the preexisting drill-holes and their previous logging. The data obtained served as reference for the preparation and validation of 2D geological models and forecasting the goals of the next stage – sampling.

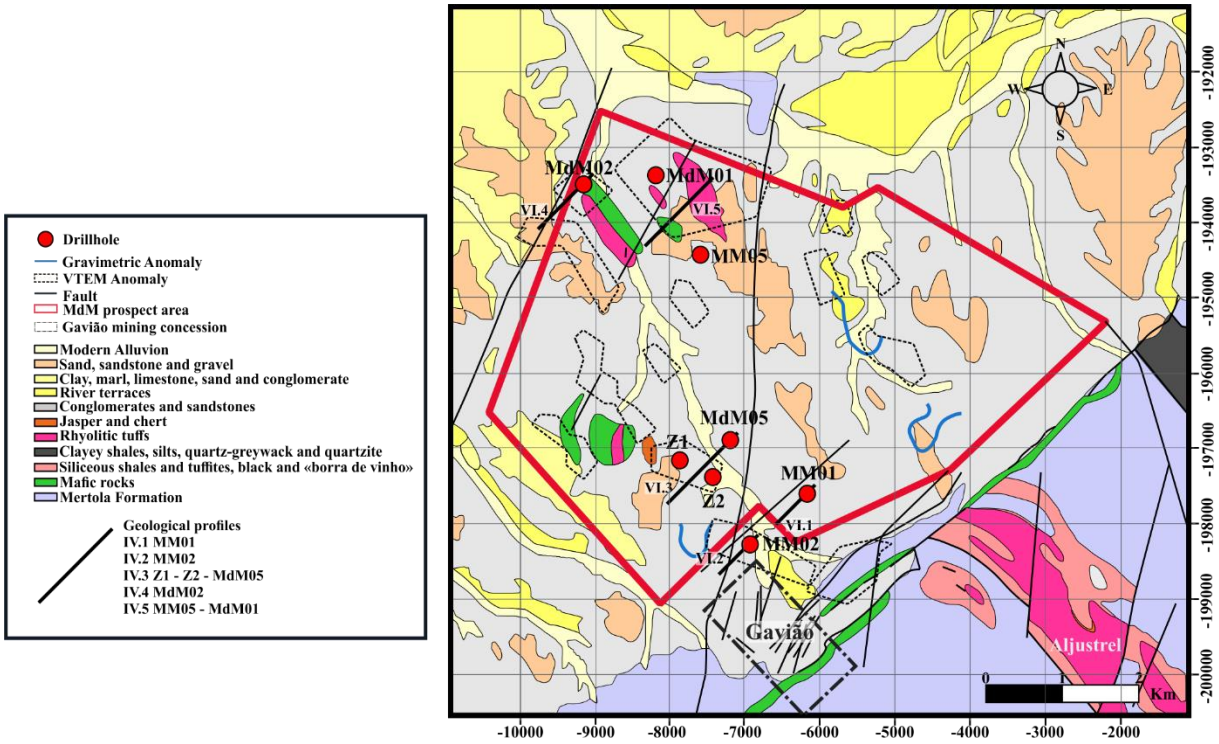

Figure III.1 Adapted simplified geological map of Monte das Mesas prospect area (provided by ESANMET)

III.2. Sampling

To deepen the information obtained from core re-logging, the main lithologies were sampled in different sections and frameworks (representing macroscopically distinct hydrothermal alteration features) for petrography and mineral chemistry studies. A total of 80 samples were collected. The main criteria used during this stage were as follows:

a. Development of a mineralogical and geochemical database for the VSC sequence at the Monte das Mesas area;

b. Characterize, on a petrographic and mineralogical basis, the different rock types composing the VSC, giving special attention to sections affected by hydrothermal alteration processes;

c. Describe the most critical mineral phases that can potentially be used as fingerprints or footprints to mineralizing systems.

Five different lithologic groups were sampled: (black, grey, green and purple) metapelites, felsic volcaniclastics, rhyolitic lavas, extrusive mafic rocks (spilites) and intrusive mafic/intermediate rocks.

III.3. Laboratory sample processing

After detailed macroscopic characterization and photographic recording of textural and mineralogical features of interest, and considering the extensive batch of samples collected, it was necessary to make a careful selection of samples to produce slabs, ensuring spatial facies representativeness.

The laboratory processing consisted of several phases:

1. Cutting the selected samples in centimetric rectangular slabs, using small diamond saws;

2. Gluing of the slab face containing the aspects of interest into an un-polished glass slice, using a two-part epoxy resin with high refractive index and mechanic resistance;

3. Removing the excess rock from the slab, leaving a thickness of approximately 0.5 mm, using a precision saw;

4. Grinding of the glued chips until they reach a 40-45 μm thickness, using an automatic lapping equipment;

5. Polishing the rock surface, with ever finer diamond pastes, until a uniformly smooth plane is obtained with approximately 30 μm.

The laboratory processing of the selected samples resulted in the production of 40 polished thin-sections for subsequent petrography further complemented with quantitative chemical mineral analyses with electron microprobe. All these procedures were carried out at the Geology Department of the Faculty of Sciences of the University of Lisbon (FCUL).

III.4. Petrography

Petrography was performed with transmitted and reflected light microscopy aiming a detailed characterization of mineral assemblages (primary and secondary phases) and their textural arrangements in rock types forming different sections of the VSC at Monte das Mesas. Additionally, the petrography inspection intended to differentiate the oceanic metasomatism effects from those ascribed to changes produced by metal-fertile hydrothermal alteration synchronous of sulfide deposition.

This stage resulted in the production of petrographic and photomicrographic summary descriptions of each lithological group. On the basis of petrography, several samples were selected to be used for the subsequent mineral chemistry studies.

III.5. Mineral Chemistry – Electron Probe Micro-Analyser (EPMA)

Out of the 40 thin-sections examined, 10 were selected for detailed analytical studies with electron microprobe, considering both textural and mineralogical variability and alteration intensity displayed by each rock type.

The selected polished thin sections were previously covered by a 20 nm thick carbon coating. This stage was also carried at FCUL, in the Electron Microprobe Lab. The equipment used was a JEOL JXA 8200 Superprobe, this model includes a power dispersion spectrometer with four wavelength dispersion spectrometers (WDS), a secondary and back-scattered electron detector, a coupled energy-dispersive spectrometer (EDS), and six crystals (LIF, LIFH, PET, PETH, TAP and LDED2).

The mineral chemistry study was carried out aiming:

a) clarification or confirmation of pending mineral identifications impossible to complete during petrography given the extremely fine grain size of some mineral phases;

b) characterization of accessory mineral phases and/or textural arrangements only resolvable under high magnification/resolution; and

c) assessment of compositional variations showed by (primary/secondary and main/accessory) mineral phases found in different textural arrangements, but most importantly in different generations of the same particular mineral phase, particularly critical regarding phyllosilicates.

Efforts were made to ensure the statistical representativeness of the analytical results obtained for each mineral phase. Also worth mentioning, the data quality strongly depends on the previous sample preparation and the quality of the standardization and calibration.

The detection limits and analytical condition of the microprobe, for each mineral phase, can be found in Appendix I.

III.6. PXRF data analysis

Pervasive hydrothermal alteration associated with massive sulfide deposits make visual lithologic correlations particularly difficult; therefore, portable x-ray fluorescence (PXRF) data, provided by ESANMET, was used to better understand the geochemical spread that characterizes the different volcanic units present in Monte das Mesas, in particular, the felsic volcanic units, and their (possible) correlation with the units described and characterized in Aljustrel mine center (Barrett, 1999, 2008, 2009).

Portable XRF guns offer many advantages, representing a very common and useful tool in the mining and exploration industry. They are lightweight, completely portable and non-destructive, providing a good analytical range and delivering results extremely fast (in seconds), nowadays, with excellent

accuracy. Nevertheless, and as any laboratory equipment or procedure, several rules and precautions should always be respected, including quality control and quantification procedures.

The data present in this work was provided by Jorge Hilário (ESANMET) and obtained with an Olympus Corp. Vanta C-series with Rh X-Ray tube, 40kV maximum voltage and a Silicon Drift Detector. To ensure acceptable analytical data quality, measurements in reference materials were reviewed and a systematic comparison was conducted between results gathered with the equipment and results provided by conventional analytical methods in an independent laboratory. The latter approach serves the same purpose as quality control and quantification with reference materials but also allows for the creation of multi-elemental correction factors. The quality and quantification control were yielded by Filipe Ribeiro (ESANMET), proving that PXRF produces high quality (although incomplete) whole-rock geochemical analyses and establishing correction factors for the relevant multi-element spectrum in felsic volcanic rocks, as they are considered the most relevant lithology in the present geological framework (Appendix II).

The Relative Standard Deviation (%RSD) is a precision quantification parameter and the Relative Difference (%Diff) an accuracy quantification parameter.

$$\%RSD = \frac{\sigma_i}{\bar{x}_i} \times 100 \qquad \text{Equation 1}$$

$$\%Diff = \frac{C_{i\,PXRF} - C_{i\,Lab}}{C_{i\,Lab}} \times 100 \qquad \text{Equation 2}$$

σ: standard deviation; $\bar{x}$: mean; C: concentration; i: measured element; $PXRF$: analysis measured by the portable XRF gun; Lab: analysis measured by an independent laboratory.

The difference between the PXRF $\%Diff$ analyses and the reported composition never exceeds 5% and the $\%RSD$ is less than 10% in most cases. These values are considered excellent for this type of equipment. The highest $\%Diff$ and $\%RSD$ correspond to Mg, whose atomic weight lies within the threshold detection limit, making these values less reliable. On the other hand, elements like Fe, Cr, and Ni are diluted due to overestimation of elements such as Al, Mg, S, K, Ca, Cu, and W. The latter group of elements do not exist in the reference sample and its detection can be due to contamination, namely rock dust (Al, Mg, K, Ca and S are major elements in most of the studied rocks) or discontinuous metal coatings from the blades used to cut the rock samples (case of W and Cu).

In order to assess and balance the previous quality control, 81 samples of different lithologies were sent to an independent laboratory (ALS Geochemistry Seville) for further comparison. The analytical packages ordered were ME-ICP6 and ME-MS61, for major and minor elements, respectively.

The comparison with the laboratory analyses was performed using the %Diff median in each element. Once again, V, Cr, and Ni show extremely high %Diff in rhyolitic rocks. Rhyolites are highly differentiated rocks, with lower multi-element diversity (in comparison with mafic rocks), being characterized by very low concentrations in the concerned elements, lower than the PXRF detection limits, as mention above (Appendix III).

Subsequently, the respective correction factors were defined, for felsic rocks, since they are considered the most relevant lithology in the current mineral exploration context. The correction factors were calculated using Equation 3 (Appendix III)

$$CF_i = \frac{1}{(100 - \%Diff_i)} \qquad \text{Equation 3}$$

IV. Drill core re-logging

This chapter summarizes the overall re-logging sequence of all 8 drill-cores, describing all intersected geological units, emphasizing lithological contrasts, textures and hydrothermal alteration. In general, the observation of these drill-cores evidenced a repetition of the lithostratigraphic sequences of tectonic nature.

IV.1. MM01

The drill-hole MM01 was designed by EDM and granted to the company RODIO which in turn subcontracted in 2012 the IN SITU TESTING to perform it. This drill-hole, planned with azimuth N225º and dip -60º on coordinates (ETRS89 PT-TM06) X: -6161; Y: -197560, was proposed to investigate a gravimetric (and geochemical) anomaly located ≈300 meters deep near Rio de Moinhos, approximately 3.5 km to the North of the Gavião deposit and to the NE of the extensive Milhouros gravimetric anomaly. Drilling was ceased after 594 meters due to technical reasons (Relatório Atividades 2º Semestre 2013, Monte das Mesas).

The first ~300 meters were not re-logged for logistical reasons; however, previous logging information states the presence of Cenozoic detrital sedimentary deposits (74 m) over a metasedimentary sequence ascribed to the Mértola Formation (BAFG) and composed of fine- to medium-grained graywackes intercalated or inter-fingered with black to grey colored metapelites. Recurrently, S_0 is transposed by S_1, ~80° of long core axis (LCA) and presents normal polarity. The contact with black metapelites belonging to the beneath sequence (geometrically and stratigraphically below) is tectonic, interpreted as a (reactivated) shear zone indicated by different structures (that record the accommodation of significant deformation), including late-developed, irregular milky quartz veins.

Between ~438 and ~468 meters the drilling crossed a metasedimentary succession with normal polarity criteria and composed of black metapelites displaying rare quartz nodules, domains slightly enriched in pyrite (usually ~S_1), and "graphitic-like" shale layers (458m) often bearing levels comprising a fine-grained sandy component. This succession is interpreted as part of the VSC and palynological studies carried out in two samples picked at 446.9 m and 465.5 m provided a mid to late Visean age (Projecto Monte das Mesas, Aljustrel, 4º Relatório semestral de Actividades, 1º Semestre de 2014). Several sections of the metasedimentary succession preserve evidence of heterogeneous strain accommodation, but the one between ~457 and ~458 meters show structural features allowing the inference of a shear zone.

A fault zone at ~468 meters puts in contact the aforementioned succession (dominated by black metapelites) with a different metasedimentary sequence of prevalent green-grey colored metapelites. This deeper metapelite sequence includes several intercalations of silt-like sediments and/or of fine-grained volcanic-derived products; if so, some levels of tuffaceous metapelites should be considered in the facies succession. Towards depth, the green-grey metapelites gradually grade to purple tints. At 543.2 m palynological studies carried out in one sample picked at 543.2 m provided a mid to late Visean age, conforming this succession as CVS, as interpreted before (Projecto Monte das Mesas, Aljustrel, 4º Relatório semestral de Actividades, 1º Semestre de 2014). At ca. 548 m, after another fault zone, several gradual interleaves between green, black and purple metapelites can be observed, as well as thinner and less frequent layers documenting the accumulation of possible volcanic-derived (distal) products. Accessory amounts of tiny galena grains were observed in quartz veins affecting the metapelite rocks at ca. 572 m. Polarity is usually normal and S_0 transposed by S_1 ~85° (LCA).

The main target indicated by geophysical data is located at depths close to 300 m, and can be explained by some features characterizing the drilled black metapelite sequence, namely the "graphitic-like" shale layers often including disseminations of fine-grained (and inter-connected) pyrite. However, following the integrative interpretation reported in the Relatório Atividades 2º Semestre 2013, Monte das Mesas, a deeper target should be investigated, closer to the upper zone of the rhyolitic volcanic rocks expectably below the drilled metapelite succession; this work hypothesis was not tested so far.

IV.2. MM02

The MM02 drill-hole was projected to inspect a geophysical and geochemical anomaly targeted around 320 meters deep to the NW extension of the Gavião anticline. The drilling was performed at coordinates (-6935, -198314) having azimuth 223° and -60° dip. The drilling work was granted to the company RODIO which in turn subcontracted IN SITU TESTING (Relatório Atividades 2º Semestre 2013, Monte das Mesas).

The first ~150 meters were not re-logged for logistic reasons, but previous logging information states the presence of Cenozoic detrital sedimentary deposits (till ~97 m) followed by a metasedimentary sequence composed of alternating meta-graywackes and metapelites. Between ~150 to ~162 meters, the drilling crossed medium- to coarse-grained meta-graywackes intercalated or inter-fingered with black to grey colored metapelites, forming a succession interpreted as Mértola Formation (BAFG). Recurrently, S_0 is transposed by S_1, oriented ~45° of long core axis (LCA). The contact with black metapelites belonging to the beneath sequence (geometrically and stratigraphically below) is tectonic, interpreted as a fault zone (~164 meters) subjected to recurring reactivation and where products of intense crushing are accompanied by fault gouge, both affecting irregular late quartz veins and an early-developed fault breccia. Note that secondary, euhedral pyrite is frequent in these fault rocks.

Between ~164 to ~220 meters, the drilling crossed a metasedimentary sequence composed of black metapelites bearing a fine-grained sandy component; usually, polarity is normal, but some sections preserve criteria of inverse polarity. Fine-grained pyrite, to a great extent distributed in S_1 planes (transposing S_0), is quite common. From ~205 to ~207 meters, several rhythmic intercalations between minor meta-graywacke and black metapelites occur; although pyrite is disseminated throughout all this section, its abundance is particularly significant along the contact between some meta-graywacke and black metapelite layers, roughly following S_0 ~40-45°. This section is interpreted as VSC and palynological studies carried out in one sample picked at 194.3 m provided a mid to late Visean age (Projecto Monte das Mesas, Aljustrel, 4º Relatório semestral de Actividade, 1º Semestre de 2014). This section presents two possible shear zones at ~168 and ~190 meters, that geometrically separate the Mértola Formation and the VSC sequence stratigraphically bellow.

At ~220 meters, a shear zone precedes ~30 meters of (greenish) felsic volcaniclastic rocks with quartz and feldspar clasts, separating them from the overlaying succession of green, purple and grey metapelites (S_1 = 60°). A thin (261.00-264.20 m) and quite brecciated layer of jasper enriched in magnetite (locally also including late-deposited and fracture-controlled calcite), is followed by felsic volcaniclastic rocks (with millimeter sized quartz and sericitized feldspar clasts) displaying domains with evident disseminations of pyrite (mostly from 261 to ~437 meters).

At ~415 and ~452 meters two fault zones were intersected, in between were drilled rhyolitic lavas contacting felsic volcaniclastic rocks. Towards the base of the drilled sequence, spilitic rocks contact a pile of intermediate facies.

During drilling, the intersected VSC sequence was interpreted as the NE limb of the Gavião anticline. The drilling was were stopped around 530 meters, and the existence of a large amplitude anticlinal fold, together with a series of inverse faults zones, were reported (Relatório Atividades 2º Semestre 2013, Monte das Mesas).

IV.3. Z1

The drill-hole Z1 was designed by EDMA (Empresa de Desenvolvimento Mineiro do Alentejo) and performed in 1985 by Sondagens e Fundações A. Cavaco, Lda. at ca. 800 m to the SW of Rio de Moinhos (i.e. ~2000 m to the NW of the Gavião deposit) on coordinates X = -7856.40 and Y = -197189.20 (ETRS89 PT-TM06), and having 220° azimuth -77° dip (Relatório Preliminar da Sondagem Z1, EDMA).

The drilling's main goal was to investigate the conductive horizons detected by the magneto-telluric method along two profiles crossing the possible extension of the Gavião ore-hosting structure to the NW. The entire area was previously subjected to gravimetric and magnetic studies performed by the SFM (Serviço de Fomento Mineiro) followed by induced and magnetic polarization studies completed by the Barringer Research Ltd., Toronto, for SMS (Sociedade Mineira de Santiago) (Relatório Preliminar da Sondagem Z1, EDMA).

The first 21.45 meters of the drill-hole were performed without core recovery. However, the available technical reports provide information on fragments of brown sandy material, most possibly corresponding to the Cenozoic detrital cover (Relatório Preliminar da Sondagem Z1, EDMA). After, the drilling intersected up to 223.20 meters of mafic metavolcanics: dark to light-green basalt flows, preserving features ascribable to oceanic metasomatism, pillow lava structures, and weakly disseminated pyrite, pyrrhotite and iron oxides. This pile of mafic metavolcanics overlies a succession mainly composed of green-colored and foliated felsic volcaniclastic rocks, sometimes including intercalations of black metapelites. Note, however, that between 80.00-153.00 meters several core boxes are missing and the development of intercalations between mafic volcanics and felsic volcaniclastic rocks are reported in previous logging records, as well as dolerite dykes (Relatório Preliminar da Sondagem Z1, EDMA).

From ~223.00 to ~297.00 meters, the drill-hole displays several intercalations between greyish-green felsic volcaniclastic rocks and minor black to grey metapelites, mostly contacting each other through gradual transitions. This VSC sequence displays evidence of sericite- and/or chlorite-dominant alteration of moderate intensity. Rhyolitic lavas are also present between ~256.00 to 286.00 meters, from 284.20 to 285.85 meters, the drilling intersected a horizon enriched in branched sulfide (pyrite + pyrrhotite) veinlets. After ~311.00 meters, a rhythmic sequence of black metapelites and felsic volcaniclastic rocks occur, developing gradual contacts; the ensemble is often intersected by dolerite sills.

The deeper section of the drill-hole, from 497.00 to 532.05 m, is almost exclusively formed by black metapelites in addition to minor intervals of fine-grained impure quartzites and/or meta-greywackes included in the siliciclastic (BAFG or PQG?) metasedimentary succession.

In general, several sections of this drill-hole preserve different structures due to heterogeneous strain accommodation and are traversed by some fault zones, the most important of which observed at ca. at ~253.00 m, ~496.00 m and ~520.00 m. Commonly, S_0 is transposed by S_1 and (mainly) ranges 25° to 70° from long core axis (LCA).

The mafic dykes/sills are of intrusive character, as evidenced by the sharp contacts with the host rocks and the preservation of gradients of grain-size reduction commonly denoting cooling margins. Locally, some of the host rocks adjoining the contact with the mafic dykes/sills display mineral and textural changes that may be interpreted as a result of limited metasomatic processes related to the emplacement of the intrusive bodies. All these features suggest that these mafic dykes/sills document a relatively late magmatic event, post-dating the main (bimodal) VSC piles but preceding the BAFG development; moreover, the emplacement of these igneous bodies should be mostly controlled by deep mechanical (structural) weaknesses, such as fault zones and/or contrasting lithological contacts.

The drilling ended at 532.05 m, long after the target pointed out by the magneto-telluric study (at a depth of 300-400 m), but whose anomaly source could be explained by the reologic contrast between the mafic rocks and the black metapelites, that respond, by comparison, as conductive rocks.

IV.4. Z2

The drill-hole Z2 was designed by EDMA and performed in 1986 by the Sondagens Foraky Lda. at ca. 300 m to the E of Z1, on coordinates X = -7436.40 and Y = -197419.19 (ET RS89 PT-TM06) and having -225° azimuth and -70° dip (Relatório Preliminar da Sondagem Z2, EDMA).

The first ~100.00 meters were not re-logged, but the report of previous logging states a sequence of clay levels and conglomerate rocks, ascribable to the Cenozoic detrital cover, followed by variably modified (i.e. altered) mafic metavolcanics (Relatório Preliminar da Sondagem Z2, EDMA).

The next 62.85 meters intersected mafic metavolcanics: dark to light-green basalt flows, recording mineral and textural changes due to the progression of oceanic metasomatic processes, as well as pillow lava structures and weakly disseminated pyrite. This pile of mafic volcanic rocks overlies a thick succession of greenish-grey felsic metavolcaniclastic facies, sometimes including intercalations of black metapelites with and without levels enriched in a sandy (volcanic-derived?) component and several rhyolitic lava flows. The VSC sequence was drilled down up to 482.50 m, showing gradual transitions mostly between felsic volcaniclastic rocks (comprising weakly disseminated pyrite) and metapelite rocks (enclosing a minor sandy (volcanic-derived?) component). Note, however, that between 232.15-240.00 meters several boxes are missing, but previous logging states a similar sequence, i.e. intercalations between black metapelites and felsic volcaniclastics.

Apart from the upper section of the drill-hole, three main different alteration styles were observed: (i) chloritization, (ii) sericitization and (iii) silicification. Nonetheless, the intensity of the mineral and textural changes is always weak.

The aforementioned metavolcanic/metasedimentary successions are crossed by (late-emplaced) dolerite sills/dykes similar to those observed in Z1 drill-hole.

In general, several sections of the Z2 drill-hole preserve different features indicating heterogeneous deformation/folding that precede the development of fault zones. Commonly, S_0 is transposed by S_1 and (mainly) ranges 20° to 40° from long core axis (LCA).

IV.1. MdM05

The drill-hole MdM05 was designed by the Esanmet Portugal, Lda. and performed in 2017 by the Drillcon Ibéria on coordinates (ETRS89 PT-TM06) X: -7151.88; Y: -196917.85, azimuth N225° and dip -60°.

The MdM05 drill-hole was planned to investigate the geochemical target identified by Esanmet Portugal, Lda., South from Rio de Moinhos. The analysis and processing of the soil campaign results, (using "Ionic leach" technique), highlighted a target with positive anomalies in almost all base metals related to massive sulfide deposits (except lead), with azimuth similar to other known close massive sulfide deposits (*e.g.* Gavião).

The first 52.00 meters crossed sediments belonging to the Cenozoic detrital cover on top of the Paleozoic folded basement. After, the drill-hole intersected a thick sequence of rock types ascribed to the VSC. The uppermost part of this sequence (up to 218.15 m), includes intercalations of black, light- to dark-green and purple metapelites (often including thin meta-siltitic levels). Chlorite- and sericite-dominant alteration, although heterogeneous, affect most of the sequence; pyrite is frequent along foliation and forming small nodules. From 154.75 to 156.25 m, pyrite dissemination is quite intense, occasionally almost semi-massive. Tectonic discontinuities are commonly found, often tracing fault zones, the most important of which crossed at 86.20 m, 112.80 m, 192.00 m and 213.60 m. In general, several sections of this drill-hole show macroscopic features due to heterogeneous strain accommodation. Commonly, S_0 is transposed by S_1 and (mainly) ranges 20° to 50° from long core axis (LCA).

From 213.70 – 218.15 m an important fault zone was intersected, composed by fault gouge and evidence of brecciation. This discontinuity puts in contact the previous upper sequence of the CVS with a thick (up to 561.30 m) of mafic metavolcanics: dark to light-green basalt flows, locally preserving pillow lava structures and a series of mineral/textural changes due to the progressing of oceanic metasomatic processes along with weakly disseminated hematite along metasomatic fronts.

The lowermost VSC section crossed by MdM05 includes a variably altered (chloritization, sericitization, silicification) succession green-grey felsic volcaniclastic rocks (quite enriched in feldspar clasts), black metapelites (including a significant sandy-derived component of possible volcanic origin) and rhyolitic lava flows. This succession is intruded by dolerite sills/dykes displaying weakly disseminated pyrrhotite and evident cooled margins. Tectonic discontinuities are frequent the most relevant of which corresponding to the fault zones intersected at 835.40 m and 838.80 m.

The MdM05 drill-hole ended at 901.80 m since there was no massive sulfide associated hydrothermal alteration evidence that justified the continuation of the drilling.

IV.2. MdM01

The drill-hole MdM01 was designed by Esanmet Portugal, Lda. and performed in 2017 by Drillcon Ibéria on coordinates (ETRS89 PT-TM06) X: -8189.26; Y: -193427.02, azimuth N225º and dip -60º (10º Relatório Semestral de Actividades, 1º semester de 2017, Monte das Mesas - Gavião).The location and planning of the drill-hole was based not only on pre-existing data (cartography and geophysical studies), but also on results of a new airborne geophysical survey carried out in September 2016 by the Canadian company Geotech Ltd. at the request of Esanmet Portugal. The MdM01 drill-hole was planned to investigate the geophysical target identified by Geotech as A2_T1, based on the Maxwell 2.5D plate model and the interpretive sections obtained by the deep resistivity images (RDI) (10º Relatório Semestral de Actividades, 1º semester de 2017, Monte das Mesas - Gavião).

The first 14.85 meters drilled document the presence of sediments belonging to the Cenozoic detrital cover on top of the folded Paleozoic basement. The latter correspond to a thick VSC sequence, extending up to 744.90 meters. The uppermost part of this sequence (up to 90.85 m) includes dark to light-green metavolcaniclastic felsic rocks (comprising mostly feldspar clasts along with minor quartz) intercalated with massive/coherent, rhyolitic rocks. This sequence is frequently cut by quartz + chlorite + carbonate

veins. Chlorite and sericite alteration of variable intensity affect also both rock types, being stronger in volcaniclastic facies.

From 90.85 to 229.45 m, the VSC section is mainly composed of black metapelites often including levels variably enriched in a sandy (distal, volcanic-derived products?) component; all through this VSC section, the felsic metavolcaniclastic rocks, although present, are minor. Pyrite is abundant, occurring as: (i) colomorphic aggregates; (ii) disseminations, mostly controlled by foliation planes and occasionally developing clusters of centimeter size; and (iii) very fine-grained disseminations in the rock matrix.

The VSC section observed from 229.45 to 422.40 m is characterized by a sequence analogous to the uppermost one (i.e. intercalations of felsic volcaniclastic rocks and massive/coherent rhyolitic rocks), although comprising several layers of dark-grey/black metapelites (often including significant amounts of volcanic-derived products). All these rock types display frequently brecciated textures resulting from the development of anastomosed, chlorite-rich veining that also includes weakly disseminated, fine-grained sulfides. Locally, sericite-dominant and chlorite-dominant alteration can be quite intense.

From 422.40 m to 560.00 m, the drilling crossed a dolerite sill/dyke that, locally, also preserves delicate brecciated textures due to anastomosed quartz + chlorite + carbonate + pyrrhotite veining.

At 560.00 meters, a grey chert/flint overlies ~70 meters of the VSC sequence that displays evidence of strong sericite- and/or chlorite-dominant alteration (locally complemented with significant silicification), mainly expressed in dark-colored metapelites, sometimes evolving rhyolitic rocks and minor metavolcaniclastic rocks. Disseminations of pyrite are frequent, sometimes along with trace amounts of chalcopyrite; locally, fracture infillings of very fine-grained sphalerite and galena can be observed.

The lower section (620.00 to 744.90 m) of the VSC sequence intersected by the MdM01 drill-hole corresponds to a monotonous metasedimentary sequence, typified by intercalations (often in rhythmic succession) of black metapelites variably enriched in sandy (distal, volcanic-derived?) component.

The last ~150 meters of the drill-hole includes a fine-grained metasedimentary succession comprising interfingered black metapelites and impure quartzites and/or metagreywackes, whose correlation with one of the main siliciclastic sequences (Mértola Formation of BAFG, or PQG) is controversial. The schematic interpretative cross-section between drill-holes MdM01 and MM05 (Figure VI.4.1) geometrically favors the correlation with the Mértola Formation, evidencing an imbricated “thin-skinned” complex through stacked thrust faults, leading to a further repetition of the lithostratigraphic sequence.

In general, several sections of the MdM01 drill-hole show a wide range of macroscopic features that support the inference of significant but heterogeneous deformation (such as various styles of folding, foliation/schistosity, multiple sets of fractures, etc.), culminating with various fault zones, the most important of which intersected at 111.60 m, 229.45 m, 565.05 m, ~650 m and 761.85m. As indicated for other drill-cores, S_0 is usually transposed by S_1 and (mainly) ranges 30° to 70° from long core axis (LCA).

The MdM01 drill-hole finished at 800.75 meters, after intersecting more than 100 m of metasedimentary rocks interpreted as part of the Mértola Formation (stratigraphically more recent in age than the successions that typically host the sulfide mineralization in the Iberian Pyrite Belt). Also, it was concluded that geophysical anomaly supporting the intended target was conceivably due to the presence

of “graphitic” shale levels with some disseminated (and interconnected) pyrite grains (10º Relatório Semestral de Actividades, 1º semestre de 2017, Monte das Mesas - Gavião).

IV.3. MdM02

The drill-hole MdM02 was designed by Esanmet Portugal, Lda. and performed in 2017 by Drillcon Ibéria on coordinates (ETRS89 PT-TM06) X: -9154.87; Y: -193552.26 and having azimuth N225º and dip -75º (10º Relatório Semestral de Actividades, 1º semestre de 2017, Monte das Mesas - Gavião). The drilling was planned to investigate the geophysical target identified by Geotech as A2_EMFT3, based on the Maxwell 2.5D plate model and interpretive sections obtained by deep resistivity images (RDI).

The first 16.45 m drilled correspond to sediments belonging to the Cenozoic detrital cover on top of the Paleozoic folded basement. The uppermost part of this basement (16.45–137.30 m) is interpreted as part of the VSC sequence that includes intercalated purple- and green-colored metapelites frequently displaying a sandy (volcanic-derived?) contribution, besides some volcaniclastic levels strongly foliated. Between 137.30-151.90 m, and in addition to purple and green metapelites, the sequence comprises abundant black metapelites and volcaniclastic rocks usually preserving effects of strong sericite- and/or chlorite-dominant alteration that is crossed by quartz + chlorite + carbonate veins. Pyrite is usually along foliation and particularly significant in black metapelites.

The next section of VSC (151.90-339.20 m) includes an intercalation of five main facies, whose relative abundance is as followed: (i) massive/coherent, rhyolitic rocks (lavas?); (ii) very light-green volcaniclastic rocks (quite enriched in sericite and without evident foliation); (iii) silicified volcaniclastic rocks; (iv) foliated volcaniclastic rocks with darker and lighter domains (perhaps reflecting differences in chlorite/sericite proportions); and (v) black metapelites that become more abundant towards the base, displaying as well pyrite along foliation and fractures.

At 385.90 m, a fault zone puts in contact the aforementioned rhyolitic rocks with a metasedimentary succession where similar rocks present very fine-grained greywack inter-fingering and are quite enriched in pyrite (along foliation and developing disseminations).

The lower section of the VSC sequence crossed by MdM02 (408.00 - 501.30 m) is composed of a rhythmic succession of intercalated dark- and light-green volcaniclastic rocks showing heterogeneous enrichments in silica; this succession shows macroscopic evidence of hydrothermal alteration (sericitization and chloritization) and is quite fragmented due to abundant tectonic discontinuities. Towards the end of this section, some intercalations of rhyolitic lavas can be observed.

The last meters of the MdM02 drill-hole (501.30 - 531.90 m) correspond to a monotonous metasedimentary sequence characterized by intercalations (often in rhythmic succession) of black metapelites and subordinate meta-greywacke interfingering until 523.00 meters, and the reverse relative abundancy afterwards. Considering the prevailing rock types, this metasedimentary sequence can be tentatively correlated to the siliciclastic, Mértola Formation of the BAFG.

As observed in cores of other drill-holes, a wide range of macroscopic features that support the inference of significant but heterogeneous deformation are preserved in several sections of MdM02, including some fault zones. Commonly, S_0 is transposed by S_1 and (mainly) ranges 10° to 80° from long core axis (LCA).

The MdM02 drill-hole was finished at 531.90 meters after intersecting several meters of metasediments interpreted as belonging to the Mértola Formation. Similarly to the MdM01 drill-hole, the EM anomaly that justified the drilling was explained on the basis of “graphitic” shale levels with some disseminated

(and interconnected) pyrite grains (10º Relatório Semestral de Actividades, 1º semestre de 2017, Monte das Mesas - Gavião).

IV.1. MM05

The MM05 drill-hole was planned considering the structural and gravimetric data resulting from previous exploration surveys that allowed the identification of the most favorable alignments and targets of higher potential. The drilling was performed at coordinates X=-7600; Y=-194450 (ETRS89 PT-TM06) having azimuth 225º and -60° dip. Positioned about 5000 meters towards the NW of the Gavião deposit, in view of the Monte Grande gravimetric anomaly, conceivably representing the NW extension of the Feitais-Estação volcano-sedimentary alignment displaced by the Messejana strike-slip fault zone (Projecto Monte das Mesas, Aljustrel, 2º Relatório semestral de Actividades, 1º Semestre de 2013; Relatório de actividades 1º Semestre, 2014).

The first ~43 meters were not re-logged for logistic reasons, but previous logging information states the presence of Cenozoic detrital sedimentary deposits (~16 m) followed by a dolerite rock (Relatório de actividades 1º Semestre, 2014). Between ~43 to ~59 meters, the drilling crossed a coherent mafic volcanic rock with disseminated sulfides (mostly pyrite), followed by ~20 meters of light-green rhyolitic rocks also showing pyrite dissemination. From ~90 to ~130 meters, the main rock type corresponds to a dark-grey metapelite including occasional layers quite enriched in tiny clasts of feldspar and quartz (possible distal volcanogenic contribution) as well as a felsic and quite foliated volcaniclastic rock (showing a chlorite and sericite rich matrix) followed by a "squeezed" (highly deformed) dark-grey metapelite. The drill core from ~114 to 118 meters was not re-logged also for logistic reasons. A fault zone at ca. ~130 meters precedes a rhyolitic rock preserving evidence of strong chloritization and sericitization, being as well affected by intense fragmentation throughout the first meters, adjoining the fault zone. After ~159 meters, a dark-grey metapelite with recurrent levels enriched in feldspar and quartz clasts (possibly indicating periods of more intense volcanogenic contribution) can be observed, also showing fracture-controlled pyrite infillings along with pyrite disseminations along foliation and local development of millimeter pyrite nodules parallel do foliation.

From ~223 to 290 meters, a mafic rock displaying an anastomosed network of fractures with very fine-grained sulfides, encircled by sericite and chlorite rich haloes (locally exhibiting brecciated texture) contacts by means of a fault zone with a metasedimentary succession composed of interfingered black, green and purple metapelites that continue until ~350 meters. The latter succession was ascribed to the Paraíso Formation (Upper CVS). The drilling was stopped after intersecting ~60 meters of a "monotonous" succession of metasedimentary rocks (composed of dark metapelites interfingered with thin metagraywacke layers) interpreted as part of the Mértola Formation (stratigraphically more recent in age than the successions that typically host the sulfide mineralization in the Iberian Pyrite Belt).

V. Macroscopic characterization

This chapter characterizes, although synthetically, all lithologies prevalent macroscopic features, present and sampled along the relogged drill-cores. A list of the 80 samples collected from the observed drill-cores along with a synthetic description of their prevalent macroscopic features and indication of the selection done for subsequent petrography work (29 polished thin-sections).

VI. Interpretative geological profiles

VI.1. MM01

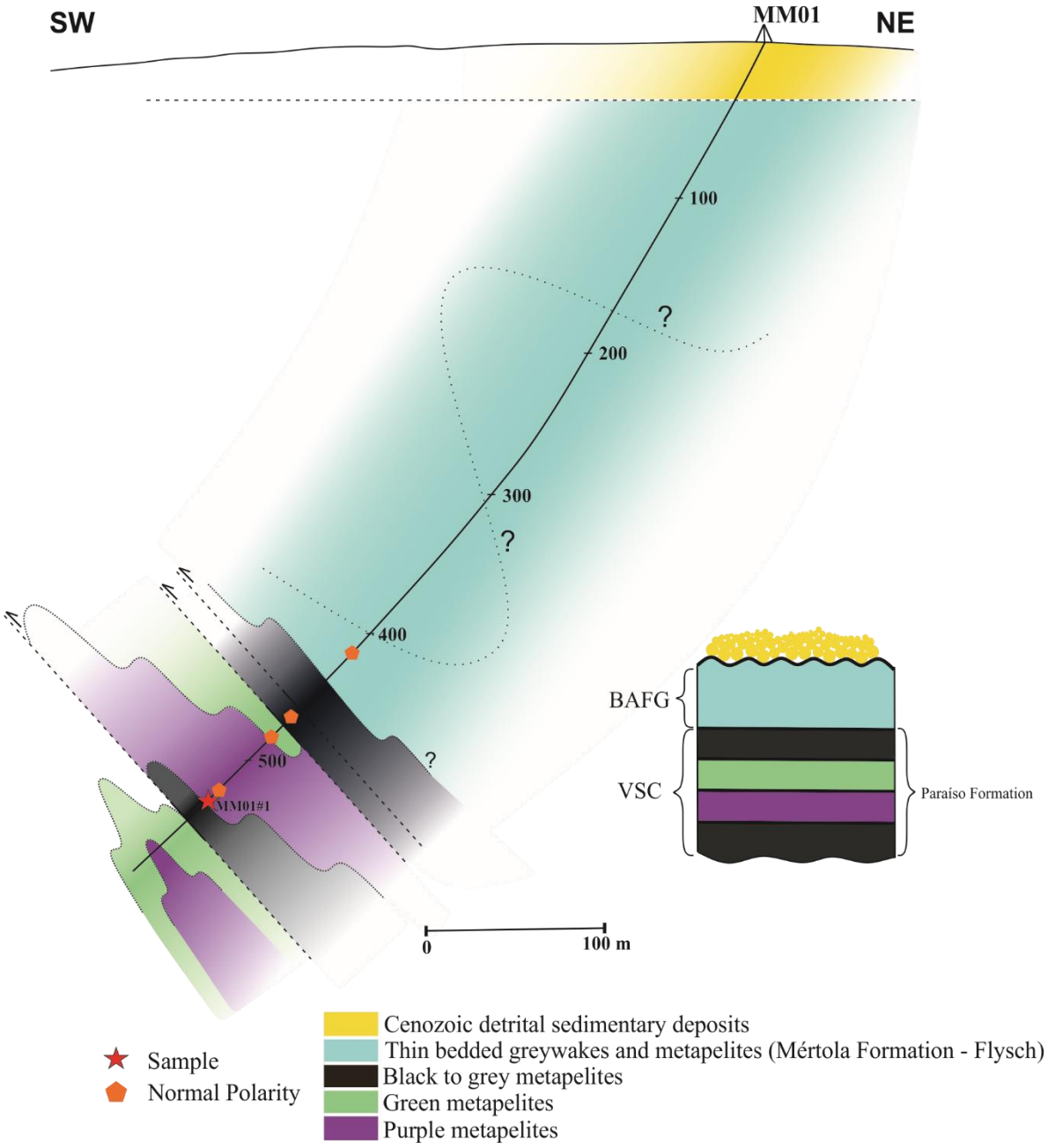

Figure VI.1.1 Interpretative geological profile for drill-hole MM01.

VI.2. MM02

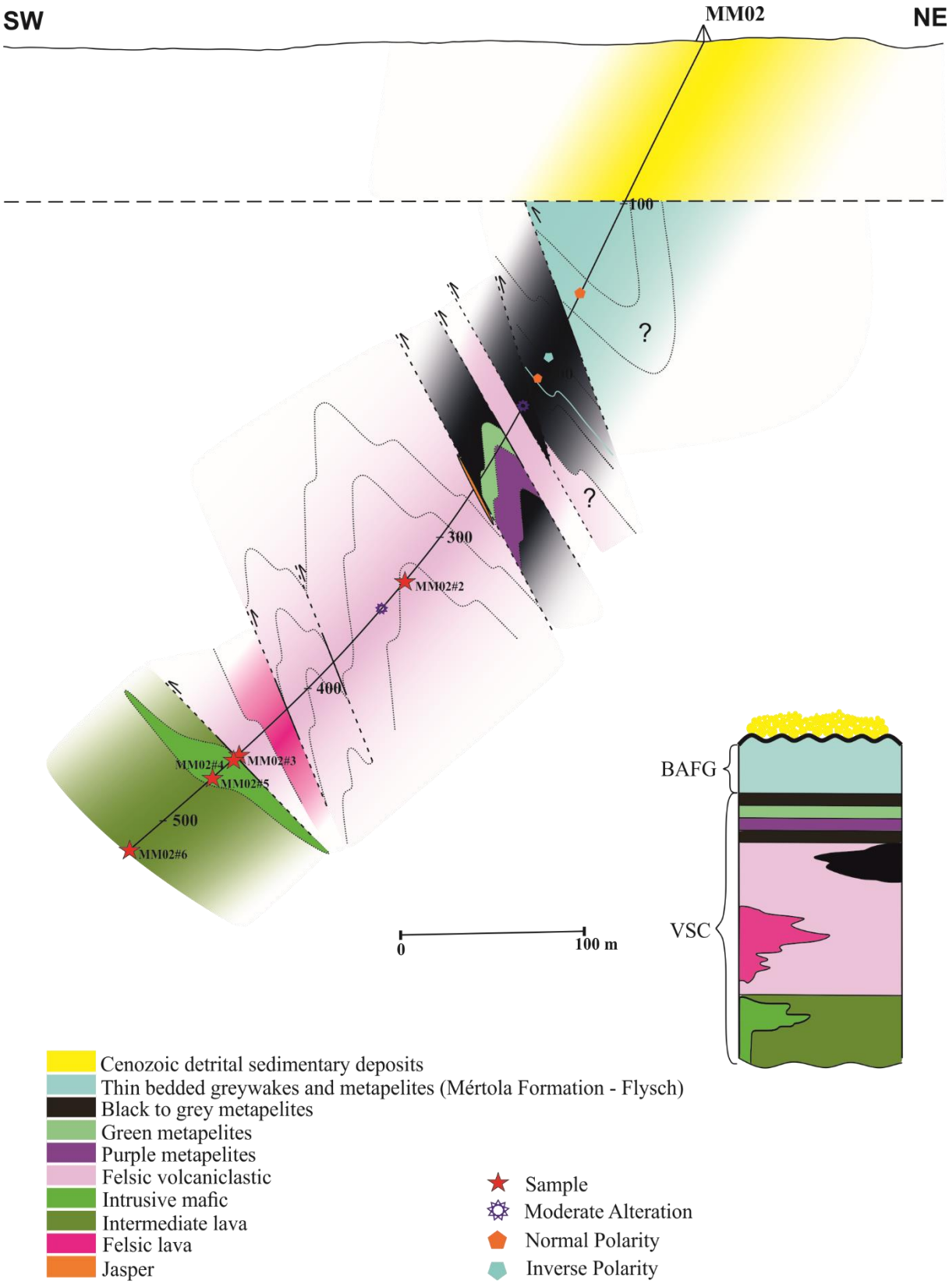

Figure VI.2.1 Interpretative geological profile for drill-hole MM02.

VI.3. Z1 – Z2 – MdM05

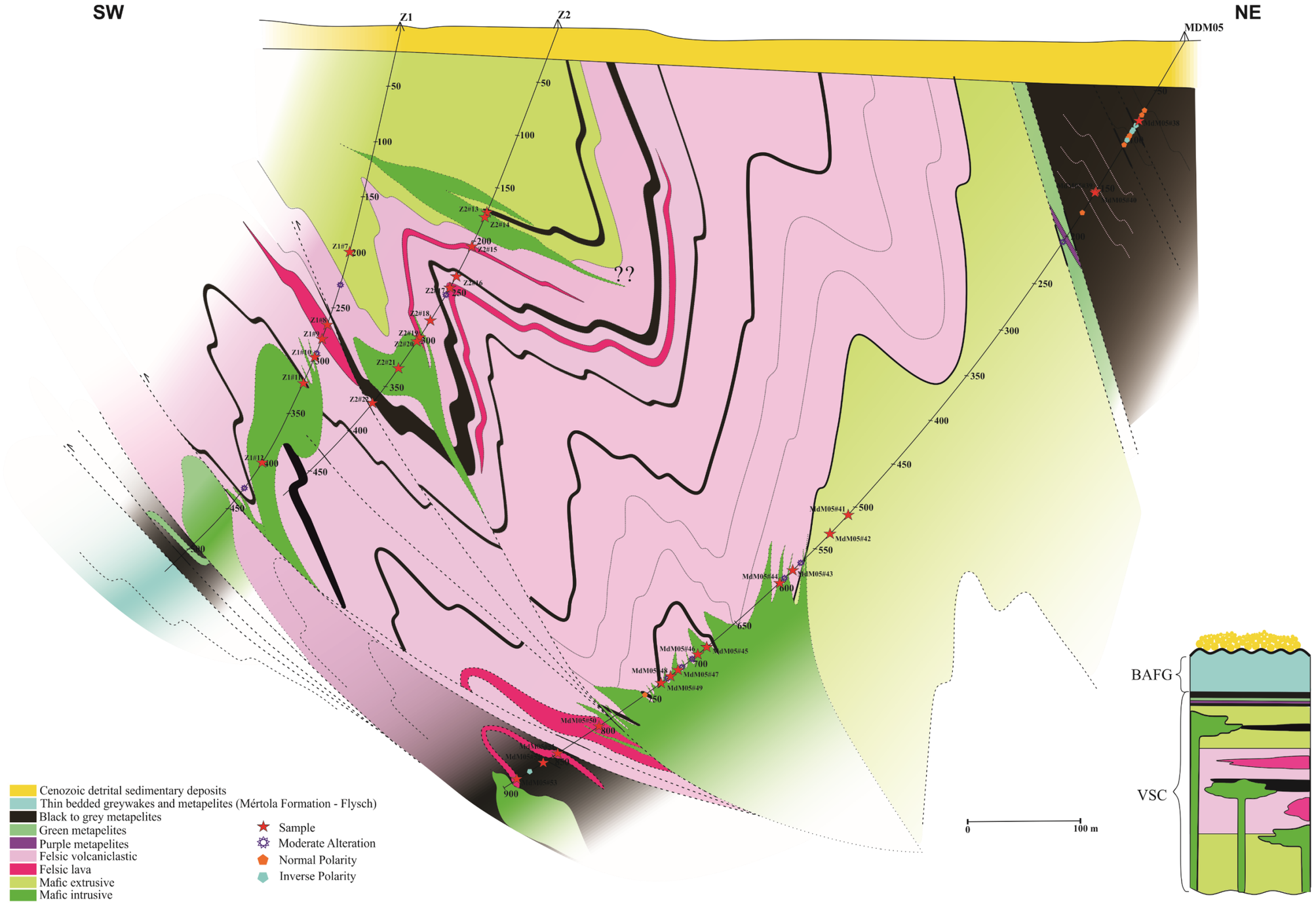

Figure VI.3.1 Interpretative geological crossection for drill-holes Z1 – Z2 – MdM05.

VI.4. MdM02

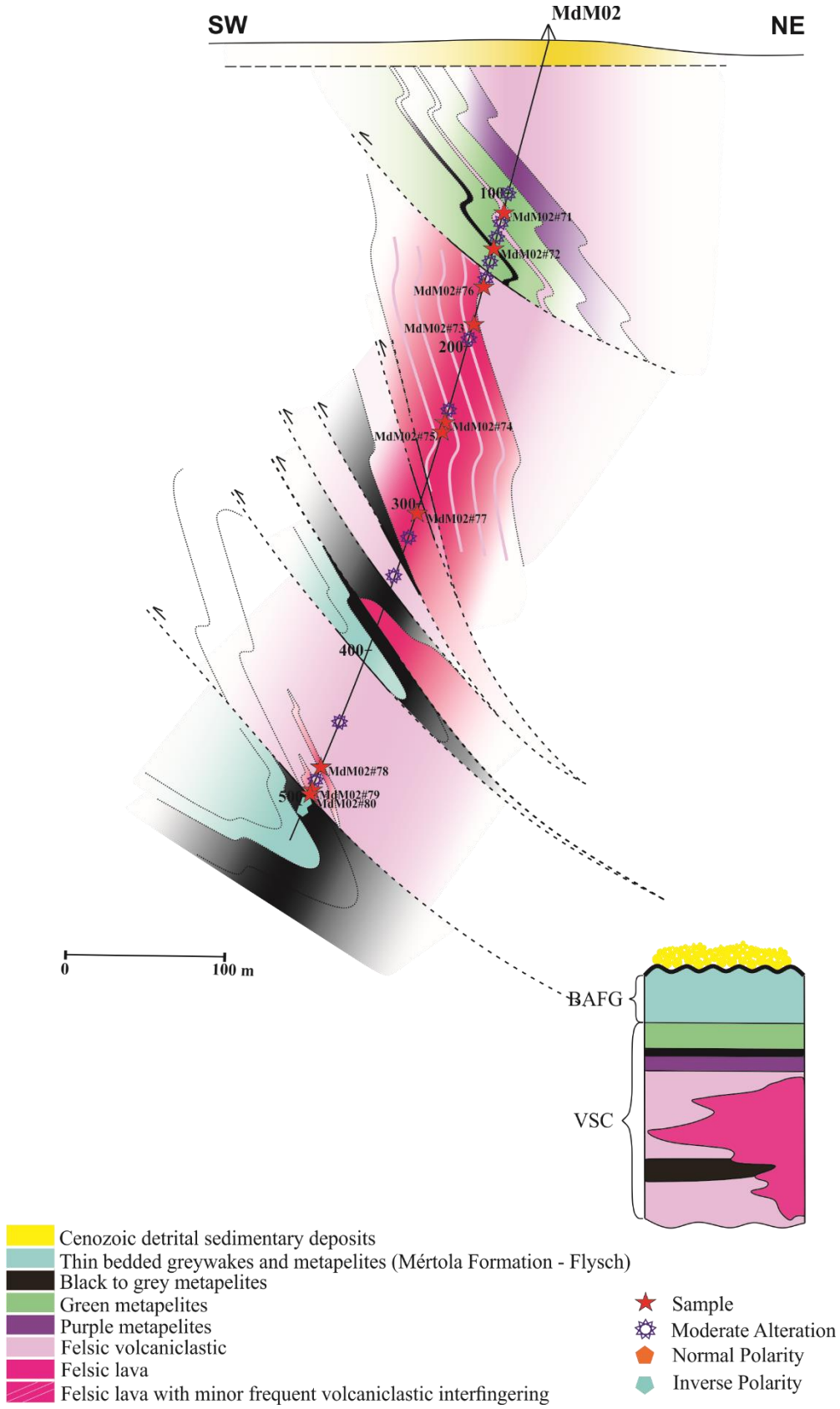

Figure VI.4.1 Interpretative geological profile for drill-hole MdM02

VI.5. MM05 – MdM01

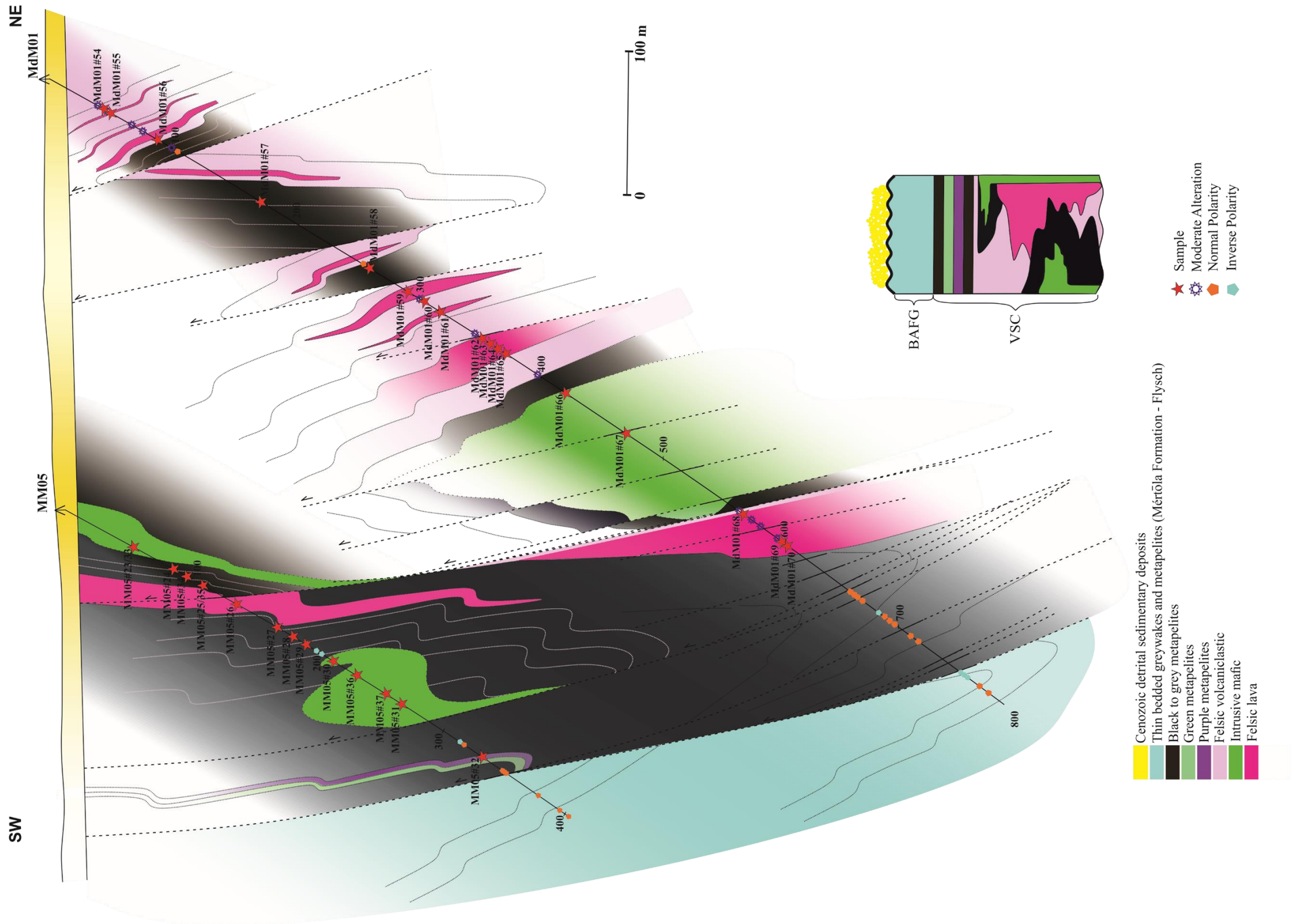

Figure VI.4.1 Interpretative geological crossection for drill-holes MM05 and MdM01.

VII. Lithostratigraphy

The Aljustrel VSC is divided into the Paraíso Siliceous Formation and the Aljustrel Volcanics (Schermerhorn and Stanton, 1969; Andrade and Schermerhorn, 1971). The Paraíso Formation is composed of rare felsic and intermediate pyroclastic rocks intercalated within (dominant) metapelites, many of them including volcanic-derived components (*e.g.* Barriga, 1983). The Aljustrel Volcanics is mostly composed of granular tuffs (Schermerhorn, 1975, 1976) characterized by a fragmental matrix composed of quartz and feldspar grains (that vary in size, shape and composition) enclosed in an almost submicroscopic framework of sericitic (± chloritic); inversely, this sericitic framework can predominate relatively to the quartz + feldspar grains (Schermerhorn, 1970b). The Aljustrel Volcanics were further divided, considering variations in composition, size and relative abundance of all these components.

Carvalho *et al*., (1976), Schermerhorn (1971) divided the Aljustrel Volcanics into (i) a central group composed of a coarse grained crystal-rich tuff lower unit (the "Megacrystic Tuff Formation") and an ash tuff upper unit (the "Green Tuff Formation"); and (ii) a more distal facies, laterally equivalent, composed by fine-grained sediments enriched in volcanic-derived fractions (the "Felsitic Tuff Formation"), and an upper unit of massive sulfide bearing tuff (the "Mine Tuff Formation"), respectively. The consistency of the chrono-spatial relations between the different units, coupled with an unambiguous cartographic expression, resulted in their adoption by subsequent authors. Following studies of the petrographic characterization of the different lithotypes (*e.g.* Barriga, 1983; Relvas, 1991) pointed out that part of the textural and paragenetic heterogeneity of these rocks should be attributed to secondary processes of sea water metasomatism and hydrothermal alteration and not to different original petrogenetic phenomena, justifying small but significant adjustments to the originally proposed stratigraphic divisions.

In 2003, EuroZinc Mining Corporation (Dawson and Caessa, 2003) informally subdivided the stratigraphy of the Aljustrel Mine, according to lithogeochemical studies, into (i) Lower Rhyolite unite (X, A and B), (ii) Massive Sulfide horizon(s), (iii) Upper Rhyolite unit (C), (iv) Quartz Feldspar Porphyritic Rhyolite unit (qf), (v) Lower Sedimentary unit, and (vi) Upper Sedimentary unit.

A different lithostratigraphic subdivision was proposed by Leitão (2014), considering three distinct volcanic cycles. The first cycle refers to a quartz-feldspathic rhyolitic lava Formation (QLF), whereas the second refers to an albite-phyric rhyolitic Formation (ALF), both formations including lava flows and volcaniclastic products resulting from progressive alteration and dismantling of the volcanic domes. The last volcanic cycle is mafic and composed of pillow lavas stratigraphically on top of the ALF, besides sills intruded along de QLF volcaniclastic sequence.

For the Monte das Mesas area, two separate lithostratigraphic columns were designed, one for each cluster of drillings (to the NW and SE, respectively). Despite different in detail, both columns share many similarities and generically fit the overall IPB lithostratigraphy. Compared to the Aljustrel lithostratigraphic columns, the drilled VSC sequence at Monte das Mesas area does not present any facies that can be correlated with either the "Megacrystic Tuff Formation" or the "Green Tuff Formation". The lack of these particular coarse-grained facies suggests a more distal character for the drilled VSC sequence, which is consistent with (1) the predominance of fine-grained (matrix-supported) volcaniclastic facies over coherent or clast-supported facies and (2) the relative abundance of metapelite rocks.

Voluminous mafic rocks (both intrusive and extrusive) at Monte das Mesas area is the most distinctive feature. According to Leitão (2014), prevalent mafic rocks represent the last volcanic cycle; at Monte das Mesas the same is not necessarily true, existing at least two different mafic (extrusive) volcanic

impulses, one (β_1) stratigraphically older than several felsic volcanic episodes. However, assuming that these mafic and felsic magmas do not have the same magmatic source (as happens in many other sectors of the IPB), these episodes, β_1 and β_2, could be, at some point, contemporaneous to earlier and latter felsic volcanic episodes, respectively. Therefore, two different hypotheses are suggested: (1) the overall VSC sequence intersected at Monte das Mesas correlates to an Upper VSC sequence or (2) the mafic volcanic episode β_1 refers to a much earlier (mid-lower VSC) volcanic episode, not described by Leitão (2014).

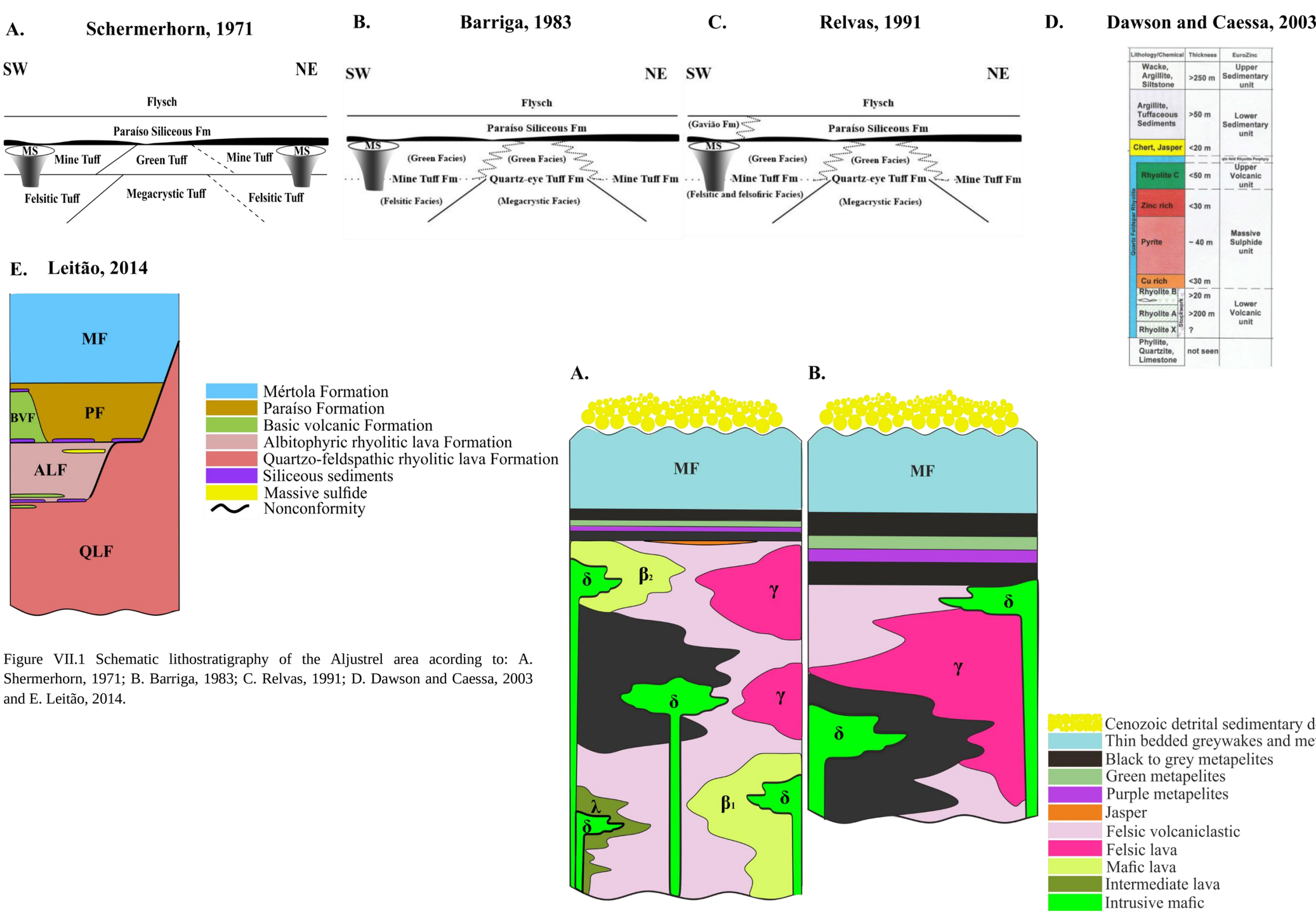

Figure VII.1 Schematic lithostratigraphy of the Aljustrel area acording to: A. Shermerhorn, 1971; B. Barriga, 1983; C. Relvas, 1991; D. Dawson and Caessa, 2003 and E. Leitão, 2014.

Figure VII.2 Schematic lithostratigraphy of the Monte das Mesas area: (A) Cluster South; (B) Cluster North.

VIII. Petrographic characterization

This chapter summarizes all the mineralogical and textural features noted during petrography of the main rock types, always considering the macroscopic scale observations. At Monte das Mesas, the main rock types forming the VSC can be classified as follows: metapelites, felsic, intermediate and mafic metavolcanic rocks. A list of all the polished thin sections studied, providing information on their geographical location, depth and classification can be found in Appendix VI.

VIII.1. Metapelites

In this work the term metapelite refers to a fine-grained metamorphosed clastic sediment, where quartz and feldspar clasts are of variable size and mostly rounded, wrapped in a sericite-rich matrix. When (micro-)porphyroblasts exist, these are often twisted and display pressure shadows or fringes; spiral feldspar porphyroblasts preserving wavy extinction and deformation twins occur in samples having strongly folded sericite-rich matrix. In these rocks, foliation is parallel to S_0 and the accessory mineralogy includes sulfides, (hydro)oxides, chlorite, apatite, zircon, epidote, titanite, rutile and tourmaline.

Sericitic alteration is very strong, underlined by intense hydrolysis of feldspar clasts when these are abundant. In some samples (*e.g.* MdM05#52) it is possible to infer that sericitic alteration precedes deformation, i.e. the sericitization took place before regional metamorphism and foliation (followed by crenulation in some samples; *e.g.* MdM05#38, MdM05#52).

Two generations of chlorite are present, the first coming together with epidote and/or carbonates, and the second with no epidote or carbonates; however, both are most likely contemporaneous to deformation and regional metamorphism (*e.g.* MM02#3).

Two chronological different carbonation events were distinguished, the earlier associated with quartz and sulfide veinlets heavily deformed (including micro-boudinage) and the later, pervasive event, succeeding the regional metamorphic peak (*e.g.* MM02#3, MdM05#38).

The amount of sulfides varies in between samples. Nonetheless, pyrite is by far the most abundant associated with minor amounts of pyrrhotite, chalcopyrite, sphalerite and galena. Texturally, these sulfides occur as fine disseminations in matrix or as infillings of veinlets geometrically concordant with foliation that also contain quartz and carbonates.

(Hydro)oxides, in particular hematite, are also present in some samples (*e.g.* MdM05#38), forming tiny disseminations and/or very fine straws mostly along the crenulation plans.

Figure VIII.1 Photographs of representative mineralogical and textural aspects of the metapelite group: (A) black metapelite with very fine-grained sandy component (detritus or volcanogenic?), disseminated Py and along foliation with pre-deformation Qz + Py ± Cal veining; (B) strong disseminated medium to fine-grained Py, Qz + Py ± Cal venules displaying incipient effects of boudinage; (C) disseminated Py along foliation planes and pre-deformation venules displaying incipient effects of boudinage; (D) Brownish metapelite (weathered?), highly deformed (folded and fractured); (E) purple metapelite with significant fine-grained sandy component (detritus or volcanogenic?); (F) gradual contact between a very fine metapelite and a volcaniclastic rock; (G) depositional contact between a volcaniclastic rock and a black metapelite; (H) inter-fingering between black and grey metapelite, Py lenses/nodules and disseminated pyrite along foliation.

Figure VIII.2 Photomicrographs of particular aspects of the metapelite group: (A) foliation concordant venule, highly deformed, composed of sulfides (mostly Py) + Qz + Cb + Ep; (B) strong foliation and crenulation; (C) twisted Qz clast in a very fine white mica matrix; (D) recrystallized Qz and post-deformation Cb; (E) zoned Py with Po and Ccp inclusions; (F) highly sericitized feldspar clasts in a quartz and fine (preceding deformation) white mica matrix; (G) twisted porphyroblasts in a strongly sericitized and deformed (Qz+Ms) matrix; (H) highly silicified metapelite.

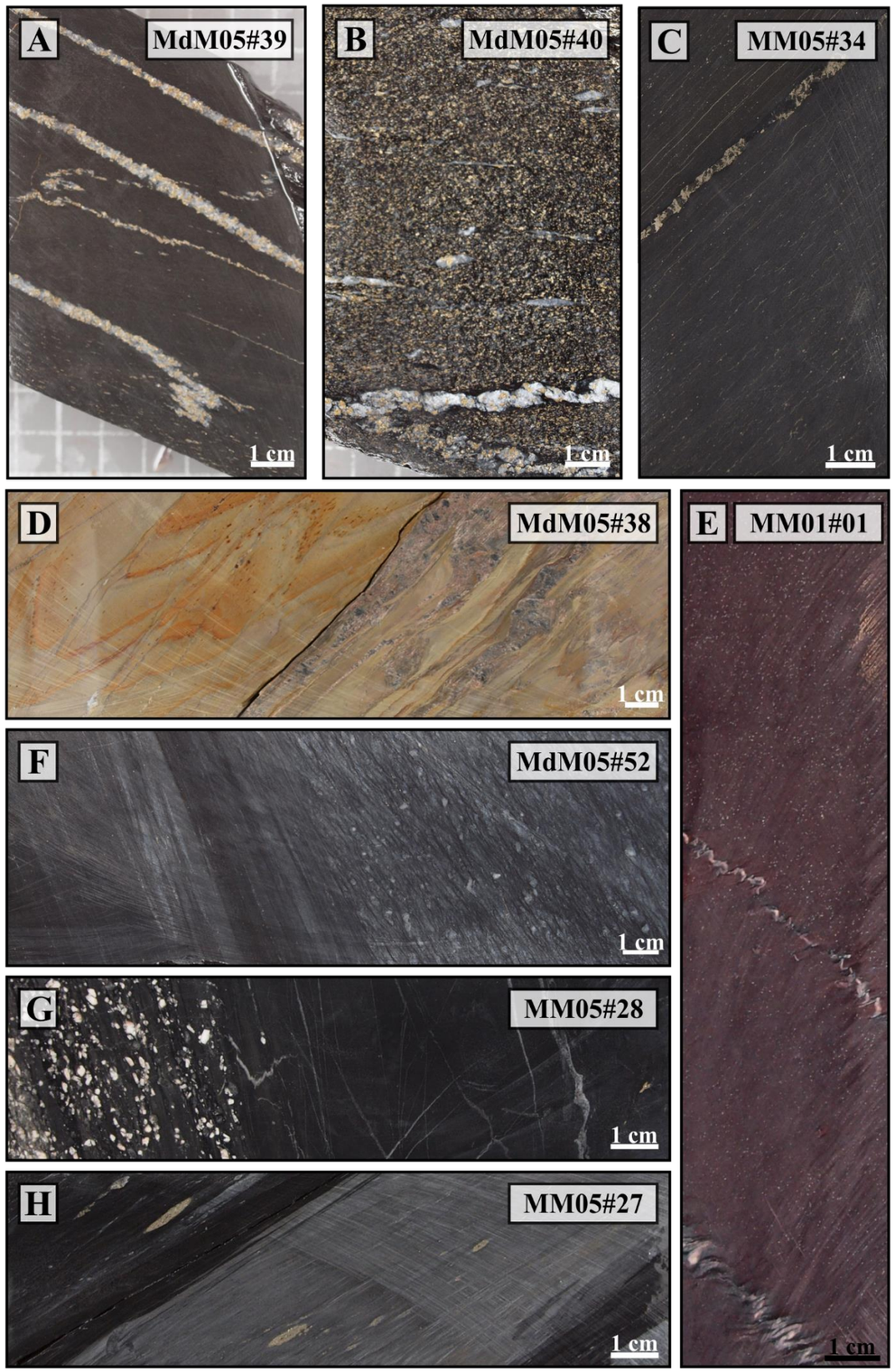

Figure VIII.1 (left)

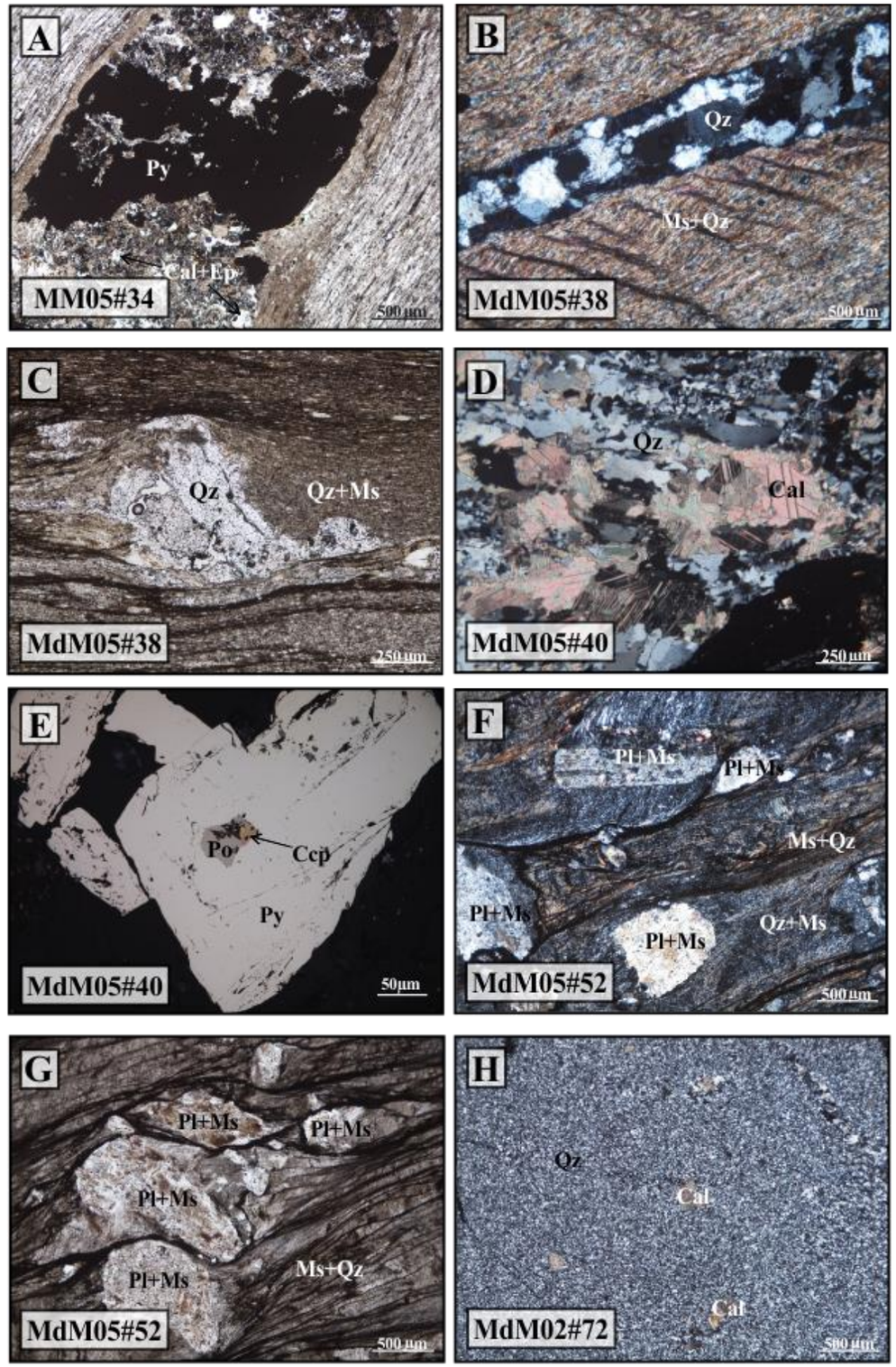

Figure VIII.2 (right)

VIII.2. Felsic Rocks

Felsic metavolcanic rocks are, by far, the most abundant rock type drilled at the Monte das Mesas area, forming two very different textural lithotypes: coherent rocks and volcaniclastic rocks. These rocks are frequently inter-fingered and the predominance of either one is variable. Some altered coherent lavas display textures roughly similar to those typical of volcaniclastic terms, but the observed arrangements are simply the result of patchy alteration and/or fracture-controlled alteration.

VIII.2.1. Coherent Rocks

Macroscopically, the lava facies is characterized by a (light to) dark green coloration, which results from the secondary mineral assemblage, namely fine dissemination of sericite and chlorite, occasionally coupled by epidote. Some lavas have a red to purple colorations, denoting Fe (hydr)oxides impregnations. Nevertheless, all the lava terms have a very fine to intermediate granularity and display abundant feldspar and quartz phenocrysts (however in variable amounts).

The petrographic analysis revealed that these lavas can also be subdivided into three major compositional groups: (i) meta-rhyolites, (ii) meta-rhyodacites and (iii) meta-dacites (these classifications are based on dominant characteristics (*e.g.* relative proportion between quartz, alkali feldspar and plagioclase) and, although three groups were considered, they often show transitional characteristics).

All the three major compositional groups are present in both the north and south drilling clusters. However, the northern cluster shows a predominance of meta-riolitic lavas whereas the southern cluster displays higher abundance of riodacitic to dacitic compositions.

Northern Cluster

The most ubiquitous hallmark is (micro)porphyritic texture, presence of euhedral-subhedral to slightly rounded quartz and feldspar phenocrysts dispersed in a much finer grained (also quartz + feldspar) groundmass; however, the original shapes can be modified either by reabsorption primary mechanisms or by extensive alteration. Quartz (micro)phenocrysts have variable size and often display reaction margins, sometimes reaction golfs. Feldspar (micro)phenocrysts, also variable in size, are mostly of plagioclase composition ($Ab_{97.05}An_{1.12}Or_{0.91}$); they preserve evidence of reaction golfs (magmatic reabsorption; *e.g.* MdM01#64) and of heterogeneous progression of hydrolysis reactions, presenting totally or partially substitution by sericite ± chlorite ± carbonates. Some relics still preserve Carlsbad twinning or polysynthetic albite twinning. Flow foliation textures (*e.g.* MM05#26) are also preserved in many cases. The groundmass is frequently cryptocrystalline possibly resulting from devitrification. The igneous quartz present in the matrix show wavy extinction and recrystallization phenomena with coalescence of individual matrix grains resulting in undefined contours.

Most samples show at least one of the following alteration types: (i) sericitic, (ii) chloritic and (iii) carbonatization. However, the alteration intensity and the relative chronology in relation to the metamorphism/deformation peak are variable: pre-, syn- and post-peak, being the first one by far the most frequent.

Sericitization is the most widespread alteration type, often possible to confirm as pre-deformation and usually preceding any carbonate generation (*e.g.* MdM01#69).

Four distinct carbonate generations are present (*e.g.* MdM02#59, MdM01#64, MdM01#65): (1) pre-deformation (and regional metamorphism), associated with plagioclase alteration; (2) pre-deformation (and regional metamorphism), but fracture-controlled and usually bordered by fine-grained muscovite; (3) post-deformation (and regional metamorphism), along late-developed fractures and sometimes associated with fine-grained white mica; and (4) very late stage infilling of interstitial spaces.

The amount of secondary epidote and titanite is noteworthy in several samples, incorporating the accessory mineralogy: zircon (primary), apatite, some sulfides and oxides. The sulfides are sporadic in these samples, usually very fine grained, disseminated or along small venules; the sulfide association is dominated by pyrite along with minor amounts of pyrrhotite, chalcopyrite, sphalerite and galena (MM05#26; MdM02#59). In some cases (*e.g.* MdM01#69), the sulfides are clearly associated to the early-formed (preceding deformation and metamorphism), fractured-controlled carbonates.

Despite the rhyolitic composition of most samples in the northern cluster, there are some riodacites (*e.g.* MM05#30), with feldspatic rich matrix and abundant titanite and epidote.

Figure VIII.3 Photographs of representative mineralogical and textural aspects of the felsic lava group present in the Northern cluster: (A) light green-grey fine-grained rhyodacite(?) presenting very fine Chl; (B) light-green fine-grained rhyodacite(?) with brecciated texture; (C) light colored and fine-grained rhyodacite(?) with brecciated texture due to Chl ± Py veining, displaying a depositional contact with black metapelite; (D) green-grey rhyolite crisscrossed by small fractures with Chl and very fine-grained oxidized sulfides; (E) light grey rhyolite with Qz + Fds phenocrystals in a silica rich groundmass locally including sericite and chlorite; (F) rhyolite Qz (± Fds) phenocrystals in a silica rich matrix presenting Chl (± Py) along discrete (micro)fractures; (G) sericitic and carbonate alteration, Py + Gn + Sp along fractures.

Figure VIII.4 Photomicrographs of particular aspects of the felsic coherent rocks from the Northern cluster: (A) pre-deformation Qz and Pl veining, fine white mica along microfractures; (B) textural rearrangement and magmatic fluency; (C) microporphyroblastic texture, Fds + Chl + Ttn + Ep rich matrix, Qz + Chl + Py venule and disseminated Po; (D) microporphyroblastic texture, groundmass composed by Qz + Fds presenting strong carbonation; (E) microporphyroblastic texture composed by a microphaneritic matrix with pre-deformation fine white mica along microfractures and post-deformation interstitial carbonate, Ms + Cal post-deformation venules; (F) microphaneritic Ms? + Qz + Fds matrix, Qz + Pl + Cal + Ms ante-deformation microfracture infillings; (G) very fine disseminated Sp + Gal + Py + Ccp; (H) Fds relics highly saussuritized (ante-deformation).

.

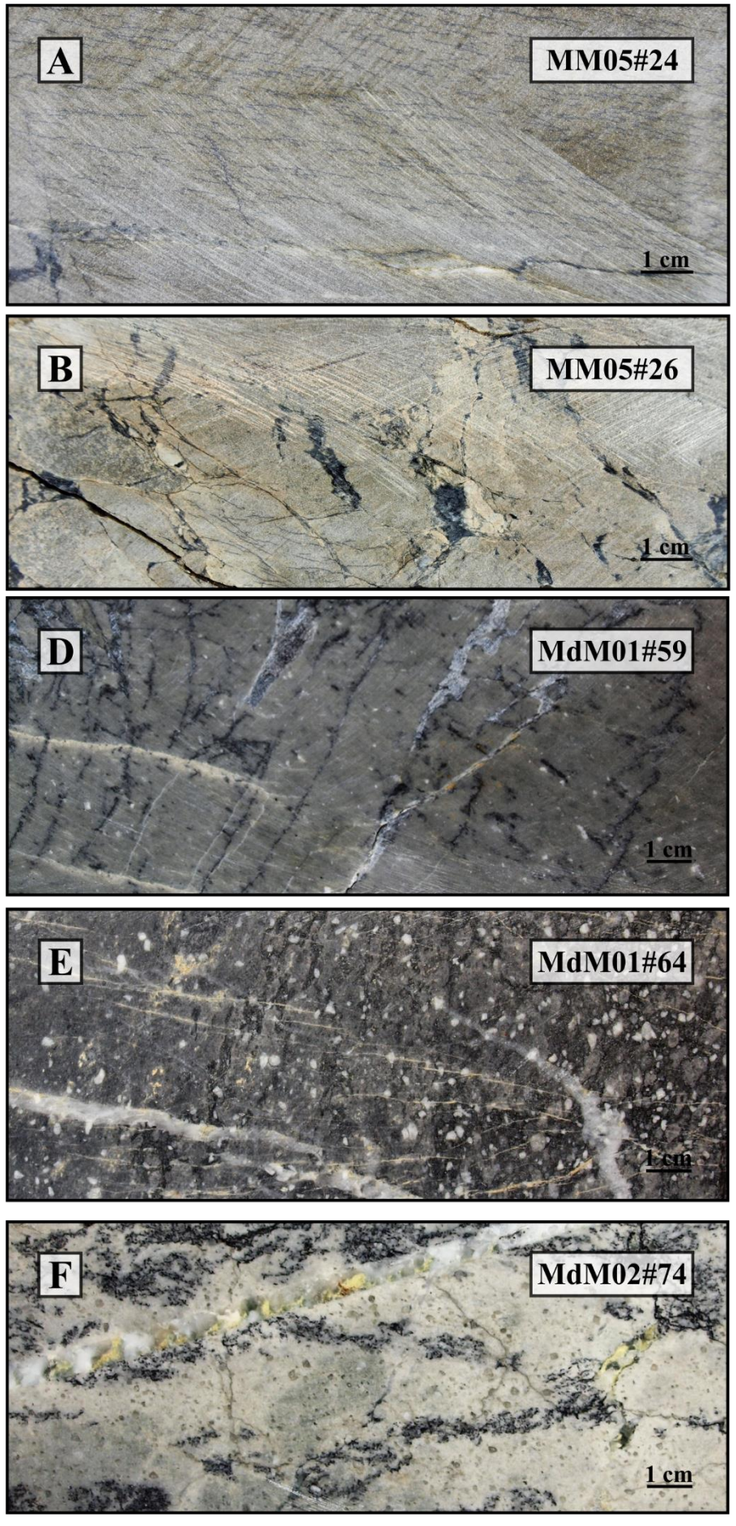

Figure VIII.3 (left)

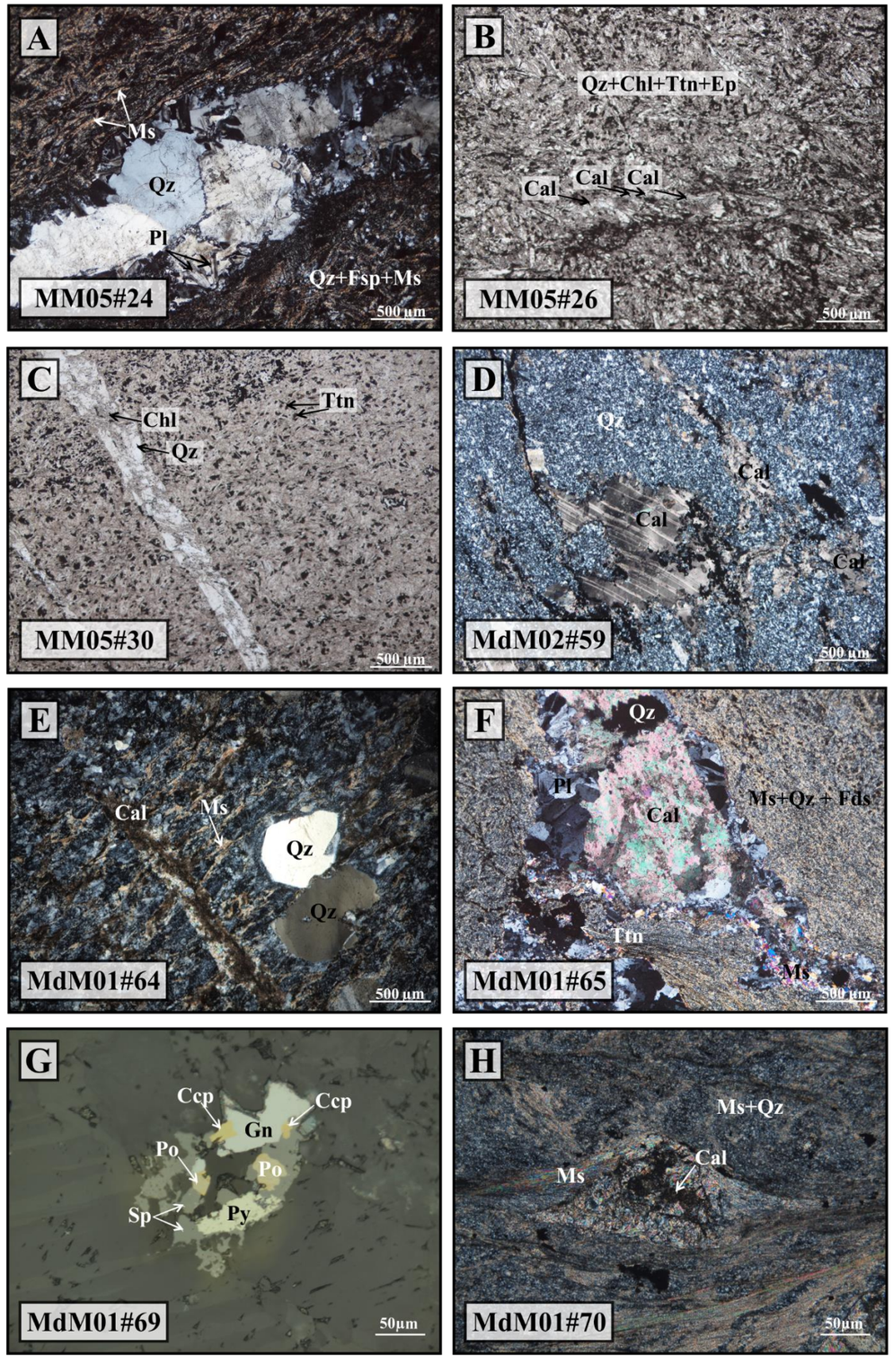

Figure VIII.4 (right)

Southern Cluster

Samples from the southern cluster show a more riodacitic to dacitic composition, despite of similar textural characteristics with those described above. Feldspar s.l. phenocrysts prevail when compared to quartz, once again displaying contrasting degrees of effects due to hydrolysis. All the three types of alteration (sericitic, chloritic and carbonation) are present, however recording distinct intensities throughout the selected group of samples. Hydrothermal alteration in the southern cluster, although similar to what described above, show a slightly more frequent and intensive chloritization, which is usually related to micro-fracture infillings along with carbonates and/or sericite (*e.g.* Z1#9, Z2#15) or to a late stage alteration (post-sericitization and post-carbonate) (*e.g.* MdM05#43).

Rhyolites are also present in the southern cluster, as indicated above, displaying similar textural characteristics to those already described (*e.g.* MdM05#53).

Once again, the amount of epidote and titanite in several samples deserve notice and the accessory mineralogy presenting sulfides (pyrite, chalcopyrite, pyrrhotite) and oxide phases (rutile?).

Figure VIII.5 Photographs of representative mineralogical and textural aspects of the felsic lava group present in the Southern cluster: (A) light-grey rhyolitic rock with Qz + Fsp phenocrysts; (B) dacite showing sericite-rich envelops and small dark chlorite aggregates; (C) dark-grey rhyolite with abundant Fsp ± Qz phenocrysts, dark chlorite tracing a poor-developed foliation; (D) rhyolite presenting brecciated texture due to Chl (± Cb) veining in which some domains are enriched in massive Po ± Py; (E) light greyish rhyodacite with Fsp (± Qz) phenocrysts with evident sericitization ± chloritization; (F) rhyodacite composed by Fsp + Qz phenocrysts in a sericite-rich groundmass crossed by an anastomosed fracture mesh of Chl ± Po that yields brecciated-like texture.

Figure VIII.6 Photomicrographs of particular aspects of the felsic coherent rocks from the Southern cluster:(A) strong chloritization and carbonation; (B) fine white mica along microfractures and Chl + Ms? along discontinuities; (C) matrix composed mostly by Pl and minor amounts of Qz and Tr? porphyroblasts highly retrograded; (D) Po (±Ccp) accompanied by abundant Ep; (E) disseminated Sp plus Po + Py exsolutions and trace amounts of Ccp; (F) microporphyroblastic texture presenting a microphaneritic matrix, Ms + Ep + Ttn along microfractures; (G) strong chloritization; (H) porphyroblastic texture and microphaneritic matrix with abundant Ep + Ttn pre-deformation.

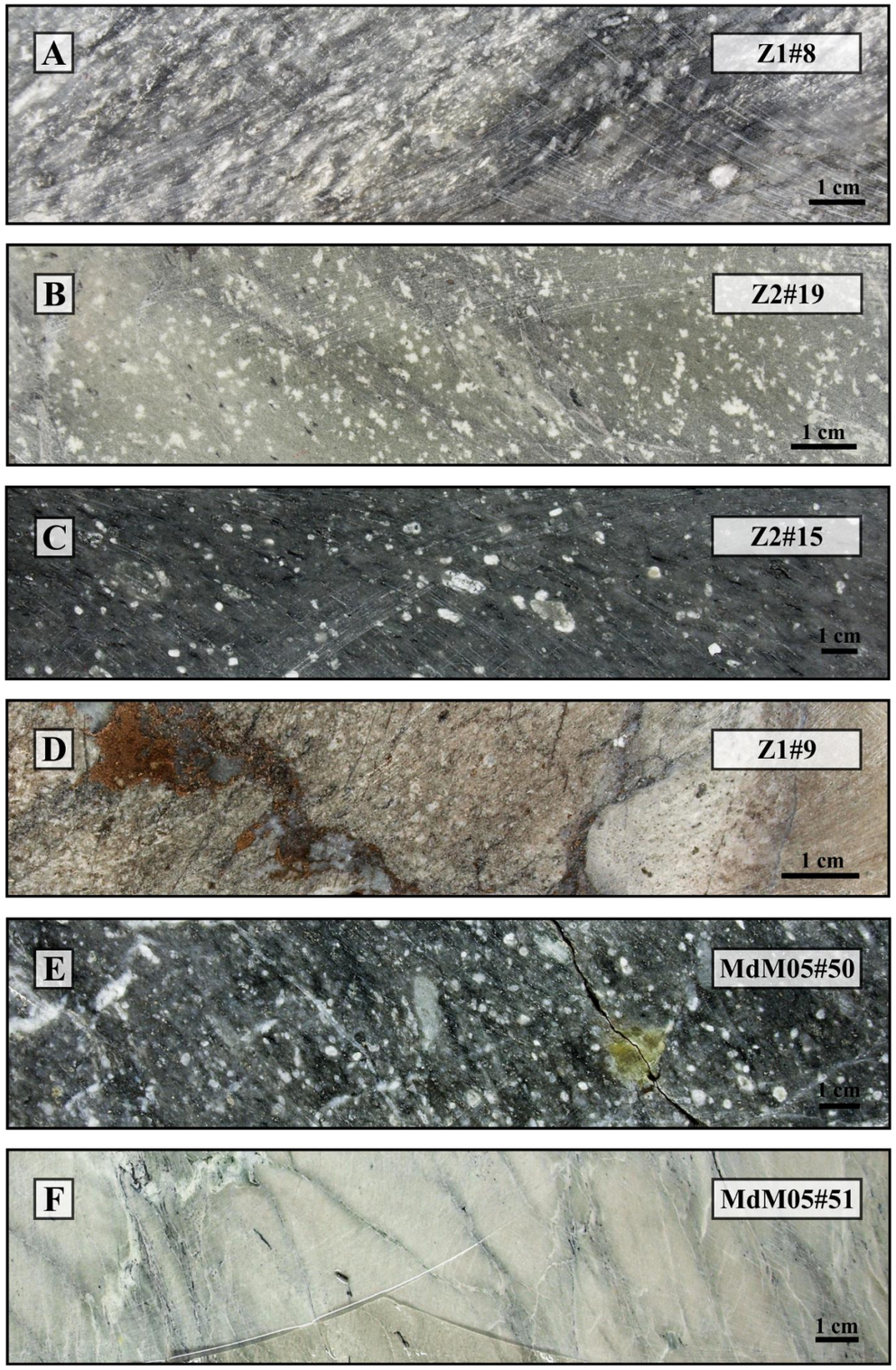

Figure VIII.5 (left)

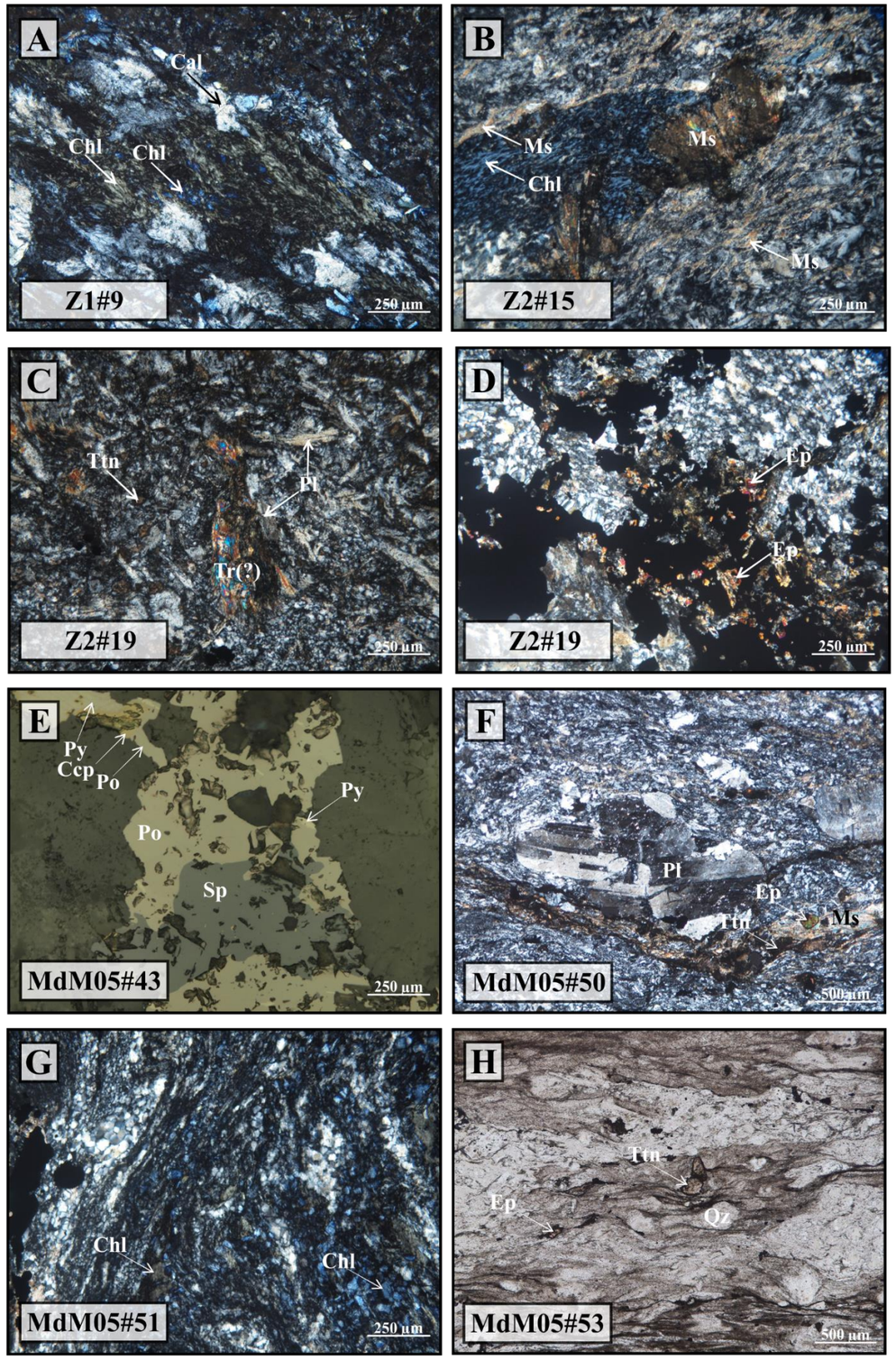

Figure VIII.6 (right)

VIII.2.2. Volcaniclastics

The term *volcaniclastic* is descriptive and applies to accumulations predominantly composed of volcanic-derived particles. The particles may have any shape and size. No specific clast-forming processes, transport and depositional mechanisms or settings are implied (McPhie *et al*., 1993).

The volcaniclastic rocks sampled at Monte das Mesas are characterized by a (light to) dark green coloration, which results from the secondary mineral assemblage, namely sericite, chlorite and epidote. They are mostly poorly calibrated and enriched in quartz and feldspar clasts unevenly distributed with different sizes and shapes, but usually broken and altered. The feldspar clasts show effects of variable hydrolysis intensity. The groundmass of these rocks comprises very fine quartz and fine white mica, developing foliation as a response to subsequent deformation accommodation.

The most common alteration minerals found are sericite (fine-grained muscovite), chlorite, epidote and carbonate; however their chronological relationship is not always possible to infer or varies in between the samples. Yet, in most samples (*e.g.* Z2#18, MdM01#58), hydrothermal alteration has been proved to precede the deformation/metamorphism peak except for some late-developed (quartz, carbonate, feldspar and chlorite) veinlets.

Deformation is mostly expressed as optical effects (wavy extinction), intragranular features (mechanical twinning) or textural arrangements (bent grains, spiral porphyroblasts, foliated secondary minerals wrapped around early porphyroclasts, pressure shadows or fringes, kink bands or micro-folds, or even micro-boudinage) documenting heterogeneous strain accommodation.

Sulfides are very fine grained, disseminated and/or forming infillings of fractured-controlled venules; the sulfide association is mostly composed of pyrite and pyrrhotite with minor to trace amounts of chalcopyrite, sphalerite, galena, marcasite and tetrahedrite-tennantite. In sample Z2#16, foliation (underlined by phyllosilicates) wrapping around sulfide porphyroblasts confirm that deposition of these sulfides preceded the deformation/metamorphism peak.

(Hydro)oxides, most likely hematite, is also frequent in some samples (*e.g.* MdM02#71) developing very fine straws in foliation planes along with phyllosilicates, conferring the rock its reddish color. In some samples, such as MdM02#76, the oxide phases are magnetite-hematite grains that form discontinuous fractured-controlled infillings.

Figure VIII.7 Photographs of representative mineralogical and textural aspects of the felsic volcaniclastic group: (A) inter-fingered layers with unequal abundance of Chl + Ep + Ms with Cb vesicle infillings and lenses subparallel to foliation, also, hematitic venules running subparallel to foliation; (B) discontinuities filled with Qz and Chl accompanied with disseminated Py; (C) strongly foliated (Ms + Chl) matrix with weakly disseminated Po + Py; (D) dark Chl veining with Py + Po masses and disseminated; (E) strong sericitization and chloritization, Qz + Chl veining that crisscross the secondary mineral assemblage tracing a previous alteration event; (F) inter-fingerings between domains with very little and fine volcanogenic component and very fine-grained Py along foliation and developing larger and massive colomorphic aggregates; (G) reddish (oxidized/weathered?) felsic volcaniclastic rock recording silicification of moderate intensity; (H) reddish (Hem rich) domains richer in very fine-grained sulfides (Py ± Apy?).

Figure VIII.8 Photomicrographs of particular aspects of the volcaniclastic group: (A) Qz + Pl porphyroclasts in a strongly foliated very fine white mica ± chlorite (pre-deformation) matrix; (B) Pl porphyroclasts of variable size, highly deformed and altered, in a very chloritized (pre-deformation) matrix; (C) intense chloritization and carbonation; (D) Py + Mrc exsolutions; (E) porphyritic texture composed of Qz + Pl porphyroclasts presenting Fds carbonation, in a (pre-deformation) Ms rich matrix; (F) Volcaniclastic rock with disseminated sulfides (Py+Gal) ; (G) twisted Qz porphyroclasts in a (pre-deformation) fine white mica-rich (±chlorite) matrix; (H) abundant Hem impregnations along late microfractures.

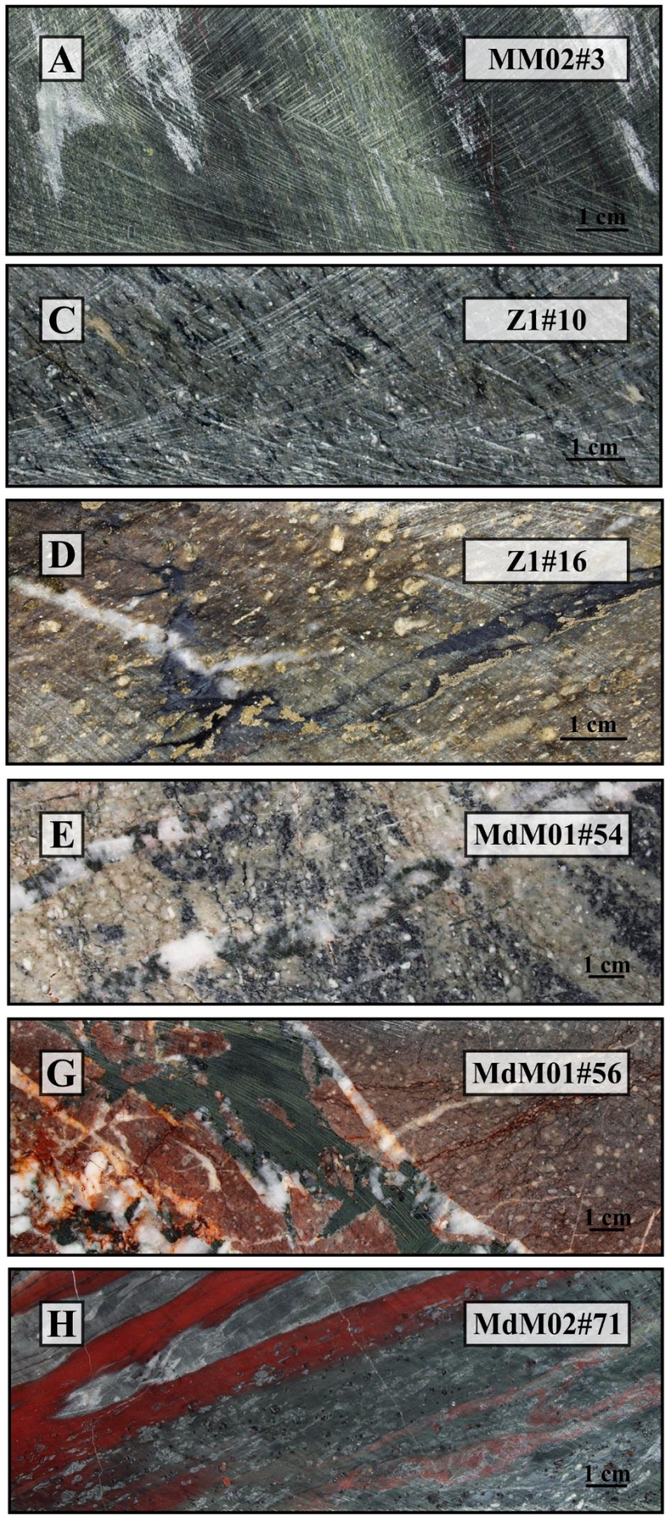

Figure VIII.7 (left)

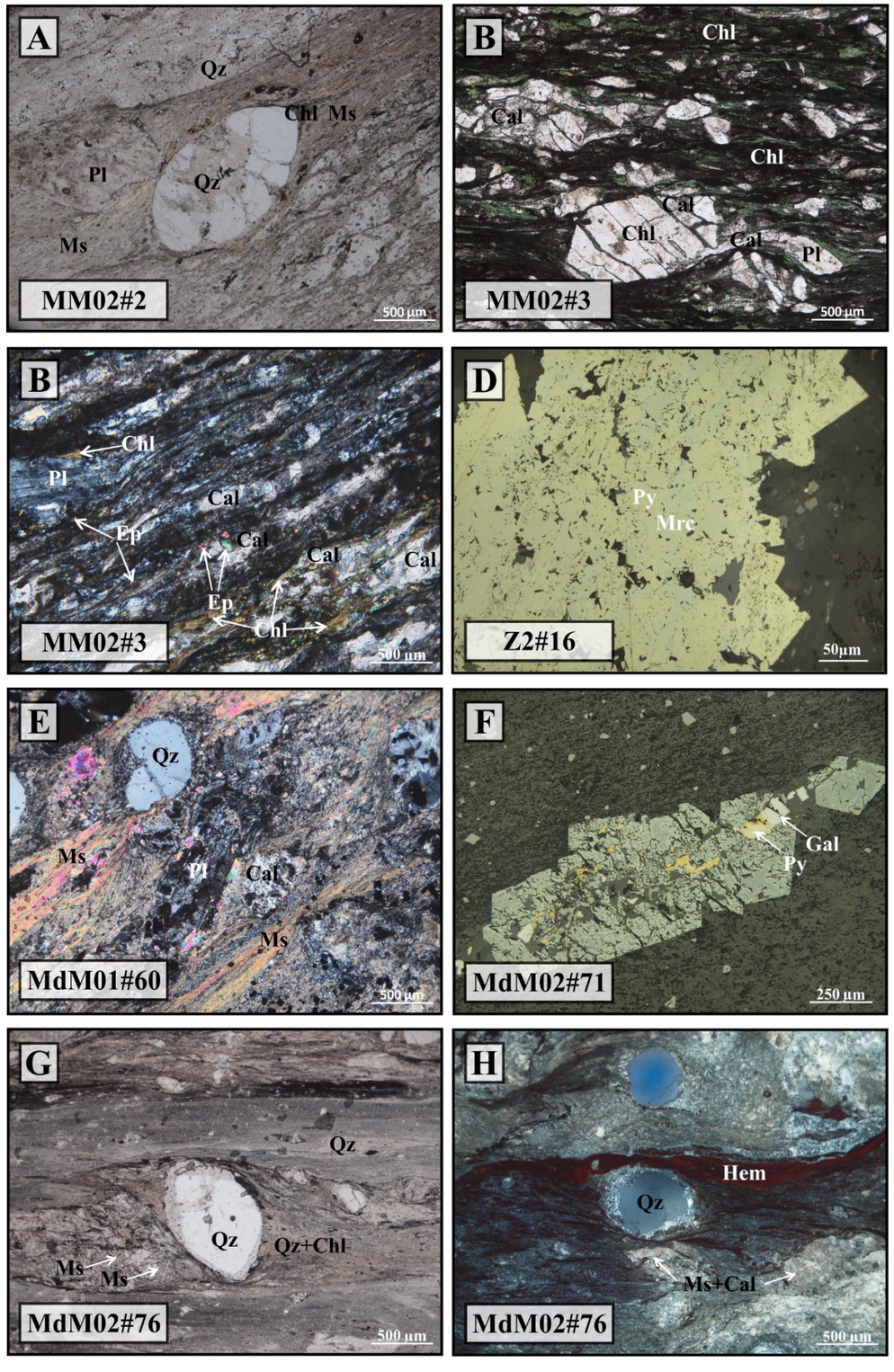

Figure VIII.8 (right)

VIII.3. Intermediate and Mafic Rocks

Once again, these classifications were based on dominant features and often show transition characteristics, for this reason only one main compositional group was considered in this chapter, including rocks with intermediate to mafic composition. However, as in the felsic main group, two very different textural lithotypes can be distinguished, denoting the intrusive or extrusive character.

Extrusive rocks (*e.g.* Z1#07, MdM05#41) present a microphaneritic texture composed mostly of plagioclase with evidence of strong saussuritization; chlorite, titanite, epidote and carbonates are the main secondary mineral phases, conferring the rocks its deep green coloration. Also frequent are clinopyroxene phenocrysts intensively retrograded with changed borders to amphibole (tremolite, hornblende, actinolite?). Some microcrystalline secondary quartz is important, resulting from late silica addition processes; for example, product of hydrolysis processes of the primary mineral phases (feldspar, pyroxene). The mineral assemblage refers to mafic lavas that underwent oceanic metasomatism, i.e. a spilite rock.

The intrusive rocks (*e.g.* MM02#5, MM05#31) display very fine-grained phaneritic textures embodied by almost total pseudomorphs between pyroxene relics and amphibole (actinolite-hornblende?), chlorite, epidote and titanite as the main mineral assemblage. Sericite and carbonate are also present, but significantly less abundant than chlorite. Minor amounts of fine-grained disseminated sulfides (pyrite, pyrrhotite, chalcopyrite) can be observed.

The classification of MdM05#42 sample is ambiguous due to the advanced stage of alteration. This sample preserves a brecciated texture (tectonic, hydraulic?) comprising clasts of variable composition (intermediate to mafic) deeply altered and cemented by a very fine secondary mineral assemblage dominated by chlorite aggregates. Considering the rock foliation (affecting its cement), the growth of secondary mineral assemblage should have occurred before the deformation/metamorphism peak. This rock was tentatively classified as a mafic (possibly of spilitic character) breccia in view of is setting in the re-logged drill-core.

Sample MM02#6 comprises, even though in minor quantities, primary quartz, being classified as intermediate unlike the previous samples, although mineralogically very similar: coherent rock, micro-phaneritic matrix composed of plagioclase (deeply hydrolyzed) and minor quartz, chlorite and epidote, besides relics of clinopyroxene (diopside?) phenocrysts strongly retrograded to amphibole (tremolite?) and chlorite.

Figure VIII.9 Photographs of representative mineralogical and textural aspects of the mafic group: (A) light-green coherent intermediate rock; (B) Pillow-lava structure (?), spilite(?); (C) Fds, titanite(?) and Bt form the original rock that appears to be obliterated by an anastomosed mesh of Se and Chl; (D) moderate chloritization and sericitization, fine sulfides (Py ± Po ± Ccp) usually associated with Chl; (E) strong chloritization and sericitization; (F) pillow-lava structure(?), Cb infillings(?), purplish-reddish domains due to Hem dissemination(?); (G) Chl aggregates frequently accompanied by Po, Cal ± Chl venules with massive Po aggregates, the development of these venules is conceivably controlled by preexistent structural weaknesses.

Figure VIII.10 Photomicrographs of particular aspects of the intermediate to mafic group: (A) microphaneritic texture presenting a slight magmatic fluency (fabric), pyroxene relics showing effects of intense retrograding, two optical different chlorites, however not denoting two different textural relationships or depositional chronological events; (B) microphaneritic texture presenting pyroxene relics in a Fds (± Qz) + Chl matrix with very abundant Ttn + Ep ± Cal; (C) medium grain phaneritic texture preserving pyroxene relics, strong chloritization and disseminated Po; (D) microphaneritic texture composed essentially by Chl + Pl + Ep preserving some retrograded pyroxene relics; (E) intense carbonation and chloritization; (F) Cal + Po filling microfractures (pre-deformation).

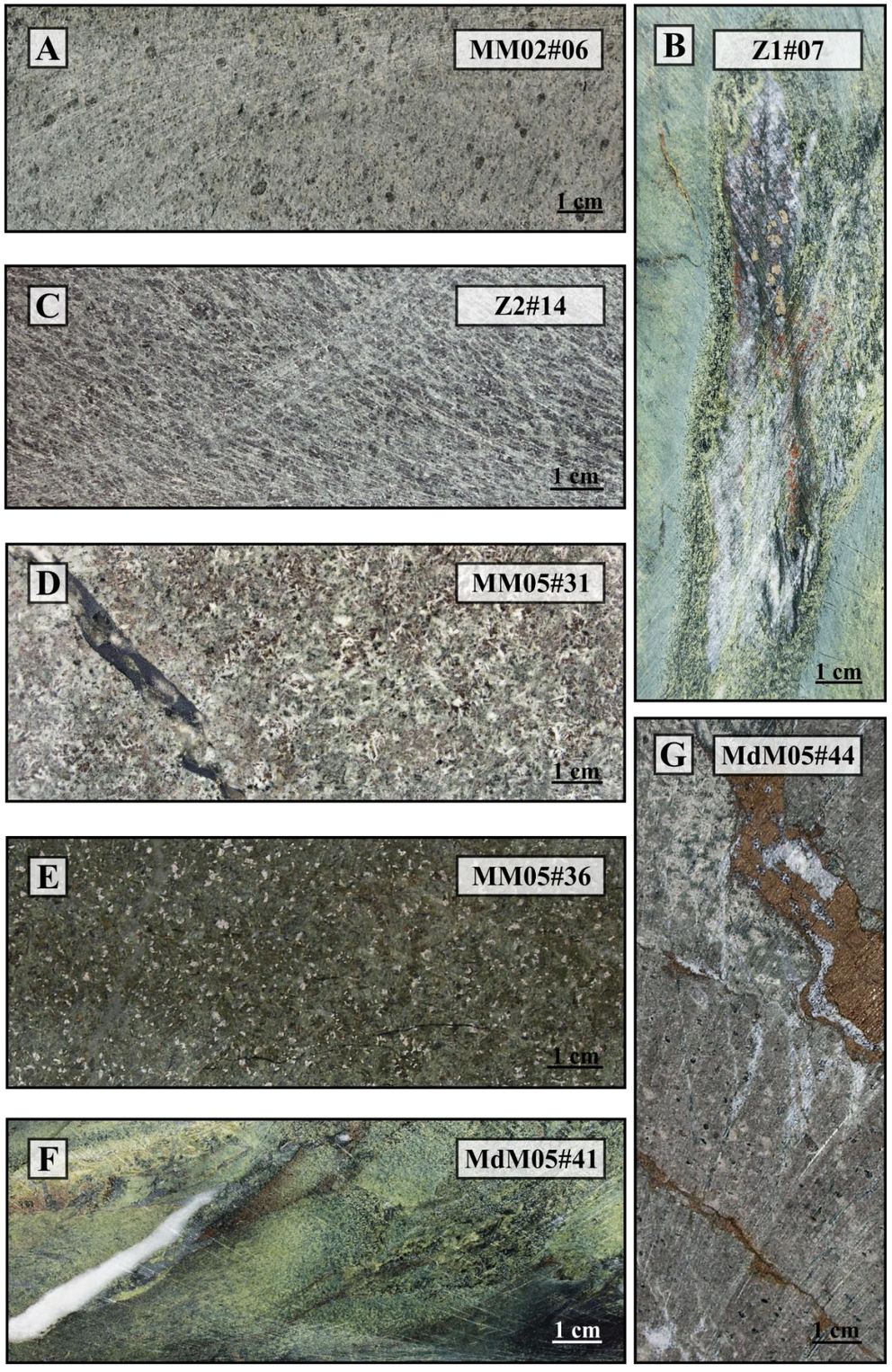

Figure VIII.9 (left)

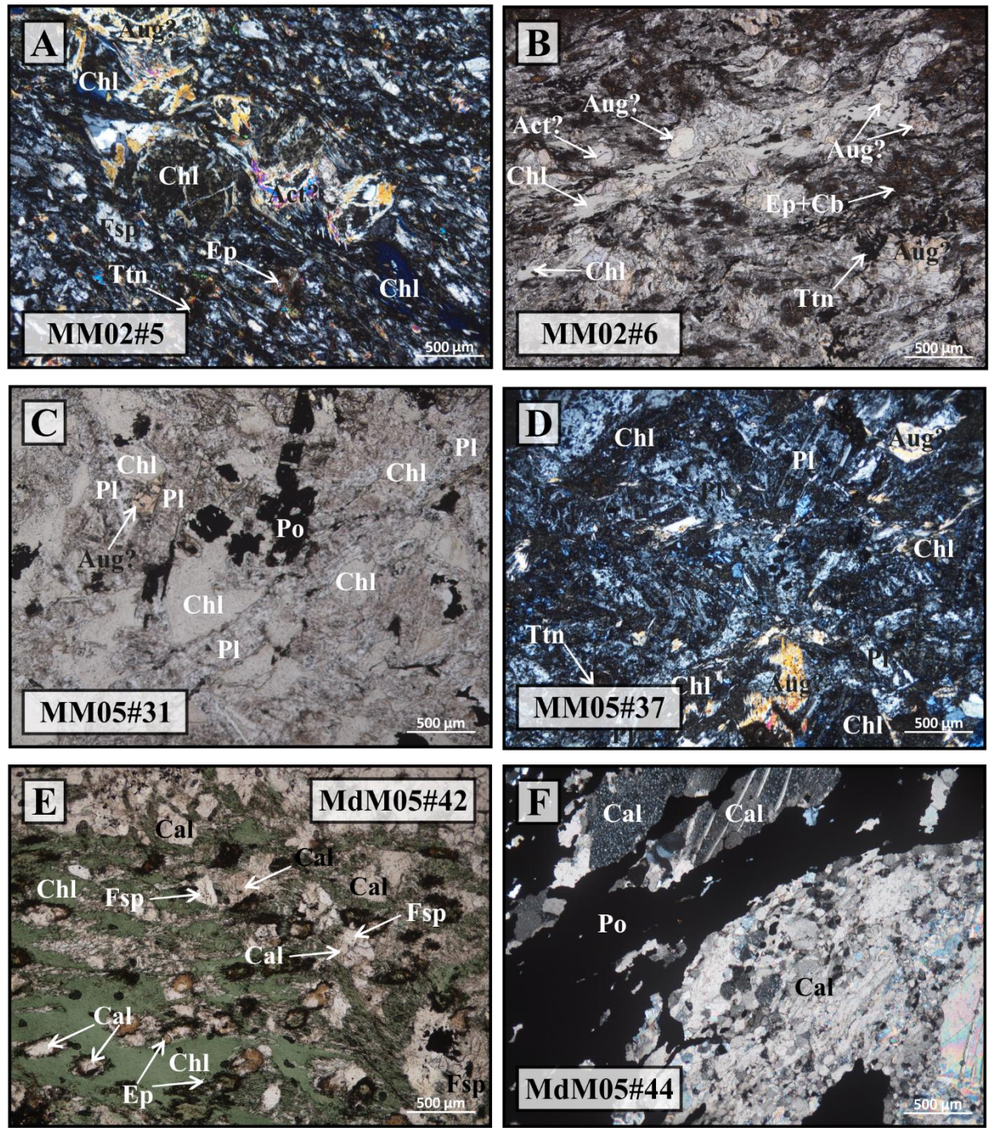

Figure VIII.10 (right)

IX. Mineral Chemistry

This chapter presents the analytical results of mineral chemistry performed at the Electron Microprobe Lab, carried out at FCUL, using a JEOL JXA 8200 equipment under standard analytical conditions (Appendix I). Its aim consists on the report of compositional variations showed by the main mineral phases forming the prevailing lithological groups and, in addition, the chemical variation displayed by secondary mineral assemblages related to the hydrothermal alteration affecting the facies that compose the VSC at Monte das Mesas.

The data processing was based on a C++ program that allowed to: (i) extract the raw data from the control probe workstation; (ii) transform data as weight percentages into atomic percentages; (iii) test the analysis in order to make a preliminary classification of the mineralogical group; (iv) compare the calculated atomic proportions, with internal mathematical models of the stoichiometry of the assumed mineralogical group, while calculating the atomic proportions and the weight masses of the un-analyzable elements, but theoretically present; dividing the elements of multiple valence into the various valences according to the required stoichiometry; and (v) evaluate the quality of the analysis. (Mateus *et al*., 2015).

From the petrographically examined samples, 10 polished thin sections were selected, of which 5 represent the northern cluster and the other 5 the southern cluster. Due to the confidentiality of the data processed in this work, it is not possible to present the analyses performed; however, their main graphical expressions are clear enough to support the fundamental conclusions.

The minerals analyzed include silicates [feldspars, pyroxenes, amphiboles, muscovite, chlorite, epidote, titanite, and zircon], carbonates [calcite and siderite], phosphates [apatite], sulfides [pyrite, pyrrhotite, chalcopyrite, sphalerite, and galena] and oxides [rutile s.l.]. Phyllosilicates are quite important in the characterization of alteration haloes due to hydrothermal processes associated with the genesis of massive sulfides and, for this reason, special attention was paid to this mineral group.

IX.1. Silicate Group

Silicates form most of the primary and secondary mineral assemblages in volcanic rocks. They include feldspar, pyroxene, amphibole, phyllosilicates, epidote, titanite and zircon.

IX.1.1. Feldspar

Feldspar and quartz are the most abundant mineral phases within the analyzed samples. They occur mostly as euhedral to sub-euhedral micro-phenocrysts, and feldspar grains preserve evidence of variable intensity hydrolysis.

Feldspar composition is characterized by the general formula MT_4O_8. Ideally, the tetrahedral position T is filled by Si^{4+} and Al^{3+} cations and the M position is occupied by K^+, Na^+ and Ca^{2+} cations. The feldspar group can be classified on the basis of the ternary system $NaAlSi_3O_8$ (Albite, Ab) - $CaAl_2Si_2O_8$ (Anortite, An) and $KAlSi_3O_8$ (Feldspar K, Or) (Deer *et al*., 2008).

To chemically characterize this mineral group, 119 analyses were performed. Two distinct subgroups were evidenced: (1) the plagioclase group, representing the chemical composition of common micro-phenocrysts present in either in felsic or mafic rocks; and (2) the K-feldspar group, characterizing the prevailing composition of feldspars within the matrix of felsic and mafic rocks.

Table IX.1 Summary of descriptive statistics for the mineral chemistry analyses, in wt%: plagioclase group (n=48).

	MEAN	*STDEV*	*MEDIAN*	*MAX.*	*MIN.*
TiO₂	0,009	0,016	0,000	0,076	0,000
SiO₂	68,035	0,820	68,222	69,347	66,132
Fe₂O₃	0,020	0,066	0,000	0,309	0,000
Al₂O3	19,242	0,362	19,191	20,058	18,544
BaO	0,011	0,027	0,000	0,143	0,000
SrO	0,065	0,054	0,067	0,167	0,000
FeO	0,060	0,097	0,027	0,517	0,000
CaO	0,435	0,399	0,247	1,357	0,000
MgO	0,007	0,018	0,000	0,090	0,000
K₂O	0,113	0,090	0,091	0,561	0,042
Na₂O	11,125	0,372	11,184	11,757	10,120

The plagioclase group average composition is $Ab_{97.05}An_{1.12}Or_{0.91}$.

Table IX.2 Summary of descriptive statistics for the mineral chemistry analyses, in wt%: K-feldspar group (n=71).

	MEAN	*MEDIAN*	*STDEV*	*MAX.*	*MIN.*
TiO₂	0,016	0,000	0,025	0,109	0,000
SiO₂	65,512	65,618	0,762	67,607	63,224
Fe₂O₃	0,033	0,000	0,190	1,563	0,000
Al₂O3	17,960	18,041	0,308	18,442	17,213
BaO	0,214	0,202	0,115	0,669	0,033
SrO	0,001	0,000	0,007	0,055	0,000
FeO	0,089	0,031	0,238	1,667	0,000
CaO	0,034	0,013	0,054	0,325	0,000
MgO	0,014	0,000	0,062	0,418	0,000
K₂O	16,500	16,600	0,326	16,930	15,436
Na₂O	0,166	0,159	0,041	0,325	0,099

The K-feldspar group average composition is $Or_{98.03}Ab_{0.61}An_{0.00}$.

IX.1.2. Pyroxene

Pyroxenes occur as micro-phenocrysts in mafic rocks and present sub-euhedral shapes, usually preserving evidence of retrogression effects to amphibole, chlorite and epidote.

The general formula of the pyroxene group is $[M2M1T_2O_6]$, where T represents the tetrahedral position occupied by Si (and/or Al), and $M1$ and $M2$ octahedral positions, that may or not be occupied by $R^+, R^{2+} and\ R^{3+}$cations; nevertheless, $M1 + M2 = T$ (Morimoto *et al*., 1988). To compositionally sort the analyzed pyroxenes, a quadrilateral projection was used [$Mg_2Si_2O_6$ enstatite, En) – $Fe_2^{2+}Si_2O_6$ (ferro-silite, Fs) - $CaMgSi_2O_6$ (diopside, Di) e $CaFe^{2+}Si_2O_6$ (hedenbergite, Hd)]; according to this classification all the quantitative analyses performed document compositions in the augite field, characterized by $Wo_{46.11}En_{41.66}Fs_{12.23}$ (En%=100Mg/Ca+Mg+ΣFe, Wo%= 100Ca/Ca+Mg+ ΣFe and Fs%= 100 ΣFe/Ca+ Mg+ΣFe, where ΣFe = Fe^{2+}+Fe^{3+}), although showing a small scattering.

Table IX.3 Summary of descriptive statistics for the mineral chemistry analyses, in wt%: pyroxene group (n=7).

	MEAN	*MEDIAN*	*STDEV*	*MAX.*	*MIN.*
TiO₂	0,186	0,188	0,110	0,000	0,244
SiO₂	50,233	50,399	0,246	50,946	50,823
Cr₂O₃	0,283	0,288	0,100	0,404	0,151
Ti₂O₃	1,424	1,367	0,122	1,244	1,175
Al₂O₃	4,568	4,523	0,174	4,334	4,110
BaO	0,000	0,000	0,000	0,000	0,000
ZnO	0,000	0,000	0,040	0,107	0,000
NiO	0,000	0,000	0,000	0,000	0,000
FeO	7,058	7,106	0,338	6,461	7,495
MnO	0,137	0,167	0,024	0,120	0,162
CaO	21,187	21,133	0,073	21,175	21,221
MgO	13,646	13,739	0,191	14,151	13,656
K₂O	0,000	0,002	0,010	0,014	0,028

IX.1.3. Amphibole

Amphiboles occur in dacitic and mafic facies, as "needles" incorporated in the matrix or as micro-phenocrysts, mostly as product of partial or complete pyroxene retrogression.

The general formula for the amphibole group, according to the CNMMN-IMA recommendations, is $AB_2{}^{VI}C_5{}^{IV}T_8O_{22}(OH)_2$ (Leake *et al*., 1997, 2004).

All the 11 amphibole analyses belong to the $(Ca + Na)_B \geq 1$ a.p.u.f. group and are compatible with the actinolite compositional field with $0.70 < Mg/(Mg+Fe^{2+}) < 0.81$; a slight deviation towards the Mg-hornblende composition can be observed.

Table IX.4 Summary of descriptive statistics for mineral chemistry analyses, in wt%: amphibole group (n=11).

	MEAN	*MEDIAN*	*STDEV*	*MAX.*	*MIN.*
TiO₂	0,020	0,018	0,020	0,061	0,000
SiO₂	56,127	55,971	0,884	57,651	54,268
Fe₂O₃	0,152	0,000	0,319	1,062	0,000
Cr₂O₃	0,178	0,224	0,119	0,318	0,019
Al₂O₃	1,318	1,212	0,348	1,900	0,739
ZnO	0,023	0,000	0,033	0,081	0,000
NiO	0,004	0,000	0,011	0,033	0,000
FeO	10,235	10,621	1,653	12,452	7,650
MnO	0,218	0,209	0,072	0,353	0,113
CaO	12,652	12,781	0,474	13,231	11,772
MgO	17,000	16,555	1,072	18,648	15,727
K2O	0,058	0,050	0,027	0,101	0,024
Na2O	0,210	0,157	0,119	0,443	0,113

The average composition of the analyzed amphibole group is $(Ca_{1.91}Na_{0.06}K_{0.01}Fe^{2+}_{0.01}Mn^{2+}_{0.01})_2(Mg_{3.49}Fe^{2+}_{1.27}Al_{0.13}Cr_{0.03}Mn^{2+}_{0.01})(Si_{7.94}Al_{0.06})O_{22}(OH)_2$.

IX.1.4. Dioctahedral potassium mica group

Usually labbeled as muscovite (or sericite when finely granular), this white mica is the main alteration phase found in felsic volcanic rocks as a result of oceanic metasomatism and/or orogenic metamorphism and/or hydrothermal activity accompanied, or not, by sulfide deposition. In the latter situation, its abundance and composition may be used to indicate more proximal or distal locations relative to the mineralizing system.

The very reduced size of most of the sericite crystals – smaller than the electron beam diameter - resulted in poor-quality quantitative analyses, the obtained composition reflecting mostly mixtures of fine-grained chlorite + sericite + quartz; these analyses were not further processed. Despite of these difficulties, 30 analyses were considered good enough to support additional studies, after categorized according to their textural context and/or relative chronology.

Petrographic characterization allowed the distinction between early formed (pre-deformation) and late formed (post-deformation) sericite, in some different textural contexts. However, during this work stage only the following subgroups were suitably analyzed: (1) pre-deformation and composing the rock matrix; (2) within veinlets; (3) replacing feldspar micro-phenocrysts; (4) co-existing with sulfides; and (5) post-deformation and forming the rock matrix.

The general dioctahedral mica group formula of can be written as $(R^+)^{xii}(R^{3+}_{2-x}R^{2+}_x[])^{vi}(R^{4+}_{3+x}R^{3+}_{(1-x)})^{iv}O_{10}(OH)_2$ (Radoslovich, 1960; Velde, 1967; Bailey, 1984, in Mateus, 1996). Most chemical variations in dioctahedral potassium micas can be explained and represented by two major cationic substitution mechanisms: (i) the Tschermak substitution vector, written as $(R_{2+})^{vi}Si^{iv}Al^{vi}_{-1}Al^{iv}_{-1}$ and, (ii) and the Illitic substitution vector, written as $Si^{iv}_{+1}[]^{xii}_{+1}Al^{iv}_{-1}R^{+xii}_{-1}$.

Table IX.5 Summary of descriptive statistics for mineral chemistry analyses, in wt%: pre-deformation mica group (n=23)

	MEAN	*MEDIAN*	*STDEV*	*MAX.*	*MIN.*
TiO_2	0,265	0,301	0,202	0,646	0,000
SiO_2	49,526	49,428	0,859	51,536	48,116
Fe_2O_3	0,776	0,000	1,650	5,243	0,000
Mn_2O_3	0,001	0,000	0,005	0,025	0,000
Cr_2O_3	0,273	0,066	0,391	1,350	0,018
Al_2O_3	28,876	28,370	1,471	31,790	26,640
BaO	0,098	0,087	0,054	0,208	0,009
FeO	3,164	3,665	1,740	5,333	0,000
MnO	0,016	0,000	0,021	0,061	0,000
CaO	0,200	0,077	0,514	2,523	0,000
MgO	2,309	1,916	1,333	7,491	1,021
Cs_2O	0,002	0,000	0,004	0,016	0,000
K_2O	10,787	10,993	0,770	11,475	8,485
Na_2O	0,095	0,067	0,085	0,375	0,019

Table IX.6 Summary of descriptive statistics for mineral chemistry analyses, in wt%: post-deformation mica group (n=6)

	MEAN	*MEDIAN*	*STDEV*	*MAX.*	*MIN.*
TiO_2	0,433	0,181	0,114	0,456	0,181
SiO_2	49,633	49,795	0,429	50,405	49,200
Fe_2O_3	0,000	0,000	0,000	0,000	0,000
Mn_2O_3	0,000	0,000	0,000	0,000	0,000
Cr_2O_3	0,095	0,066	0,184	0,527	0,051
Al_2O_3	29,809	28,361	0,738	29,809	27,766
BaO	0,028	0,048	0,037	0,108	0,025
FeO	4,115	4,182	0,313	4,646	3,733
MnO	0,073	0,048	0,026	0,073	0,000
CaO	0,022	0,000	0,020	0,048	0,000
MgO	1,929	2,181	0,115	2,181	1,923
Cs_2O	0,000	0,000	0,000	0,000	0,000
K_2O	10,780	11,470	0,375	11,528	10,689
Na_2O	0,050	0,117	0,025	0,117	0,050

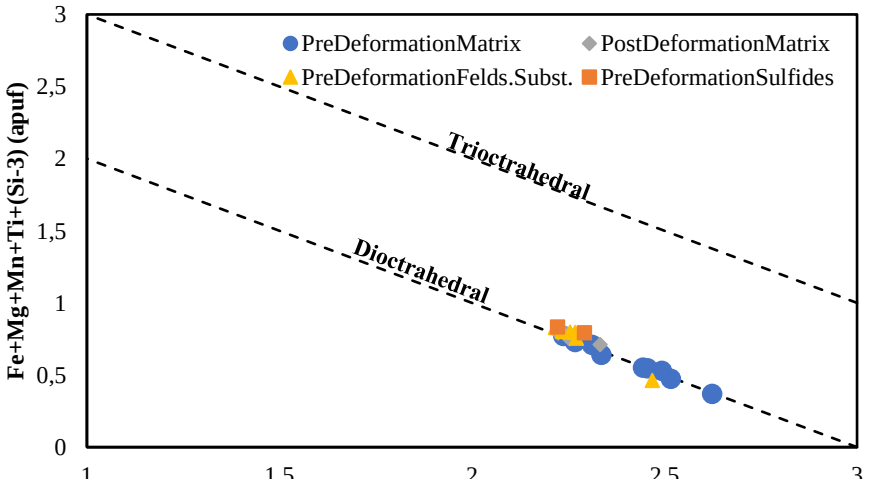

Figure IX.1 $R^{3+} versus\ Fe + Mg + Mn + Ti + (Si - 3)$ plot showing deviations between dioctahedral and trioctahedral compositions.

Figure IX.1 show almost no deviation from the dioctahedral ideal composition proving that the third octahedral position is rarely occupied. The $Al^{iv} versus\ Al^{vi}$ plot (

Figure IX.2.) shows in addition that Al is rather incorporated in octahedral positions due to minor deficiencies of Si^{iv} and/or low amounts of R^{2+}cations, thus justifying the plot of analyses between the muscovite – phengite line deviating towards ferri-phengite. However, these deviations towards the ferri-phengite composition are misleading because there is no evidence to support the incorporation of $Fe^{3+}$and the existence of vacancies in dodecahedral and octahedral positions are not taken it to account in this graphical representation. Figure IX.3 shows the deviation caused by the illitic substitution vector

over compositions described by the solid solution between the end-members muscovite and phengite. This suggests a significant chemical readjustment of the analyzed micas after their growth and/or the development of illite/muscovite interstratifications. The analyses obtained show a very similar composition regardless of their lithological, textural or chronological context; for example, the median composition of pre-deformation sericite can be written as $(K_{0.939}Na_{0.01}Ca_{0.01})^{xii}(Al_{1.56}Mg_{0.19}Fe_{0.19}Ti_{0.02})^{vi}(Si_{3.31}Al_{(0.69)})^{iv}O_{10}(OH)_2$ whereas for post-deformation sericite we get $(K_{0.977}Na_{0.01})^{xii}(Al_{1.59}Mg_{0.20}Fe_{0.24}Ti_{0.01})^{vi}\left(Si_{3.33}Al_{(0.67)}\right)^{iv}O_{10}(OH)_2$.

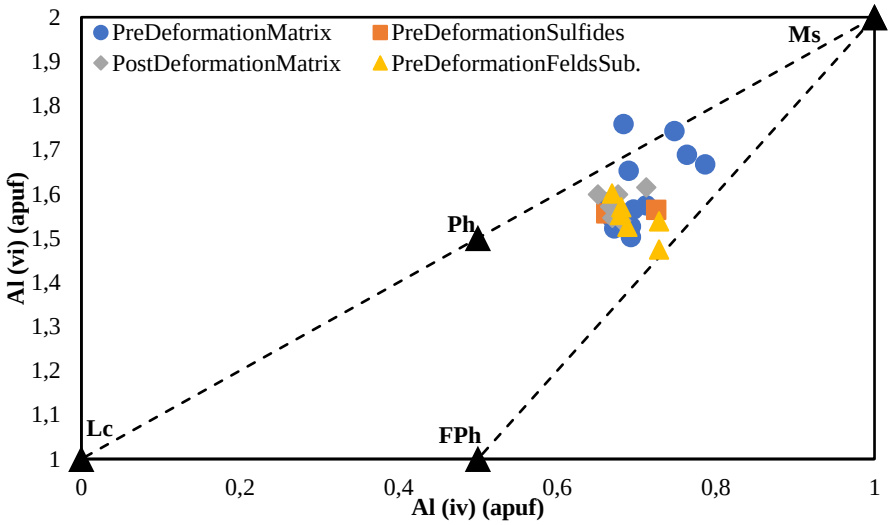

Figure IX.2 Plot of the Tschermak substitution vector for micas, differentiating their textural and chronological context. The compositional end-members where defined by the following ideal compostions: moscovite (Ms) $KAl_2(Si_3Al)O_{10}(OH,F)_2$, phengite (Ph) $K(Al_{1.5}R^{2+}_{0.5})(Si_{3.5}Al_{0.5})O_{10}(OH,F)_2$, leucophyllite (Lc) $K(MgAl)Si_4O_{10}(OH,F)_2$, and Ferri-phengite (FPh) $K(Mg_{0.5}Fe^{2+}_{0.5})(Al,Fe^{3+})(Si_{3.5}Al_{0.5})O_{10}(OH,F)_2$. Abbreviations according to Whitney and Evans (2010).

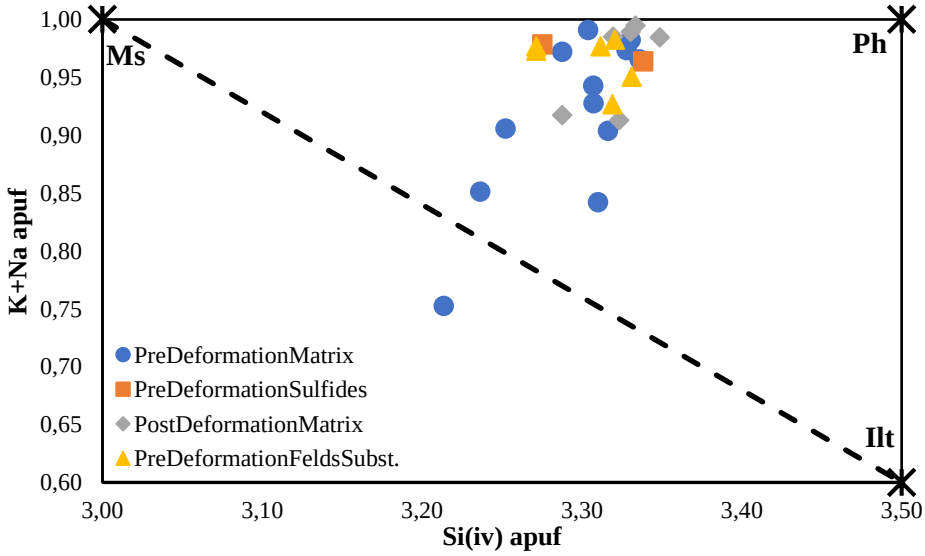

Figure IX.3 Plot of the Illitic substitution vector for micas, differentiating their textural and chronological context. The compositional end-members where defined by the following ideal compostions: moscovite (Ms) $KAl_2(Si_3Al)O_{10}(OH,F)_2$, (Ph) $K(Al_{1.5}R^{2+}_{0.5})(Si_{3.5}Al_{0.5})O_{10}(OH,F)_2$ and illite (Ilt) $K_{0.6}(H_3O)_{0.4}Al_{1.3}Mg_{0.3}Fe^{2+}_{0.1}Si_{3.5}O_{10}(OH)_2.(H_2O)$. Abbreviations according to Whitney and Evans (2010).

IX.1.5. Chlorite

Petrographic criteria allowed distinguish early formed (pre-deformation) and late formed chlorites (post-deformation) and, texturally, it is possible to subdivide these phyllosilicates into the following subgroups: (1) composing the rock matrix, mostly fracture-controlled; (2) within veinlets; (3) replacing micro-phenocrysts of feldspar, pyroxene or amphibole; and (4) associated with sulfides. The relative chronology for many chlorite aggregates was not possible to determine without ambiguity.

The very reduced size of most of the chlorite crystals – smaller than the electron beam diameter - resulted in poor-quality quantitative analyses, often documenting mixtures between fine-grained chlorite + sericite + quartz. These mixed-compositions were not further processed, remaining 102 analyses of enough quality to further investigate.

The general formula for chlorite group is $\left[R^{2+}_{(6-x-3y)}(R^{3+},R^{4+})_{(x+2y)}[\quad]_y\right]^{vi}[Si_{4-x}Al_x^{3+}]^{iv}O_{10}(OH)_8$ with $R^{2+}=Mg,Fe^{2+},Mn,Ni;Zn;\ R^{3+}=Al,Fe^{3+},Cr$ and $x\sim1-3$ (*e.g.* Bayliss, 1975; Laird, 1988). This formula can be simplified as $(Mg,Fe^{2+},Fe^{3+},Mn,Al)_6[(Si,Al)_4O_{10}](OH)_{16}$, fitting an ideal structure defined by regular alternations of octahedral "brucite-like" sheets and tetrahedral-octahedral-tetrahedral sheets in a 1:1 proportion (Deer *et al*., 2008).

Table IX.7 Summary of descriptive statistics for mineral chemistry analyses, in wt%: pre-deformation chlorite group (n=84).

	MEAN	***MEDIAN***	***STDEV***	***MAX.***	***MIN.***
TiO₂	0,016	0,003	0,029	0,195	0,000
SiO₂	27,644	28,051	1,970	32,670	24,248
Fe₂O₃	0,919	0,000	3,250	16,170	0,000
Mn₂O₃	0,005	0,000	0,027	0,166	0,000
Cr₂O₃	0,085	0,072	0,046	0,264	0,020
Al₂O₃	18,923	19,167	1,060	20,489	14,810
ZnO	0,052	0,039	0,047	0,186	0,000
NiO	0,024	0,017	0,024	0,098	0,000
FeO	24,720	22,034	9,938	40,428	0,000
MnO	0,241	0,223	0,098	0,472	0,000
MgO	16,003	19,430	6,534	25,943	4,403

Table IX.8 Summary of descriptive statistics for mineral chemistry analyses, in wt%: post-deformation chlorite group (n=18).

	MEAN	***MEDIAN***	***STDEV***	***MAX.***	***MIN.***
TiO₂	0,018	0,005	0,046	0,200	0,000
SiO₂	28,554	28,529	0,444	29,280	27,757
Fe₂O₃	0,000	0,000	0,000	0,000	0,000
Mn₂O₃	0,000	0,000	0,000	0,000	0,000
Cr₂O₃	0,242	0,082	0,291	1,033	0,026
Al₂O₃	18,448	18,166	0,704	19,808	17,412
ZnO	0,052	0,032	0,049	0,155	0,000
NiO	0,011	0,003	0,014	0,051	0,000
FeO	19,710	18,538	2,069	22,519	17,135
MnO	0,242	0,252	0,040	0,305	0,125
MgO	20,887	21,365	1,018	22,273	19,281

The chemical variation in chlorites can be explained by three major cationic substitution mechanisms (Zane *et al.*, 1998): (i) FM substitution, given by $[Fe^{2+}]^{vi}Mg^{vi}_{-1}$, where both cations occupy the octahedral position; (ii) Tschermak (TK) substitution, written as $Al^{iv}Al^{vi}Si^{iv}_{-1}(Mg, Fe^{2+})^{vi}_{-1}$, where the incorporation of Al^{3+} in the octahedral position (instead of a R^{2+} cation) is balanced by the substitution of Si^{4+} by Al^{3+} in the tetrahedral position; and (iii) dioctahedral substitution (AM), given by $3(Mg, Fe^{2+})^{vi}[\ \ ]^{vi}_{-1}Al^{vi}_{-2}$, responsible for the opening of vacancies in the octahedral coordination position $([\ \ ]^{vi})$; these mechanisms are sensitive to temperature and pressure conditions, as well as to the local chemical gradients. Other substitutions are possible, involving $Fe^{3+}, Mn^{2+}; Ti, V, Cr$ or Ni, however usually less important and/or frequent.

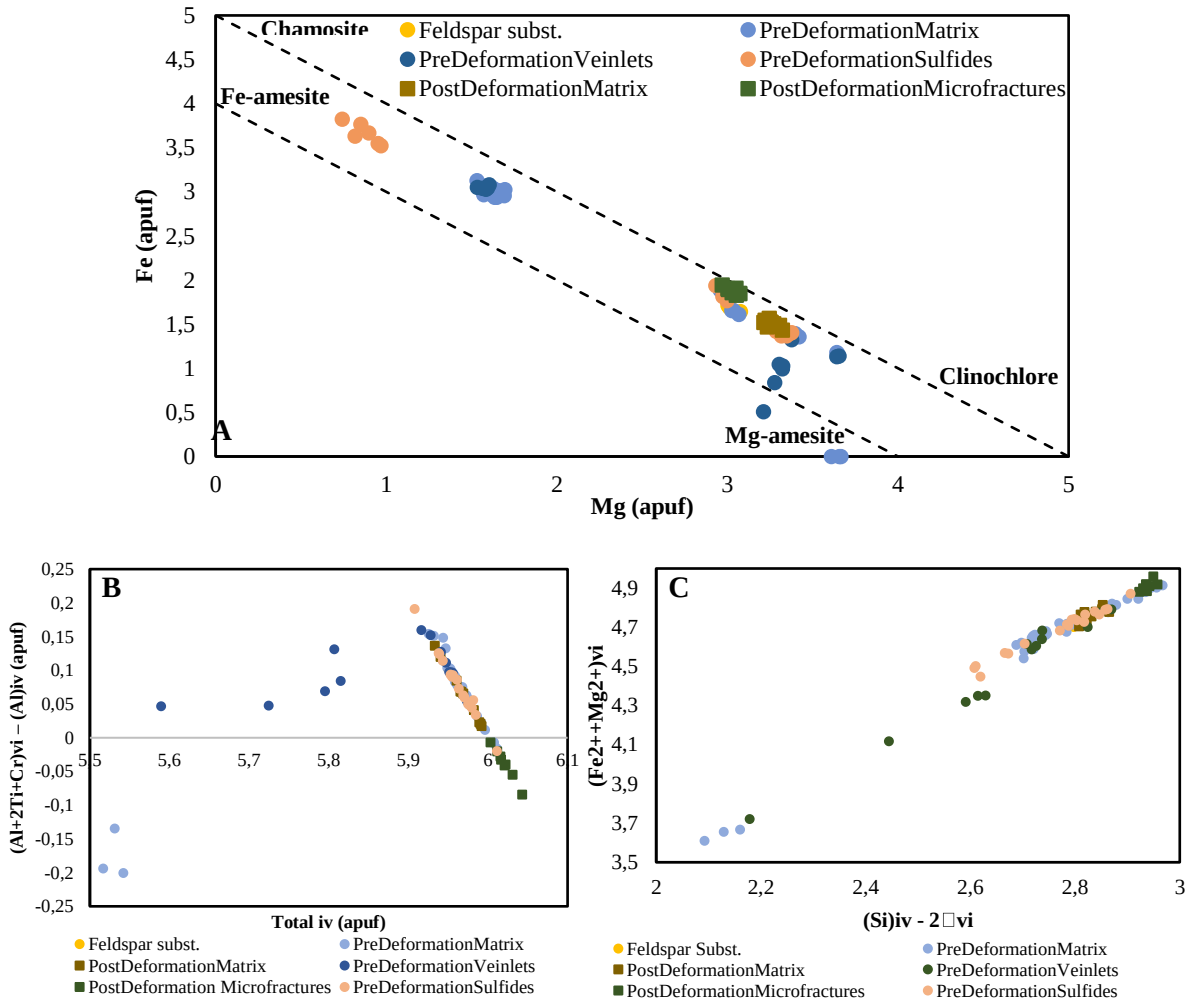

Figure IX.4 A) Projection of the FM substitution vector. B) Plot of Tschermak (TK) substitution vector. C) Plot of Dioctahedral (AM) substitution vector

Figure IX. A, illustrates the scattering of the analyzed chlorites, showing that they are clustered in three distinct compositional groups, the first closest to the clinochlore ideal composition and the third to the chamosite ideal composition. However, it is not possible to relate the compositional enrichment in Fe or Mg with their lithological or textural context, or even to their relative chronology (pre- or post-deformation). Still, the chemical variation presented by most of the chlorite analyses (to a great extent reflecting local chemical gradients) can be explained by a good covariation between Fe^{2+} and Mg; most analyses are characterized by low Fe concentrations, in relation to Mg, however there are two groups that express higher concentrations, particularly the group directly associated with the sulfides present in

sample MdM02#72. Nevertheless, there is a clear composition deviation relatively to the ideal clinochlore - chamosite binary line $[(Mg_5Al)(Si_3AlO_{10})OH_8] - [(Fe_5^{2+}Al)(Si_3AlO_{10})OH_8]$, that may indicate other mechanisms in the partition of di- and trivalent cations.

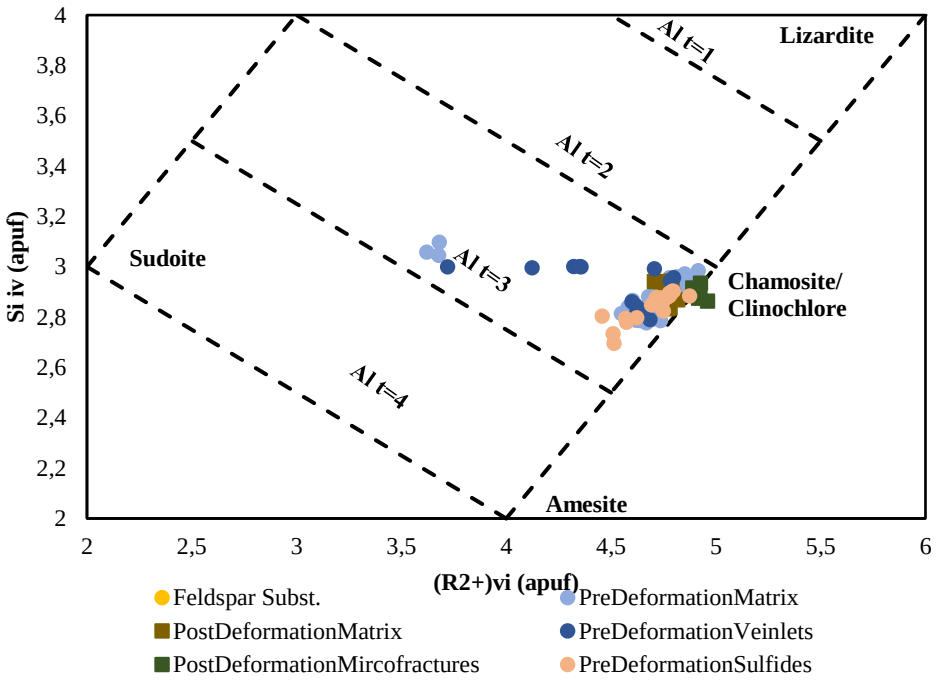

Figure IX.5 Plot of the total divalent cations present in octahedral positions vs. Si in tetrahedral positions. The ideal composition of end-members are lizardite-minnesotaite $[Mg_6(Si_4O_{10})(OH)_8]$, chamosite-clinochlore $[((Mg,Fe^{2+})_5Al)(Si_3AlO_{10})(OH)_8]$, sudoite $[(Mg_2Al_3)(AlSi_3)O_{10}(OH)_4]$, and amesite $[(Mg_4Al_2)(Al_2Si_2)O_{10}(OH)_8]$.

Figure IX.4B and Figure IX.4C prove that both Tschermak (TK) and dioctahedral (AM) substitution occur, generating enrichment in Al^{iv}, causing deviations towards the amesite composition and opening vacancies in octahedral positions, respectively. Figure IX.5 illustrates the deviations towards the amesite ideal composition, with octahedral position completely full (equal 6), as the chamosite/clinochlore component, however, with different R^{2+} and R^{3+} proportions. Deviations towards the sudoite ideal composition are also observed with the octahedral positional partialy full (equal 5).

The chemical composition variation of chlorite represents a potential geothermometer, as its composition records information about physicochemical conditions during its formation.

Numerous authors have noted a systematic decrease in Si^{iv} and $[]^{vi}$ (or conversely an increase in Al^{iv} and $\sum^{iv}$, respectively) in chlorites with increasing depth in diagenetic and geothermal systems or with increasing grade of metamorphism in metamorphic rocks (Cathelineau and Nieva, 1985; Cathelineau, 1988) reasoning that these compositional changes resulted from the progressive increase of chlorite temperature formation. Subsequently, several authors (*e.g.* Kranidiotis and MacLean, 1987; Jowett, 1991; Zang and Fyfe, 1995) improved these empirical geothermometers, accounting the influence of cationic exchanges in octahedral position, reflected in the $Fe^{2+}/(Fe^{2+}Mg)$ ratio. The corrections proposed by Kranidiotis and MacLean (1987) and Zang and Fyfe (1995) provide acceptable results if chlorite growth occurred in an alumina-saturated environment. Conversely, the correction indicated in Jowett (1991) can be used without constraints, yielding more robust results. The empirical approach, although satisfactory under certain circumstances (particularly when applied to active geothermal systems), presents several problems when applied to paleosystems since it is only valid for neoformed

chlorites in equilibrium with the fluid. Nevertheless, if used with the required caution, this approach can provide preliminary indications on the temperature conditions under which chlorites were formed (Caritat, 1993).

The thermodynamic approaches, also reveal inaccuracies due to accumulated uncertainties involving (i) the PT data used in model calibrations; (ii) difficulties due to unknown thermodynamic properties of several end-members forming the solid solutions; (iii) uncertainties related to the most appropriate model for distributing cationic contents among the various coordination positions; and (iv) problems in accurate measurements of Fe^{3+}content, as well to decide the best way to consider them in solid solution models (Grosh *et al*., 2012). Still, several thermodynamic geothermometers have been developed and proved useful, for example, Walshe (1986), Vidal *et al*. (2001, 2005, 2006), Inoue *et al*. (2009), Bourdelle *et al*. (2013) and Lanari *et al*. (2014).

The chlorite formation temperature was calculated using the entire database and considering the textural context of each analysis. Several empirical and thermodynamic models were tested (Walsh, 1986; Vidal *et al*., 2002; Inoue *et al*., 2009; Bourdelle *et al*., 2013 and Lanari *et al*., 2014), each one requiring: (1) prior identification of the appropriate solid solution by selecting the relevant end-members; (2) cationic distribution models for each coordination position; and (3) models that calculate the ideal activities of the various components of the solid solution. The obtained results show that the models that best adjust to the chlorite temperatures were those reported in Vidal *et al*. (2001) and Bourdelle *et al*. (2013), framed by the empirical solutions provided by the approach of Jowett (1991).

The calculation expression (T, ºC) used by Jowett (1991) is given by:

$$T = 319 \times \left[Al^{iv} + 0.1\frac{Fe^{2+}}{Fe^{2+}+Mg}\right] - 69 \qquad \text{Equation 4}$$

The thermodynamic approach of Vidal *et al*. (2001) uses the following end-members: $C_1 = clino$; $C_2 = chm$; $C_3 = sud$; $C_4 = am$. The model excludes compositions enriched in Si, ($Si > 3$ apuf), which are common in low-temperature hydrothermal systems. After defining the order by which cationic distributions should be used, the following reaction is considered as reference $2C_1 + 3C_3 = 4C_4 + 7SiO_2 + 4H_2O$, finally calculating:

$$T(°C) = \frac{1}{0.00184 - 1.113\times10^{-4}x + 3.407\times10^{-6}x^2} - 273.15 \qquad \text{Equation 5}$$

$$\text{with } x = 4\log a_{c4} - 2\log a_{c1} - 3\log a_{c3}.$$

The thermodynamic approach of Bourdelle et al. (2013) uses six end-members: $C_1 = Mg\ chl$; $C_2 = Fe\ chl$; $C_3 = Mg\ am$; $C_4 = Fe\ am$; $C_5 = Mg\ sud$ and $C_6 = Fe\ sud$. The approach considers a semi-ordered cationic distribution model and follows the reference reaction $C_1 + 3C_5 = 3C_3 + 7SiO_2 + 4H_2O$, calculating:

$$T(°C) = \frac{9400}{23.40 - x} - 273.15 \qquad \text{Equation 6}$$

$$\text{with } x = 3\log a_{c3} - \log a_{c1} - 3\log a_{c5}.$$

The numeric results obtained are presented in Table IX.9.

Table IX.9 Summary of results obtained for chlorite temperature formation (ºC) using different approaches.

Context	PreDefMtx			PreDefVein			PreDefSulf	PostDefMtx	PostDefMicro fract
Jowett (1991)									
Mean	309			*287*			316	294	*295*
Median	326			274			304	294	295
Stdev	31			*31*			25	12	*7*
Max.	342			338			372	314	306
Min.	219			255			293	278	283
n	48			13			19	10	8
excluded	-			-			-	-	-
Vidal *et al.* (2011)									
Mean	309	396	164	*241*	*402*	*140*	140	162	*145*
Median	383	396	176	*157*	*401*	*153*	136	162	*148*
Stdev	114	14	26	124	20	20	16	14	12
Max.	427	427	194	427	427	159	170	183	163
Min.	107	363	107	110	369	110	123	142	128
n	45	28	17	13	5	8	13	10	5
excluded	4			-			6	-	3
Bourdelle et al. (20013)									
Mean	399			*343*			393	-	-
Median	406			*354*			391	-	-
Stdev	44			36			41	-	-
Max.	462			397			464	-	-
Min.	304			278			296	-	-
n	27			10			10	-	-
excluded	15			-			9	-	-

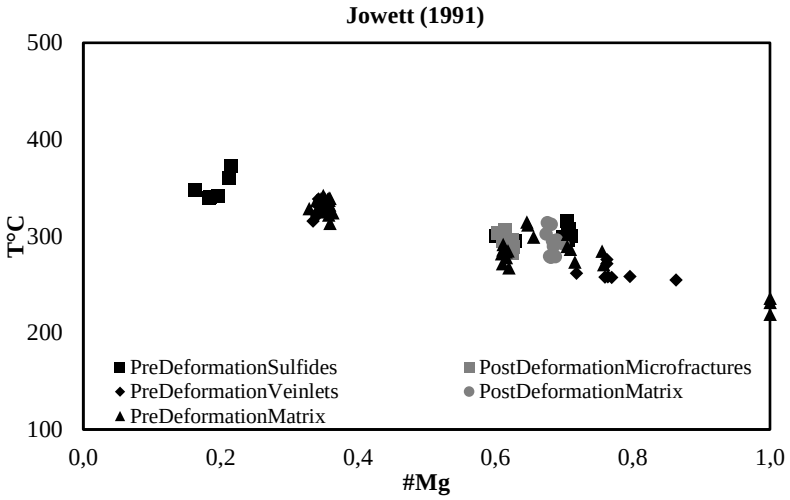

Figure IX.6 Plot of #Mg vs. Temperature for all the chlorite analyses calculated with the empirical model of Jowett (1991).

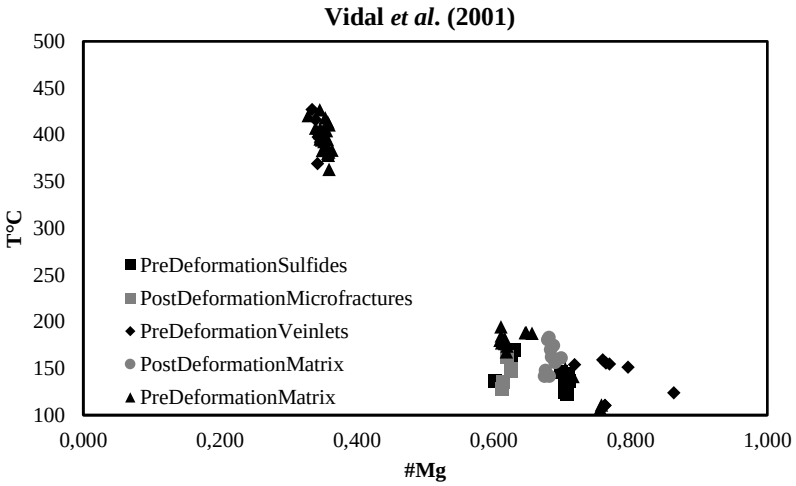

Figure IX.7 Plot of #Mg vs. Temperature for all the chlorite analyses calculated with the thermodynamic model of Vidal et al. (2001).

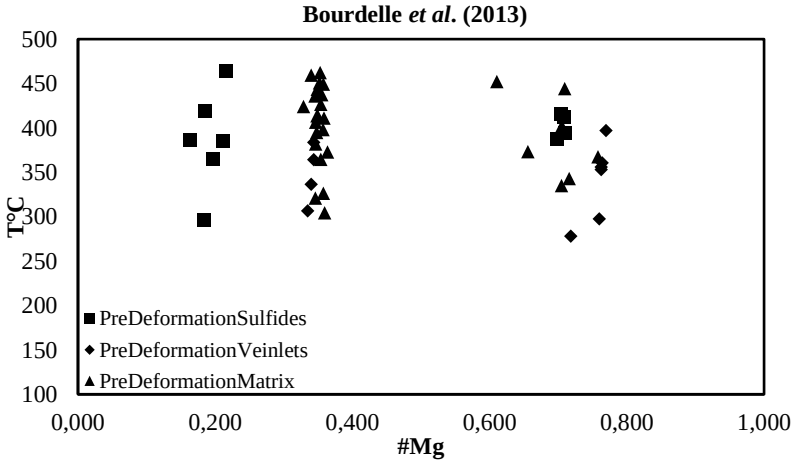

Figure IX.8 Plot of #Mg vs. Temperature for all the chlorite analyses calculated with the thermodynamic model of Bourdelle et al. (2013).

Figure IX.6, Figure IX.7 and Figure IX.8 show that the formation temperature of most chlorites are distributed between 220 and 370°C when the empirical model of Jowett (1991) is applied. The temperature range is wider, extending from 110 to 430°C or from 300 to 460°C, when the thermodynamic approaches of Vidal *et al* (2001) and Bourdelle *et al*., (2013) are used, respectively. Also, and considering the #Mg values, three distinct groups can be considered, as expected and illustrated in Figure IX.4.

Pre-deformation chlorites in rock matrix display temperatures around 330°C, according to the Jowett (1991) empirical model. The thermodynamic model of Bourdelle *et al*. (2013) yields formation temperatures for these chlorites around 410°C, comparing well with results for one of the subgroups when the Vidal *et al*. (2001) model is applied; for the other subgroup, the latter approach indicates much lower temperatures, around 180°C, possibly documenting a late crystallization stage of chlorite or a late compositional readjustment experienced by this phyllosilicate.

Pre-deformation chlorites within veinlets show median temperature values around 270°C and 350°C when the approaches of Jowett (2001) and Bourdelle *et al*. (2013) are used, respectively. Results gathered with the Vidal et al. (2001) approach show once again two subgroups, a high-temperature subgroup, around 400°C, and a lower-temperature subgroup, around 150°C.

Pre-deformation chlorites directly associated with sulfides show median temperatures of 300°C, 135°C and 390°C using the Jowett (1991), Vidal *et al*. (1991) and Bourdelle *et al*., (2013) models, respectively.

Temperature values for post-deformation chlorites are quite similar, regardless of their textural context (within the rock matrix or late-developed micro-fractures), displaying median values around 300°C and 160°C, considering the models of Jowett (1991) and Vidal *et al*. (2001), respectively. The composition of this late-deformation chlorite is not compatible with the solid-solution and/or cationic distribution used in the approach of Bourdelle *et al*. (2013).

In general, the Jowett (1991) empirical model "dilutes" extreme temperature values, indicating a 220-380°C range for pre-deformation chlorites and a 280-310°C range for post-deformation chlorites. Results from the thermodynamic model of Bourdelle *et al*. (2013) point to a higher temperature interval for pre-deformation chlorites, between 280-470°C. The model of Vidal *et al*. (2001) suggests the spatial coexistence of chlorites formed in distinct temperature (and time) ranges: 400-390°C and 180-135°C for pre-deformation chlorites; and 130-180°C for post-deformation chlorites.

IX.1.6. Epidote Group

Epidote is present in felsic and mafic rocks, as an alteration product, sometimes very abundant and frequently along with chlorite, sericite and/or carbonates (respectively).

The general formula for the epidote group is $A_2M_3[T_2O_7][TO_4]O(OH)$ where $A: Ca, Sr, Pb^{2+}, Mn^{2+}, Th, REE^{3+}\ and\ U$, existing two positions $A(A1\ and\ A2)$ structurally different, and $M: Al, Fe^{3+}, Fe^{2+}, Mn^{3+}, Mn^{2+}, Mg, Cr^{3+}\ and\ V^{3+}$ with three octahedral positions $M\ (M1, M2, M3)$ e $T: Si$ (Armbruster *et al*., 2006).

In general, the obtained chemical analyses document a compositional variability determined by the solid solution between epidote and clinozoisite. The plot $(R^{2+}_{-1})^A(R^{3+}_{-1})^M vs.\ (R^{3+}_{+1})^A(R^{2+}_{+1})^M$ (Figure IX.9A) shows that rhyolitic samples are sensitive to $REE + Th$ incorporations, suggesting some deviation

towards the allanite or ferri-allanite compositional fields. For these analyses, the paired cationic replacements involving A and M positions reveal a slight inverse proportionality (Figure IX.9B).

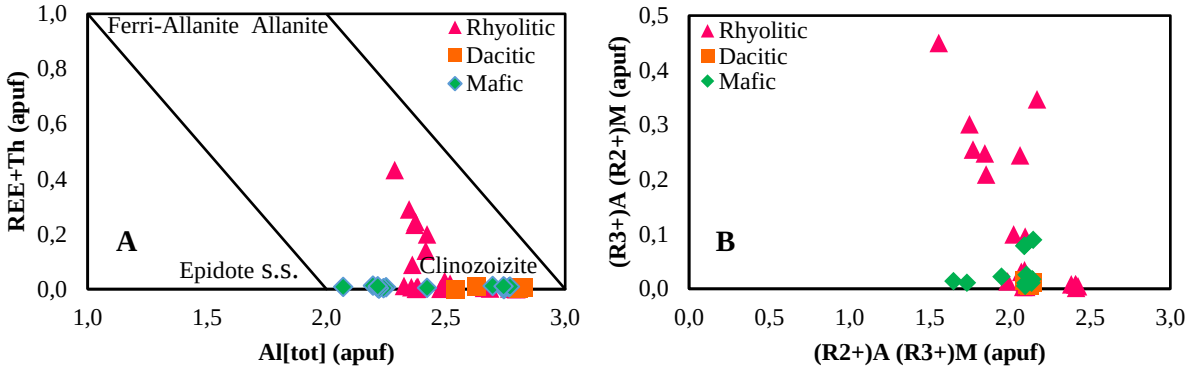

Figure IX.9 A) Plot of Al(T) vs. REE+Th. for epidote analyses. B) Plot of paired substitution vectors for epidote analyses.

Table IX.10 Summary of descriptive statistics for mineral chemistry analyses, in wt%: epidote group (n=55).

	MEAN	*MEDIAN*	*STDEV*	*MAX.*	*MIN.*
Ta_2O_5	0,048	0,000	0,065	0,200	0,000
Nb_2O_5	0,011	0,000	0,016	0,072	0,000
ThO_2	0,007	0,000	0,012	0,049	0,000
ZrO_2	0,015	0,007	0,020	0,094	0,000
TiO_2	0,050	0,032	0,054	0,195	0,000
SiO_2	40,647	37,966	6,580	67,607	30,976
Sm_2O_3	0,060	0,024	0,084	0,351	0,000
Nd_2O_3	0,200	0,020	0,445	1,690	0,000
Pr_2O_3	0,130	0,027	0,205	0,752	0,000
Ce_2O_3	0,398	0,002	1,098	5,347	0,000
La_2O_3	0,290	0,006	0,927	5,905	0,000
Fe_2O_3	7,713	6,503	5,547	34,336	0,000
Mn_2O_3	0,047	0,040	0,045	0,161	0,000
Cr_2O_3	0,011	0,001	0,018	0,084	0,000
V_2O_3	0,061	0,052	0,067	0,368	0,000
Al_2O_3	26,333	25,941	3,498	32,967	17,545
BaO	0,041	0,032	0,046	0,228	0,000
ZnO	0,029	0,000	0,042	0,158	0,000
FeO	0,100	0,000	0,441	2,917	0,000
MnO	0,046	0,024	0,054	0,169	0,000
CaO	19,074	23,276	9,137	27,767	0,025
MgO	0,425	0,024	0,922	4,610	0,000
Na_2O	0,019	0,012	0,038	0,271	0,000

IX.1.7. Zircon group

Zircon is an accessory mineral phase in rhyolitic samples, usually displaying submicroscopic dimensions and coming along with apatite, rutile, titanite, and monazite.

The ideal chemical composition of zircon is $ZrSiO_4$. Compositional deviations are usually due to the incorporation of $Hf^{4+}Zr_{-1}^{4+}$ and $(U^{4+}, Th^{4+}, Ti^{4+}, Sn^{4+})Zr_{-1}^{4+}$. The incorporation of trace elements depends on temperature gradients and for this reason the concentration of these elements can be used to estimate the zircon formation temperature as long as the thermodynamic relations for the cationic substitutions are known. Several authors (*e.g.* Claiborne *et al*., 2006; Ferry and Watson, 2007; Harrison *et al*., 2007) have developed and proposed geothermometer models based on Ti contents. Claiborne *et al*. (2007) proposed an adjustment to the equation developed by Watson *et al*. (2006) (TitaniZ) to calculate the formation temperature, coming to the following equation:

$$T°(C) = \left[{}^{5080}/_{6,01} - log_{0,7\times Ti_{Zrn}}\right] - 273 \qquad \text{Equation 7}$$

where the experimental constants 5080 and 6.01 are affected by uncertainty of ±30 and ±0,03, respectively. The geothermometer TitaniZ can only be applied to systems saturated in rutile (when present) since the same conditions are responsible for high $aZrO_2$ and $aTiO_2$. The saturation in zircon and rutile is strongly dependent on the magma composition and temperature, contrarily to pressure. For this reason, the limitations imposed by the composition of the melt narrow the a_{TiO_2} to values over 0,5 and under 1; Claiborne et al. (2007) considered $a_{TiO_2} = 0{,}7$.

According to the obtained analyses (quite small in number), the zircon average chemical composition is $(Zr_{3.88}Hf_{0.04})SiO_4$.These grains were formed under temperature conditions close to 750-770°C.

Table IX.11 Descriptive statistics of the mineral chemistry analyses, in wt% for zircon group (n=4).

	MEAN	*MEDIAN*	*STDEV*	*MAX.*	*MIN.*
UO₃	0,026	0,013	0,038	0,081	0,000
P₂O₅	0,304	0,303	0,072	0,389	0,221
ThO₂	0,064	0,019	0,105	0,220	0,000
HfO₂	1,135	1,139	0,042	1,183	1,080
ZrO₂	64,283	64,309	0,158	64,439	64,076
TiO₂	0,002	0,000	0,003	0,006	0,000
SiO₂	32,626	32,609	0,116	32,760	32,526
Nd₂O₃	0,014	0,000	0,028	0,056	0,000
Ce₂O₃	0,050	0,050	0,051	0,101	0,000
La₂O₃	0,019	0,012	0,024	0,051	0,000
Fe₂O₃	0,131	0,046	0,184	0,407	0,027
Al₂O₃	0,002	0,000	0,003	0,006	0,000
MnO	0,007	0,007	0,007	0,015	0,000
CaO	0,012	0,009	0,013	0,030	0,000
MgO	0,002	0,000	0,004	0,007	0,000

IX.1.8. Titanite Group

Titanite is another important mineral phase present in all the examined volcanic facies. It occurs in different textural backgrounds, often along with epidote and chlorite, and mostly associated with secondary substitution processes affecting primary mineral phases; individual grains disseminated within the rock matrix were also observed in some samples.

The ideal chemical formula of titanite is $CaTiSiO_4(O, OH, F)$. However, solid solutions exist with aluminous titanites $CaAlFSiO_5$ and Ca can be substituted by a large number of uni- di- and trivalent cations, namely $REE, Y, Mn, Fe^{2+}, Sr, Ba, Mg, Na, K, Li, U, Th$ and Pb; these replacements are balanced by exchanges in Ti or Si contents, for $Al, Fe^{3+}, Nb, Ta, Zr, Sn, V, Cr$ or P, Al, respectively, and often implicate the incorporation of OH, F, Cl instead of O.

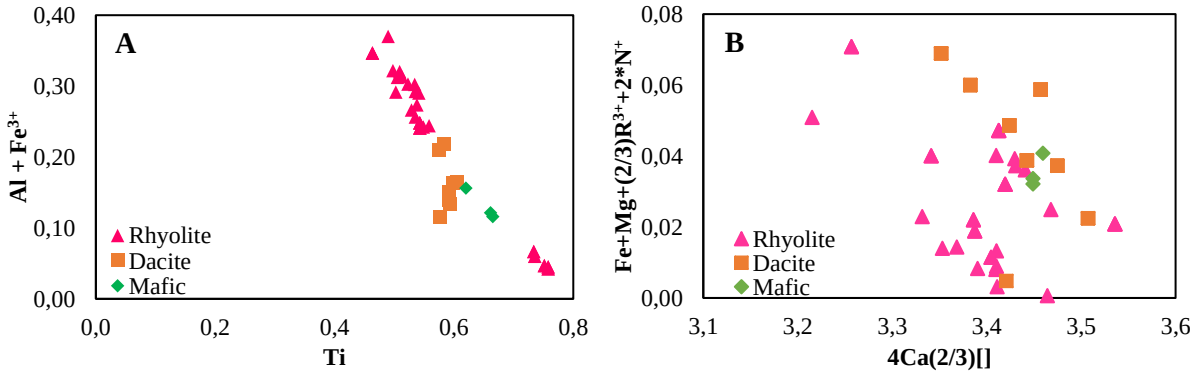

Figure IX.10 A) Plot of *Ti vs. Al+Fe*$^{3+}$ substitution vector. B) Plot of *Fe+Mg+(2/3)R*$^{3+}$*+2*N*$^{+}$ *vs. 4Ca*(2/3)[]* substitution vector.

Table IX.12 Summary of descriptive statistics for mineral chemistry analyses, in wt%: titanite group (n=59).

	MEAN	*MEDIAN*	*STDEV*	*MAX.*	*MIN.*
Ta_2O_5	0,044	0,010	0,068	0,237	0,000
Nb_2O_5	0,090	0,043	0,096	0,278	0,000
ZrO_2	0,121	0,103	0,077	0,274	0,000
VO_2	0,323	0,083	0,387	1,362	0,000
TiO_2	29,318	28,456	4,226	37,984	22,876
SiO_2	30,676	30,578	0,631	32,024	29,536
Sm_2O_3	0,041	0,037	0,050	0,206	0,000
Nd_2O_3	0,070	0,047	0,074	0,258	0,000
Pr_2O_3	0,082	0,008	0,122	0,470	0,000
Ce_2O_3	0,074	0,044	0,079	0,309	0,000
La_2O_3	0,023	0,015	0,023	0,093	0,000
Fe_2O_3	0,294	0,000	0,746	4,482	0,000
Mn_2O_3	0,001	0,000	0,003	0,021	0,000
Cr_2O_3	0,046	0,018	0,064	0,198	0,000
Al_2O_3	5,851	5,182	2,763	10,922	1,352
BaO	0,124	0,121	0,049	0,230	0,022
ZnO	0,009	0,000	0,016	0,069	0,000
FeO	0,973	1,004	0,648	2,222	0,000
MnO	0,009	0,000	0,021	0,105	0,000
CaO	28,757	28,744	0,588	29,868	26,743
MgO	0,178	0,102	0,252	1,152	0,000
K_2O	0,047	0,010	0,076	0,406	0,000
Na_2O	0,033	0,032	0,023	0,073	0,000

Figure IX.10A shows a negative covariation due to the incorporation of Al and Fe^{3+} in the position ideally occupied by Ti, this substitution is balanced by the opening of structural vacancies and the substitution of Ca by *Fe*, *Mg*, N^+, and other R^{3+}cations, showing two different trends (Figure IX.10B).

IX.2. Carbonates

Carbonates are a minor mineral phase in all the examined rock types. Petrographic observations allowed the identification of several generations: (i) early stage veinlets; (ii) pre-deformation and fracture-controlled; (iii) post-deformation and fracture-controlled; (iv) post-deformation veinlets; and (v) very late stage infillings of interstitial spaces. To characterize the compositional variation of carbonates, 120 analyses were made and the results plotted in the conventional ternary diagram $MgCO_3 - CaCO_3 - FeCO_3$. This plot separates three compositionally distinct groups. The calcite group is characterized by a composition very close to the ideal one ($CaCO_3$); the second, documents a solid solution between dolomite and ankerite ($CaMg(CO_3)_2 - Ca(Fe,Mg)(CO_3)_2$; and the siderite ($FeCO_3$) group shows compositional deviations towards the magnesite ($MgCO_3$) end-member.

The calcite group includes 94 quantitative analyses, proving to be very homogeneous in composition, regardless of the rock type or generation. The average composition of this group is $(Ca_{0.971}Mn_{0.003}Fe_{0.003}Mg_{0.002})CO_3$ (Table IX.13).

Table IX.13 Summary of descriptive statistics for mineral chemistry analyses, in wt%: calcite group (n=94).

	MEAN	*MEDIAN*	*STDEV*	*MAX.*	*MIN.*
TiO_2	0,002	0,000	0,006	0,033	0,000
CO_2	44,908	44,192	3,016	66,413	39,844
Ce_2O_3	0,023	0,010	0,027	0,104	0,000
La_2O_3	0,012	0,000	0,019	0,082	0,000
BaO	0,008	0,000	0,017	0,086	0,000
SrO	0,008	0,000	0,023	0,135	0,000
ZnO	0,013	0,000	0,021	0,115	0,000
FeO	0,342	0,182	0,450	3,188	0,002
MnO	0,460	0,223	0,619	3,730	0,013
CaO	54,030	54,161	1,699	57,325	48,941
MgO	0,114	0,062	0,162	1,070	0,000

The siderite group comprises just 5 quantitative analyses gathered in very late stage infillings of interstitial spaces in two rhyolitic lava samples. The average composition of this group is $(Fe_{0.66}Mg_{0.24}Ca_{0.09}Mn_{0.01})CO_3$ (Table IX.14).

Table IX.14 Summary of descriptive statistics for mineral chemistry analyses, in wt%: siderite group (n=5).

	MEAN	*MEDIAN*	*STDEV*	*MAX.*	*MIN.*
CO_2	41,048	41,107	0,096	41,125	40,916
Ce_2O_3	0,018	0,014	0,019	0,041	0,000
La_2O_3	0,019	0,014	0,019	0,043	0,000
BaO	0,008	0,000	0,017	0,038	0,000
SrO	0,004	0,000	0,006	0,011	0,000
ZnO	0,019	0,025	0,014	0,034	0,000
FeO	44,783	44,304	0,813	45,770	44,091
MnO	0,740	0,803	0,113	0,838	0,586
CaO	4,131	4,948	1,465	5,347	2,423
MgO	9,067	8,872	0,598	9,737	8,528
Na2O	0,057	0,063	0,032	0,101	0,018

The dolomite-ankerite group embraces 21 quantitative analyses, all obtained in the sample MdM01#65 but documenting different textural frameworks (within fractures and veinlets, and sealing interstitial spaces) preceding the regional metamorphic peak and deformation. The average composition of this group is $(Ca_{0.54}Mg_{0.22}Fe_{0.19}Mn_{0.01})CO_3$ (Table IX.15).

Table IX.15 Summary of descriptive statistics for mineral chemistry analyses, in wt%: dolomite-ankerite group (n=21).

	MEAN	*MEDIAN*	*STDEV*	*MAX.*	*MIN.*
CO_2	41,048	41,107	0,096	41,125	40,916
Ce_2O_3	0,018	0,014	0,019	0,041	0,000
La_2O_3	0,019	0,014	0,019	0,043	0,000
BaO	0,008	0,000	0,017	0,038	0,000
SrO	0,004	0,000	0,006	0,011	0,000
ZnO	0,019	0,025	0,014	0,034	0,000
FeO	44,783	44,304	0,813	45,770	44,091
MnO	0,740	0,803	0,113	0,838	0,586
CaO	4,131	4,948	1,465	5,347	2,423
MgO	9,067	8,872	0,598	9,737	8,528
Na2O	0,057	0,063	0,032	0,101	0,018

IX.3. Phosphates

This mineral group includes apatite and very rare xenotime. A total of 34 analyses were made in 2 felsic volcanic samples. Apatite frequently occurs along with zircon, titanite and rutile, forming isolated (disseminated) grains; occasionally, it occurs also associated with several alteration products, such as chlorite, epidote and sericite.

The ideal chemical formula of apatite is $Ca_5(PO_4)_3(OH,F,Cl)$. However, the position ideally completed by Ca can be occupied by: (i) other divalent cations with similar radius; (ii) trivalent cations, compensated by the substitution of P by tetravalent cations; or (iii) monovalent cations, compensated by the loss of an anion (F, Cl or OH) and opening of structural vacancies. Figure IX.11A shows that there is some deviation relative to the ideal chemical composition which can be explained by the paired substitutions mentioned above (Figure IX.11B). This deviation is not significant for most of the analyses and the resulting average composition of apatite is $(Ca_{4.98}^{2+}Na_{0.01}^{+})(PO_4)_3OH$.

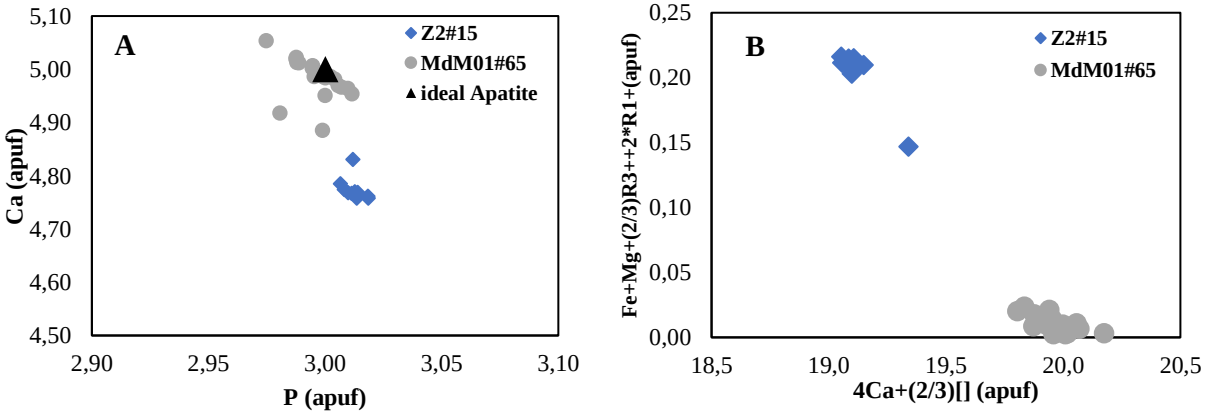

Figure IX.11 A) Plot of P vs Ca considering the ideal chemical formula of apatite. B) Plot of paired Ca substitutions.

Table IX.16 Descriptive statistics of the mineral chemistry analyses, in wt% for the apatite group (n=33).

	MEAN	MEDIAN	STDEV	MAX.	MIN.
P_2O_5	42,503	42,538	0,305	42,885	41,296
Nd_2O_3	0,091	0,088	0,076	0,296	0,000
Ce_2O_3	0,162	0,137	0,143	0,476	0,000
La_2O_3	0,042	0,027	0,044	0,195	0,000
Fe_2O_3	0,027	0,000	0,061	0,340	0,000
Mn_2O_3	0,015	0,000	0,033	0,170	0,000
SrO	0,023	0,000	0,112	0,653	0,000
FeO	0,497	0,018	0,739	1,762	0,000
MnO	0,076	0,016	0,099	0,259	0,000
CaO	55,086	55,808	1,256	56,506	53,174
MgO	0,073	0,005	0,105	0,257	0,000
Na_2O	0,084	0,031	0,119	0,625	0,000

IX.4. Oxides

Oxide phases are quite common in many rock types, as described in Chapter VIII. However, considering just the samples that underwent mineral chemistry studies, rutile *s.l.* is the sole noteworthy oxide in felsic volcanic rocks.

Table IX.17 Descriptive statistics of the mineral chemistry analyses, in wt% for the rutile group (n=16).

	MEAN	*MEDIAN*	*STDEV*	*MAX.*	*MIN.*
WO_3	0,155	0,135	0,154	0,417	0,000
Ta_2O_5	0,048	0,001	0,079	0,282	0,000
Nb_2O_5	0,200	0,173	0,119	0,584	0,089
As_2O_5	0,013	0,008	0,014	0,038	0,000
V_2O_5	0,035	0,017	0,043	0,121	0,000
P_2O_5	0,015	0,000	0,025	0,073	0,000
PbO_2	0,021	0,000	0,029	0,083	0,000
SnO_2	0,042	0,025	0,053	0,167	0,000
ZrO_2	0,097	0,101	0,039	0,196	0,029
MnO_2	0,013	0,000	0,027	0,101	0,000
TiO_2	98,059	97,879	0,814	99,540	96,471
SiO_2	0,308	0,227	0,288	0,837	0,000
Ce_2O_3	0,009	0,000	0,038	0,150	0,000
Ni_2O_3	0,012	0,000	0,015	0,038	0,000
Co_2O_3	0,014	0,005	0,018	0,050	0,000
Fe_2O_3	0,320	0,316	0,128	0,537	0,120
Cr_2O_3	0,077	0,070	0,043	0,198	0,000
Al_2O_3	0,078	0,047	0,090	0,312	0,000
BaO	0,099	0,092	0,053	0,262	0,013
ZnO	0,047	0,022	0,053	0,154	0,000
CuO	0,006	0,000	0,011	0,042	0,000
FeO	0,006	0,000	0,015	0,056	0,000
MnO	0,003	0,000	0,008	0,031	0,000
CaO	0,238	0,146	0,204	0,638	0,010
MgO	0,028	0,002	0,060	0,231	0,000
K_2O	0,022	0,018	0,019	0,060	0,000
Na_2O	0,008	0,008	0,008	0,027	0,000

The ideal composition of rutile is TiO_2. And for the 16 quantitative analyses performed, the average chemical composition is $Ti_{0.99}O_2$.

IX.5. Sulfides

Sulfides are present throughout all rock types, as described in Chapter VIII, usually in trace amounts. A total of 94 analyses were performed, of which 36 correspond to pyrrhotite, 33 to sphalerite, 15 to pyrite, 8 to galena and 2 to chalcopyrite.

The average composition of pyrite, close to the ideal formula (FeS_2), is $Fe_{0.99}Ni_{0.01}S_2$ showing in addition irregular trace amounts of Co and Zn.

Table IX.18 Summary of descriptive statistics for mineral chemistry analyses, in apuf: pyrite group (n=15).

	MEAN	*MEDIAN*	*STDEV*	*MAX.*	*MIN.*
Mo	0,000	0,000	0,000	0,001	0,000
Sn	0,000	0,000	0,000	0,001	0,000
Ge	0,000	0,000	0,000	0,000	0,000
In	0,000	0,000	0,000	0,001	0,000
Pb	0,000	0,000	0,000	0,002	0,000
Cd	0,000	0,000	0,000	0,001	0,000
Zn	0,002	0,000	0,004	0,014	0,000
Cu	0,000	0,000	0,000	0,000	0,000
Ni	0,017	0,008	0,020	0,051	0,000
Co	0,001	0,001	0,001	0,006	0,000
Fe	0,981	0,990	0,018	1,000	0,951
Mn	0,000	0,000	0,000	0,001	0,000
Au	0,000	0,000	0,000	0,000	0,000
Ag	0,000	0,000	0,000	0,001	0,000

Results for pyrrhotite indicate an average chemical composition of $Fe_{0.86}S$ with trace amounts of Ni and Co.

Table IX.19 Summary of descriptive statistics for mineral chemistry analyses, in apuf: pyrrhotite group (n=36).

	MEAN	*MEDIAN*	*STDEV*	*MAX.*	*MIN.*
As	0,000	0,000	0,000	0,001	0,000
Sn	0,000	0,000	0,000	0,000	0,000
Se	0,000	0,000	0,000	0,000	0,000
Ge	0,000	0,000	0,000	0,001	0,000
Sb	0,000	0,000	0,000	0,000	0,000
In	0,000	0,000	0,000	0,001	0,000
Fe	0,871	0,864	0,016	0,897	0,843
Pb	0,000	0,000	0,000	0,001	0,000
Cd	0,000	0,000	0,000	0,000	0,000
Zn	0,000	0,000	0,000	0,001	0,000
Cu	0,000	0,000	0,000	0,000	0,000
Ni	0,002	0,001	0,003	0,009	0,000
Co	0,001	0,001	0,001	0,003	0,000
Mn	0,000	0,000	0,000	0,001	0,000
Au	0,000	0,000	0,000	0,000	0,000
Ag	0,000	0,000	0,000	0,001	0,000

The average composition of sphalerite is $Zn_{0.93}Fe_{0.05}S$, displaying irregular trace amounts of Cd and Mo.

Table IX.20 Summary of descriptive statistics for mineral chemistry analyses, in apuf: sphalerite group (n=33).

	MEAN	*MEDIAN*	*STDEV*	*MAX.*	*MIN.*
Mo	0,001	0,001	0,000	0,001	0,000
As	0,000	0,000	0,000	0,000	0,000
Sn	0,000	0,000	0,000	0,001	0,000
Ge	0,000	0,000	0,000	0,001	0,000
Bi	0,000	0,000	0,000	0,001	0,000
In	0,000	0,000	0,000	0,000	0,000
Pb	0,000	0,000	0,000	0,001	0,000
Cd	0,003	0,002	0,003	0,016	0,000
Zn	0,921	0,934	0,041	0,976	0,851
Cu	0,000	0,000	0,001	0,004	0,000
Ni	0,000	0,000	0,000	0,001	0,000
Co	0,000	0,000	0,000	0,001	0,000
Fe	0,062	0,052	0,040	0,128	0,011
Mn	0,000	0,000	0,000	0,002	0,000
Au	0,000	0,000	0,000	0,000	0,000
Ag	0,000	0,000	0,000	0,001	0,000

Galena presents an average chemical composition of $Pb_{0.99}Fe_{0.01}S$ and irregular trace amounts of Zn, Cu and Ge.

Table IX.21 Summary of descriptive statistics for mineral chemistry analyses, in apuf%: galena group (n=8).

	MEAN	*MEDIAN*	*STDEV*	*MAX.*	*MIN.*
As	0,000	0,000	0,000	0,000	0,000
Sn	0,000	0,000	0,000	0,001	0,000
Ge	0,001	0,001	0,001	0,001	0,000
In	0,000	0,000	0,000	0,001	0,000
Ga	0,001	0,000	0,001	0,002	0,000
Pb	0,991	0,992	0,007	1,003	0,981
Zn	0,004	0,002	0,007	0,021	0,000
Cu	0,001	0,001	0,001	0,003	0,000
Ni	0,000	0,000	0,001	0,002	0,000
Co	0,000	0,000	0,000	0,001	0,000
Fe	0,008	0,006	0,006	0,019	0,000
Mn	0,001	0,000	0,001	0,003	0,000
Ag	0,000	0,000	0,000	0,000	0,000

Quantitative analyses of chalcopyrite were measured only in two different grains due to the common very small grain size. The obtained average composition is $Cu_{0.99}Fe_{1.00}S_2$, showing also trace amounts of Cd, Mo and Co.

Table IX.22 Descriptive statistics of the mineral chemistry analyses, in apuf for the chalcopyrite group (n=2).

	MEAN	*STDEV*	*MAX.*	*MIN.*
Mo	0,001	0,001	0,002	0,001
As	0,000	0,000	0,000	0,000
Bi	0,000	0,000	0,001	0,000
Sb	0,000	0,000	0,000	0,000
In	0,000	0,000	0,001	0,000
Fe	0,996	0,006	1,000	0,992
Pb	0,000	0,000	0,000	0,000
Cd	0,002	0,000	0,002	0,002
Zn	0,000	0,001	0,001	0,000
Co	0,001	0,001	0,002	0,001
Mn	0,000	0,000	0,000	0,000
Cu	0,985	0,007	0,990	0,981

X. PXRF data analysis

Magmatic affinity of volcanic rocks can be assessed using several incompatible trace element ratios, such as *Zr/Y vs*. Al_2O_3/TiO_2. Ideally, these ratios are not modified by many common geological transformations, such as metamorphism or hydrothermal alteration processes. As a general guideline, volcanic rocks displaying *Zr/Y* ratios below 4 have a tholeiitic affinity; whereas ratios ranging from 4 to 7 document transitional affinities, and ratios above 7 indicate calc-alkaline or alkaline affinities.

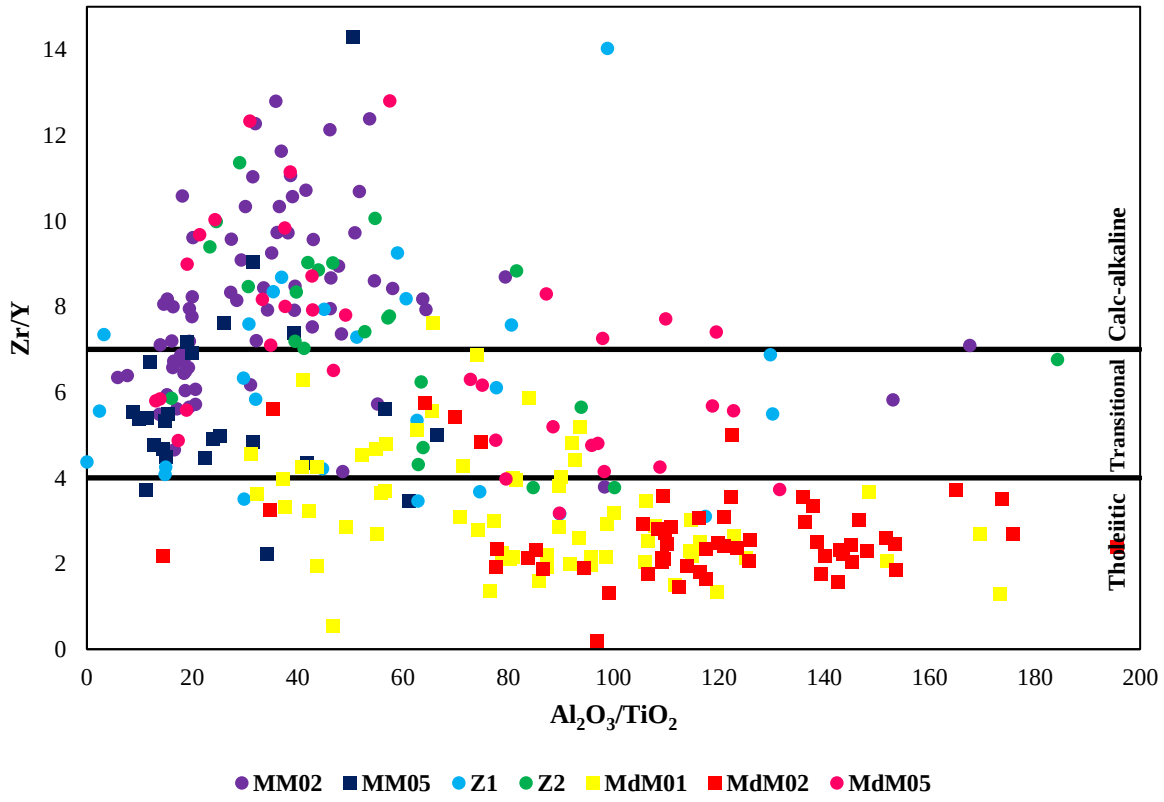

Figure X.1 Plot using immobile element ratios for drill hole samples of Monte das Mesas, discriminating magmatic affinities

Considering the two main (geographic) drill-hole clusters, North (MM05, MdM01, and MdM02) and South (MM02, Z1, Z2, and MdM05), it is clear that they show different magmatic affinities. Volcanic rocks from the northern cluster shows tholeiitic (MdM01 and MdM02) to transitional (MM05) affinities, whereas samples from the southern cluster displays a prevalent calc-alkaline affinity. Note that the *Zr/Y* ratio may be underestimated due to analytical error (overestimation of *Y*), which led to an overall deviation of the plotted samples towards the tholeiitic field. Nevertheless, the error is systematic and for this reason, the main interpretation still valid, two different magmatic affinities are distinguishable.

Immobile element plots are also used to discriminate different rock types in variably modified volcanic sequences since the ratios between various immobile elements remain constant during alteration processes (MacLean and Kranidiotis, 1987; MacLean, 1990; Barrett and MacLean, 1991; Barrett and MacLean, 1999 and Barrett *et al*., 2001).

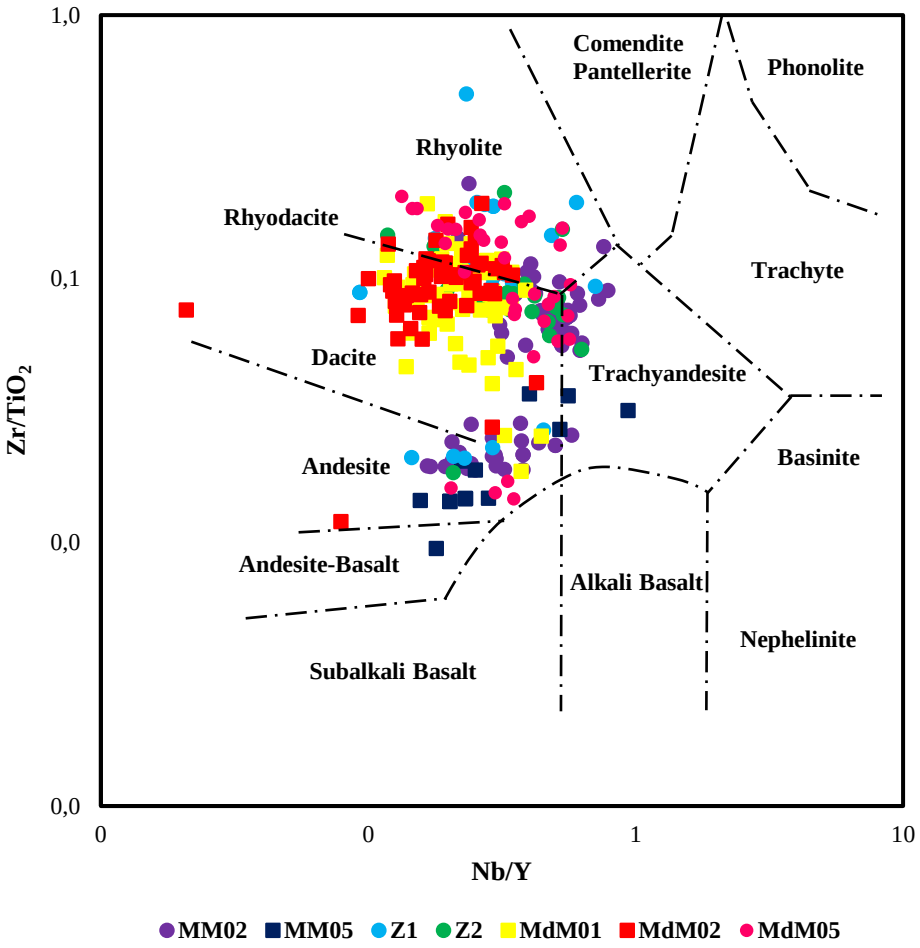

Figure X.2. Plot using immobile elements to discriminate various volcanic rock types (after Winchester and Floyd, 1978).

Most samples along the re-logged drill-holes are in fact compositionally classified as rhyolites and rhyodacites. However, there is a considerable number of samples whose composition spreads in the dacite and andesite fields, particularly along drill-holes MM02 and MM05. These "intermediate" compositions will be referred hereafter as "andesitic-like".

An integrated observation of Figure X.1 and Figure X.2 shows that drill-holes MM02 and MM05 have the strongest transitional affinities and also the more evident "andesitic-like" compositions.

The volcanic rocks that host massive sulfide deposits record mineralogical and compositional modifications due to different, and superimposed, alteration stages; however, not all of them are related to hydrothermal ore-forming process. To geochemically discriminate alteration stages with metallogenetic or regional significance, Large *et al*. (2001) proposed an alteration box plot that uses two indexes: the AI (Ishikawa Alteration Index) and the CCPI (chlorite-carbonate-pyrite index).

$$AI = \frac{100(K_2O+MgO)}{(K_2O+MgO+Na_2O+CaO)} \qquad \text{Equation 8}$$

The AI index (equation 8) was proposed by Ishikawa *et al*. (1976) to estimate the intensity of sericite and chlorite alteration recorded by volcanic rocks proximal to Kuroko deposits. The key mineral

reactions involve the breakdown of sodic plagioclase and volcanic glass and their replacement by sericite and chlorite. However, there are two major limitations regarding the use of this index, as follows: (1) it does not consider the effects related to carbonate alteration, which can be significant in some massive sulfide ore systems, leading to a decrease in the AI values;, and (2) used alone, the index does not allow the separation of chlorite- from sericite-rich alteration, the two common and major haloes of alteration associated with massive sulfide ores (Large *et al*., 2001).

$$CCPI = \frac{100(MgO+FeO)}{(MgO+(FeO+Fe_2O_3)+Na_2O+K_2O} \qquad \text{Equation 9}$$

The CCPI index (equation 9) has been designed to measure the increase in *MgO* and *FeO* related to the *Mg-Fe* chlorite development, which commonly replaces albite, K-feldspar, or sericite in hydrothermally altered volcanic rocks, leading to falls in Na_2O and K_2O abundances. Plus, it is also affected positively by *Mg-Fe* carbonate alteration (dolomite, ankerite, or siderite) as well as pyrite, magnetite or hematite enrichments, since all these mineral phases incorporate *Fe*, *Mg* or both elements, typically developed in the inner alteration zones. One important limitation of the CCPI index is its sensitivity to magmatic fractionation processes and primary compositional variations in the volcanic rocks. This contrasts with the AI indez, which shows no significant trend across the same compositional range from rhyolite to basalt (Large *et al*., 2001).

The combination of the Ishikawa AI index (plotted in the horizontal axis) and the CCPI index (plotted in the vertical axis), proposed by Large *et al*. (2001), show that the least altered volcanic rocks plot toward the center of the diagram, and hydrothermally altered volcanic rocks plot in different fields depending on the prevailing secondary mineral assemblage. The mineral end-members (albite, K feldspar, sericite, chlorite, pyrite, dolomite, ankerite, and epidote) plot along the boundaries of the box in the marked positions.

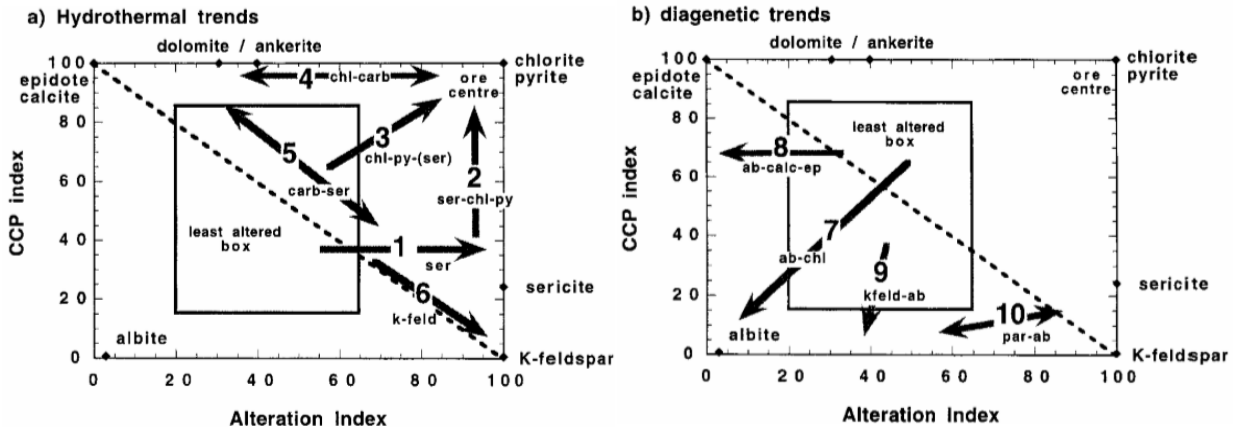

Figure X.3 a) Compositional trends for hydrothermal alteration (left) b) Compositional trends for diagenetic alteration (right) in the alteration box plot. The arrows indicate the common trends depending on the secondary mineral assemblage and intensity of alteration (in Large *et al*., 2001).

These alteration indexes are useful in exploration surveys as they allow distinguish compositional trends related to regional alteration effects (the so-called seafloor metasomatism), exhalative hydrothermal

activity without associated mineralization, and ore-forming hydrothermal systems. This has been successfully applied by other authors in different IPB areas (*e.g.* Codeço, 2015). Unfortunately, due to the nature of the whole-rock geochemical data analyses available in this study (PXRF), it is not possible to evaluate these alteration indices, because no quantitative measurements exist for some elements (*e.g. Na*) or no reliable data exist for other measured elements (*e.g. Mg*). Nonetheless, other weaknesses are known, especially important for the Monte das Mesas area, since the volcanic rock types are predominantly clastic (even though frequently clast supported), therefore affected by sedimentary transport processes. Volcanic-derived sediments should be plotted with extreme caution in these diagrams as mixtures with sliciclastic components may lead to chemical changes (*e.g.* loss of alkalis), causing increases in both the AI and the CCPI that are unrelated to hydrothermal alteration.

Host rock samples from the Aljustrel (Feitais) volcanic sequence and overlying shales were plotted and the main rock types defined by their trends: rhyolites A, B, C, X and QF porphyry (Dawson and Caessa, 2003; Barrett, 2008; Barrett, 2009). The various groups are generally well defined, although each show a certain degree of scattering. No data for mafic volcanic rocks of Aljustrel were published to date, although mafic dykes with chilled margins occur in some drillholes (Barrett, 2009). The present chapter attempt to characterize and frame the volcanic sequence at Monte das Mesas through its geochemical signature and comparison to the Aljustrel chemostratigraphy.

Regarding the magmatic affinity of volcanic rocks assessed using incompatible trace element ratios (*e.g. Zr/Y vs. Al_2O_3/TiO_2*), the Aljustrel (Feitais) host rocks reflect different affinities, proving their different rock types signatures. Rhyolites A and C generally have lower Zr/Y than rhyolites B and X. This suggests that these two rhyolite "pairs" were derived from different magma types, tholeiitic-transitional and transitional(-calc-alkaline), respectively. Zr/Y ratios for the QF porphyry are higher and its *Al_2O_3/TiO_2* ratios are considerably lower than the previous rock types, this suggests that it represents a different calc-alkaline magma type (Barrett *et al*.,2008).

Conceptually, in immobile element plots, altered rocks from an originally homogeneous volcanic unit will plot along linear arrays. These linear arrays (also known as alteration lines) are caused by net mass loss/gain of mobile elements during alteration; however, distinct precursor compositions generate different slope alteration lines.

In plots of one immobile ratio against another, involving elements such as Al, Ti, and Zr, the effects of alteration are essentially removed; in plot Zr/TiO_2 *versus* Al_2O_33/TiO_2 the relative position of a given rhyolite along the Y-axis simply reflects the slop of its alteration line in plot (TiO_2 *versus* Zr, figure XI.1.1.). The small spread of points within each rhyolite field can be due to minor magmatic fractionation effects or, in case of volcaniclastic rocks, to minor intermixing of other clast types.

Although a given rhyolite type can overlap another type in terms of one immobile element ratio, the other ratios do not simultaneously overlap. For this reason, rhyolite type identification is based on several ratios. In this study Al_2O_3 *versus* TiO_2, TiO_2 *versus* Zr, Al_2O_3 *versus* Zr (not shown), Zr/Al_2O_3 *versus* Al_2O_3/TiO_2, Zr/TiO_2 *versus* Al_2O_3/TiO_2 and Zr/Nb *versus* Al_2O_3/TiO_2 (not shown) were used to constrain, identify and relate the several geochemical different types of felsic rocks present in Monte das Mesas with Aljustrels main rock types.

Along drill-hole MM02, Figure X.1.1 and Figure X.1.2, two major compositionally different rock types are considered: (i) a subgroup with an intermediate composition between qfR and rhyolite B; and (ii) a subgroup characterized by very low Zr/TiO_2 *versus* Al_2O_3/TiO_2, reflecting "andesitic-like" compositions. Two unique samples were framed in the Rhyolite C and A compositional fields.

From Figure X.2.1 and Figure X.2.2, four subgroups can be considered to existe along drill-hole Z1: (i) a subgroup chemically framed within type C rhyolites; (ii) a subgroup with higher Zr/TiO_2 ratios, closer to the rhyolite type A compositional field; (iii) a subgroup framed from qf and B type rhyolites; and (iv) two (anomalous?) samples showing significant lower Zr/TiO2 ratios.

Along drill-hole Z2, five distinct compositional signatures can be considered (Figure X.3.1 and Figure X.3.2): (i) framed by rhyolite type A; (ii) one sample near rhyolite C field; (iii) another compatible with rhyolite B signature; (iv) close to qfR field, however with higher Zr contents; and (v) one sample with lower ratios consistent with a mafic composition (present along the Z2 drill hole).

Figure X.4.1 and Figure X.4.2 display three distinct compositional subgroups presente along drill-hole MdM05: (i) a well-represented subgroup whose spread is similar to rhyolite A; (ii) another well-represented subgroup with an intermediate signature from type qfR and B rhyolites; and (iii) a smaller subgroup with lower ratios consistent with mafic compositions, from mafic intrusions present along the MdM05 drill-hole.

Two major subgroups were considered along drillhole MM05 (Figure X.5.1 and Figure X.5.2): (i) close to the spread that characterize B type shyolites, and (ii) with lower ratios, consistent with intrusive mafic rocks present along the drill-hole, but also with more intermediate signatures related to “andesitic-like” compositions.

Along drill-hole MdM01 the chemical signature is “diffuse”, spreading between the compositional fields proposed for qfR, B, and C type rhyolites (Figure X.6.1 and Figure X.6.2).

Felsic volcanic rocks in drill-hole MdM02 show no chemical relationship with any rhyolite type classified by Barrett (2009), displaying much higher Al_2O_3/TiO_2 ratios (Figure X.7.1 and Figure X.7.2).

X.1. MM02

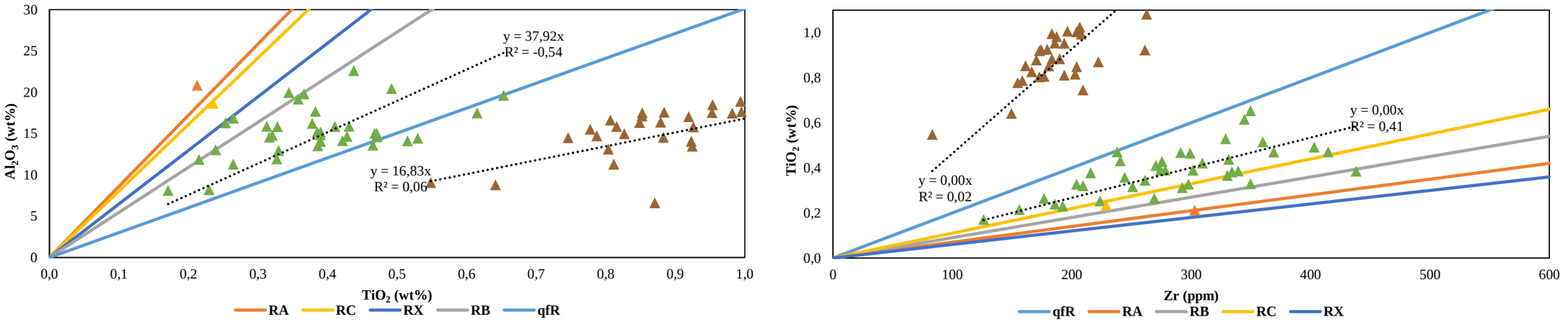

Figure X.1.1 Immobile element plots for MM02 drill-hole samples. The colored full lines represent the tendency line for each rhyolite type present in Aljustrel (Feitais) host rocks, sampled along drill-holes and nearby outcrops. Triangles (▲) represent samples from Monte das Mesas.

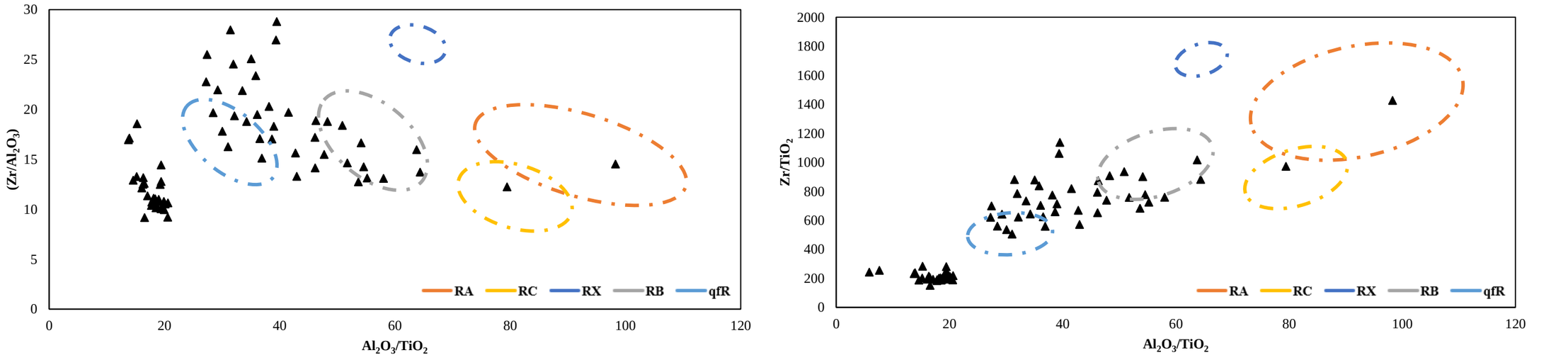

Figure X.1.2 Plot using immobile element ratio on each axis for MM02 drill hole. The colored areas represent the spread for each rhyolite type present in Aljustrel (Feitais) host rocks, sampled along drill-holes and nearby outcrops. Triangles (▲) represent samples from Monte das Mesas.

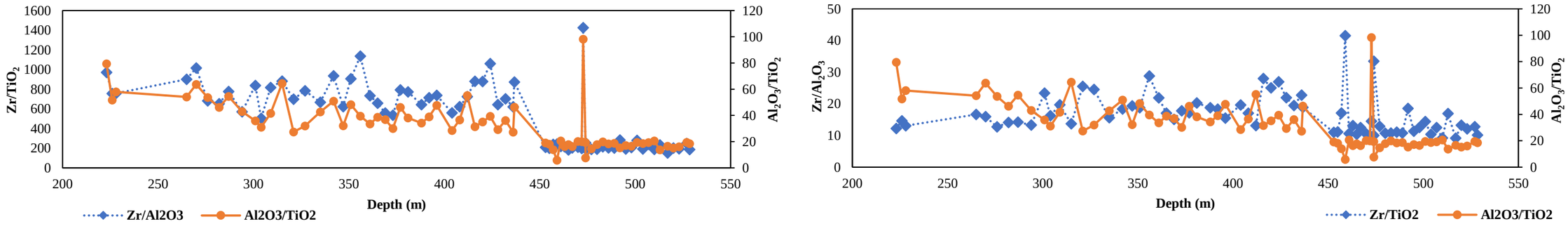

Figure X.1.3 Down-hole chemostratigraphic units for drill hole MM02. Despite of variations in facies and degree of alteration, the main felsic rock types can be identified

X.2. Z1

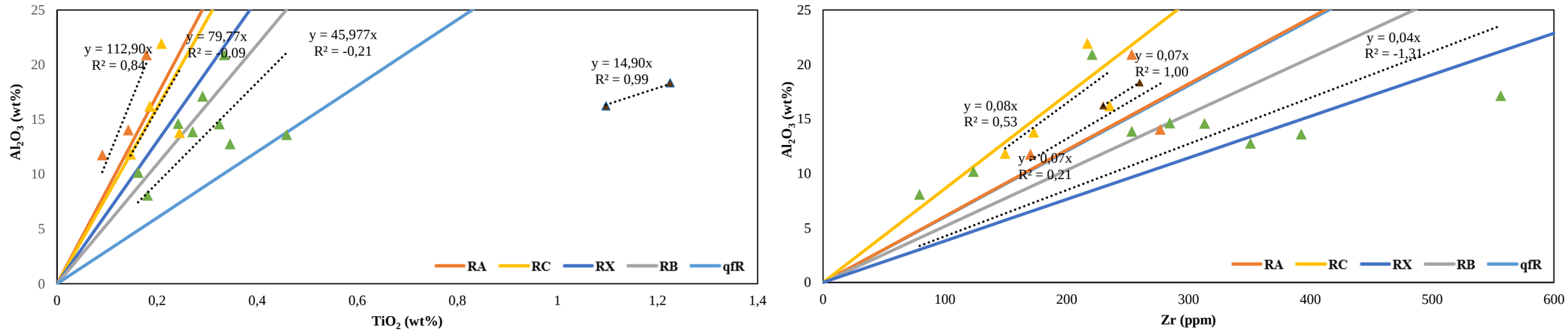

Figure X.2.1 Immobile element plots for Z1 drill-hole samples. The colored full lines represent the tendency line for each rhyolite type present in Aljustrel (Feitais) host rocks, sampled along drill-holes and nearby outcrops. Triangles (▲) represent samples from Monte das Mesas.

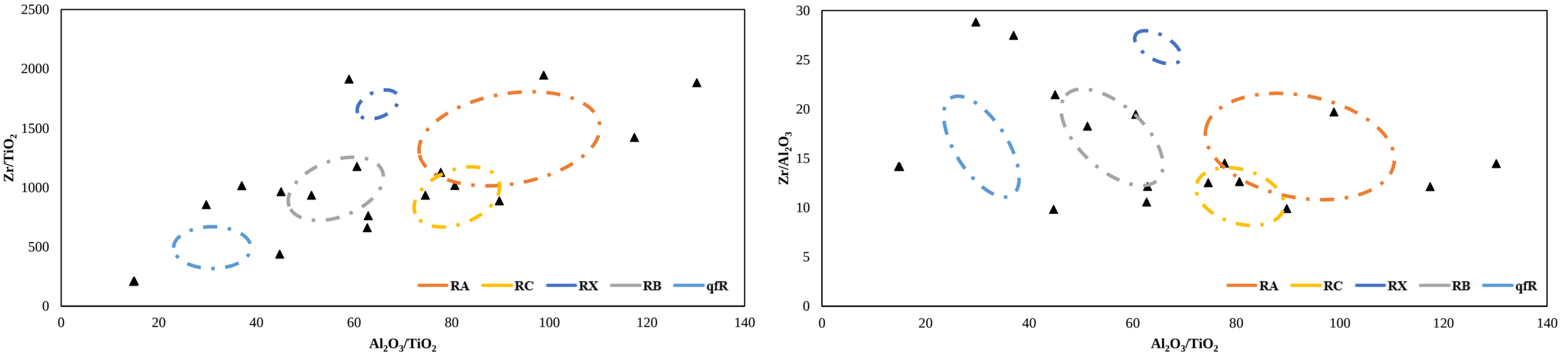

Figure X.2.2 Plot using immobile element ratio on each axis for Z1 drill hole. The colored areas represent the spread for each rhyolite type present in Aljustrel (Feitais) host rocks, sampled along drill-holes and nearby outcrops. Triangles (▲) represent samples from Monte das Mesas.

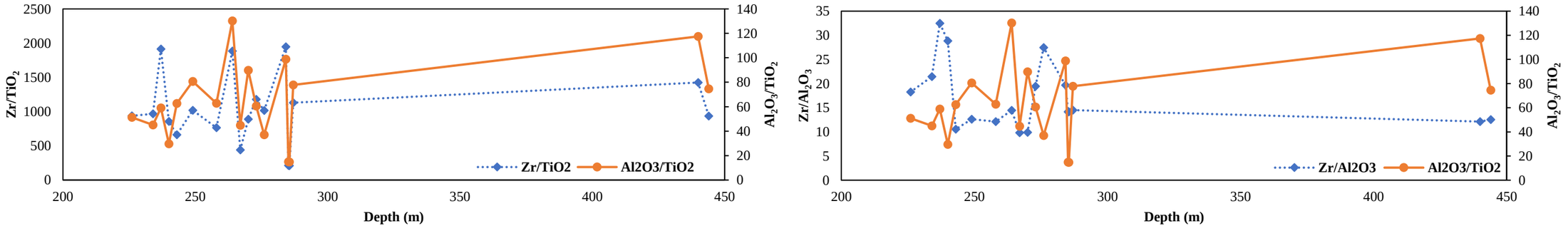

Figure X.2.3 Down-hole chemostratigraphic units for drill hole Z1. Despite of variations in facies and degree of alteration, the main felsic rock types can be identified

X.3. Z2

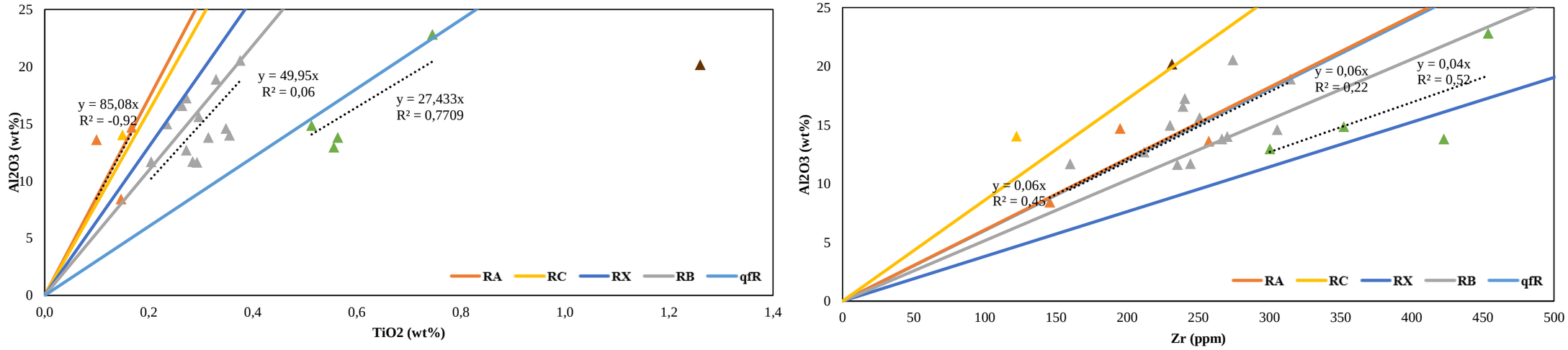

Figure X.3.1 Immobile element plots for Z2 drill-hole samples. The colored full lines represent the tendency line for each rhyolite type present in Aljustrel (Feitais) host rocks, sampled along drill-holes and nearby outcrops. Triangles (▲) represent samples from Monte das Mesas.

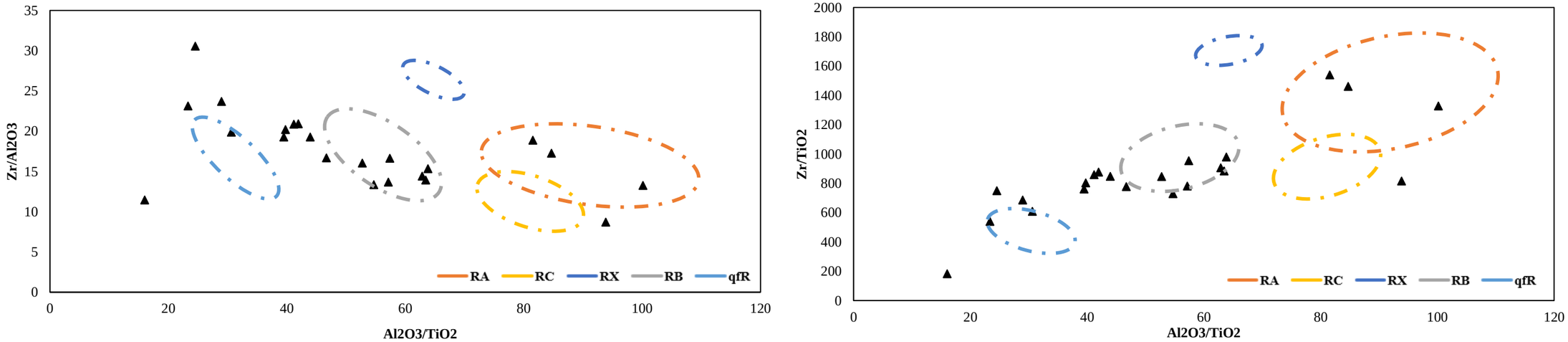

Figure X.3.2 Plot using immobile element ratio on each axis for Z2 drill hole. The colored areas represent the spread for each rhyolite type present in Aljustrel (Feitais) host rocks, sampled along drill-holes and nearby outcrops. Triangles (▲) represent samples from Monte das Mesas.

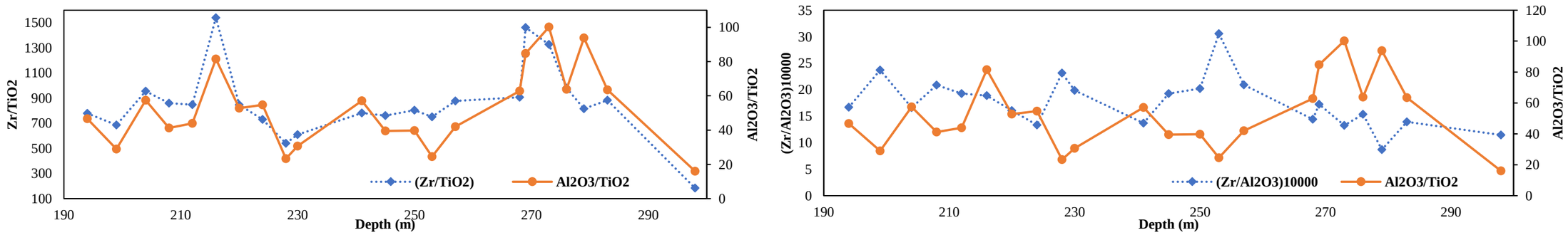

Figure X.3.3 Down-hole chemostratigraphic units for drill hole Z2. Despite of variations in facies and degree of alteration, the main felsic rock types can be identified

X.4.MdM05

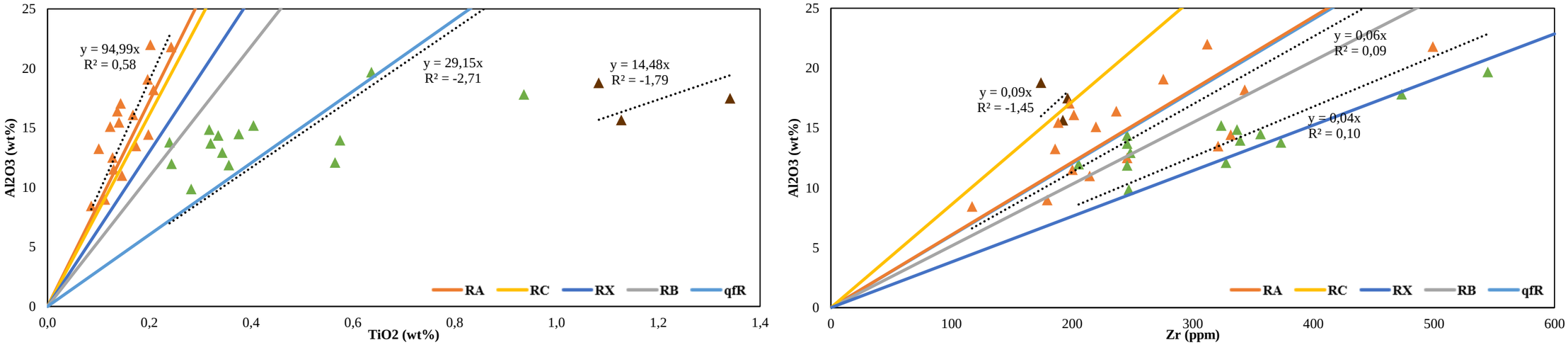

Figure X.4.1 Immobile element plots for MdM05 drill-hole samples. The colored full lines represent the tendency line for each rhyolite type present in Aljustrel (Feitais) host rocks, sampled along drill-holes and nearby outcrops. Triangles (▲) represent samples from Monte das Mesas.

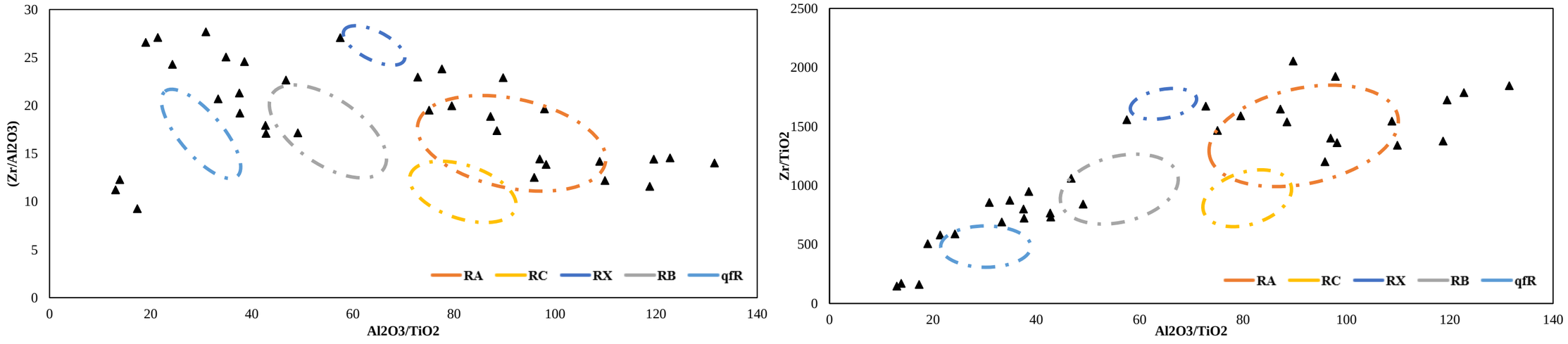

Figure X.4.2 Plot using immobile element ratio on each axis for MdM05 drill hole. The colored areas represent the spread for each rhyolite type present in Aljustrel (Feitais) host rocks, sampled along drill-holes and nearby outcrops. Triangles (▲) represent samples from Monte das Mesas.

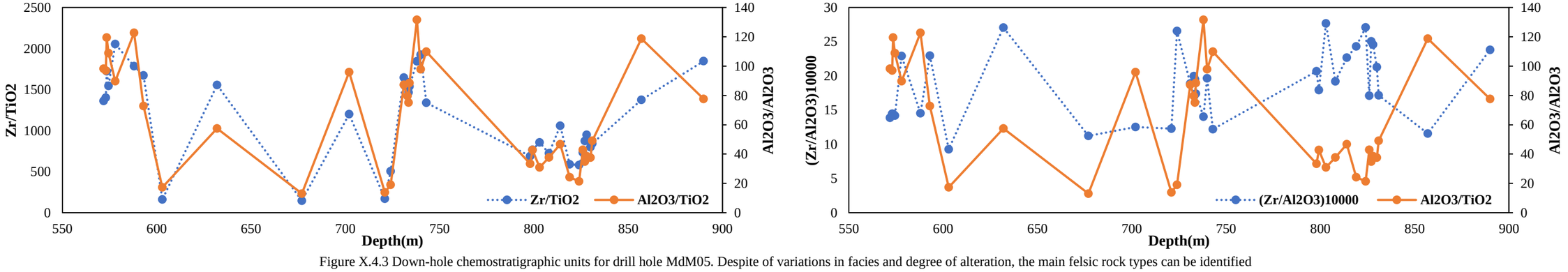

Figure X.4.3 Down-hole chemostratigraphic units for drill hole MdM05. Despite of variations in facies and degree of alteration, the main felsic rock types can be identified

X.5.MM05

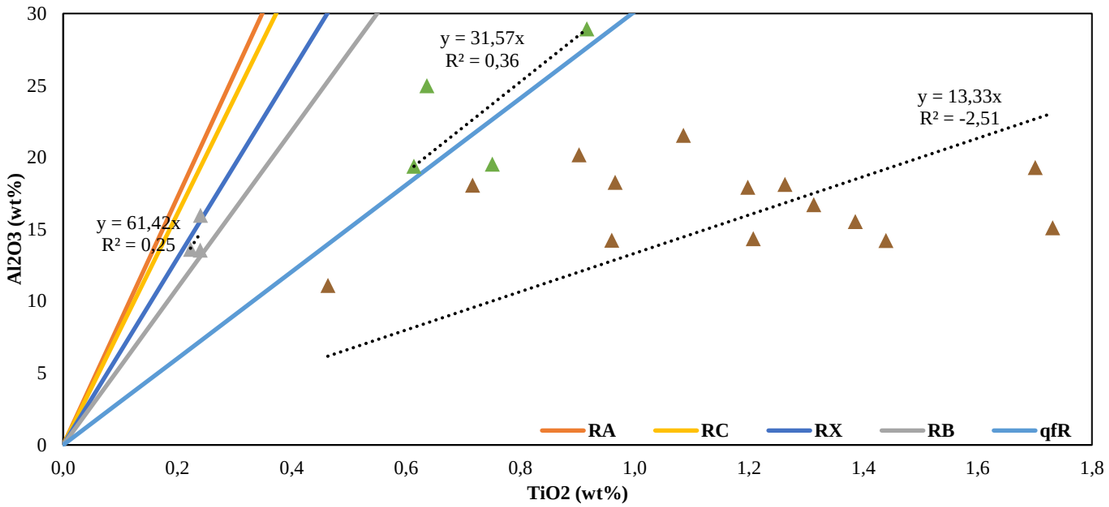

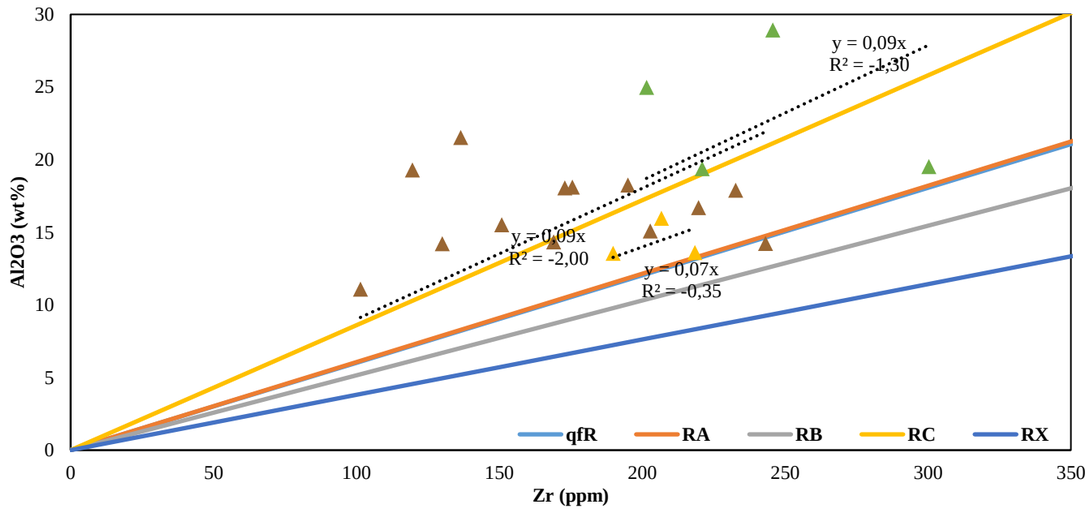

Figure X.5.1 Immobile element plots for MM05 drill-hole samples. The colored full lines represent the tendency line for each rhyolite type present in Aljustrel (Feitais) host rocks, sampled along drill-holes and nearby outcrops. Triangles (▲) represent samples from Monte das Mesas.

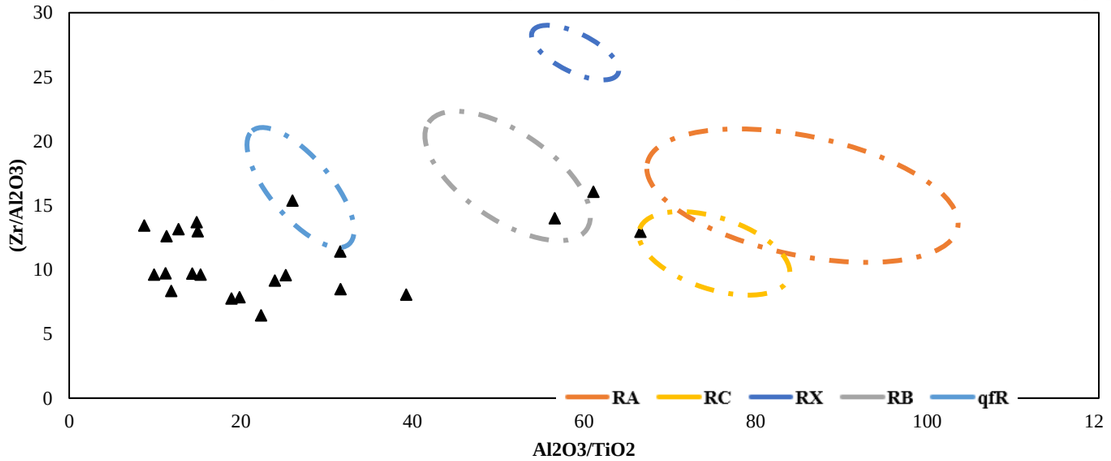

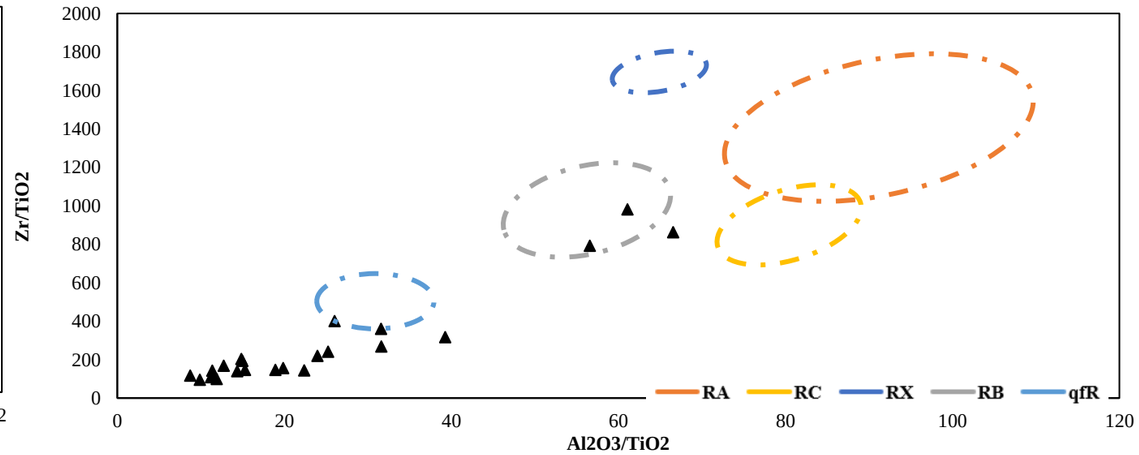

Figure X.5.2 Plot using immobile element ratio on each axis for MM05 drill hole. The colored areas represent the spread for each rhyolite type present in Aljustrel (Feitais) host rocks, sampled along drill-holes and nearby outcrops. Triangles (▲) represent samples from Monte das Mesas.

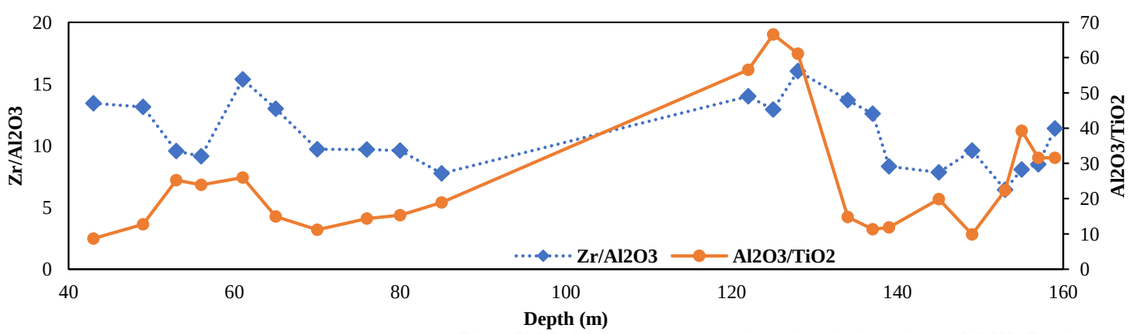

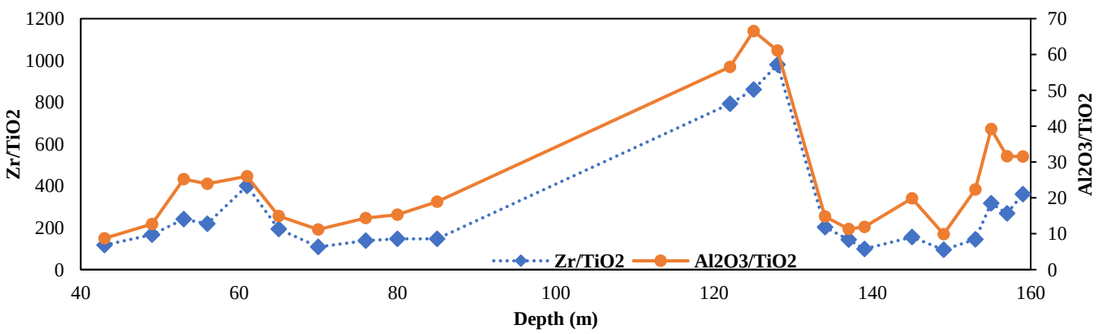

Figure X.5.3 Down-hole chemostratigraphic units for drill hole MM05. Despite of variations in facies and degree of alteration, the main felsic rock types can be identified

X.6.MdM01

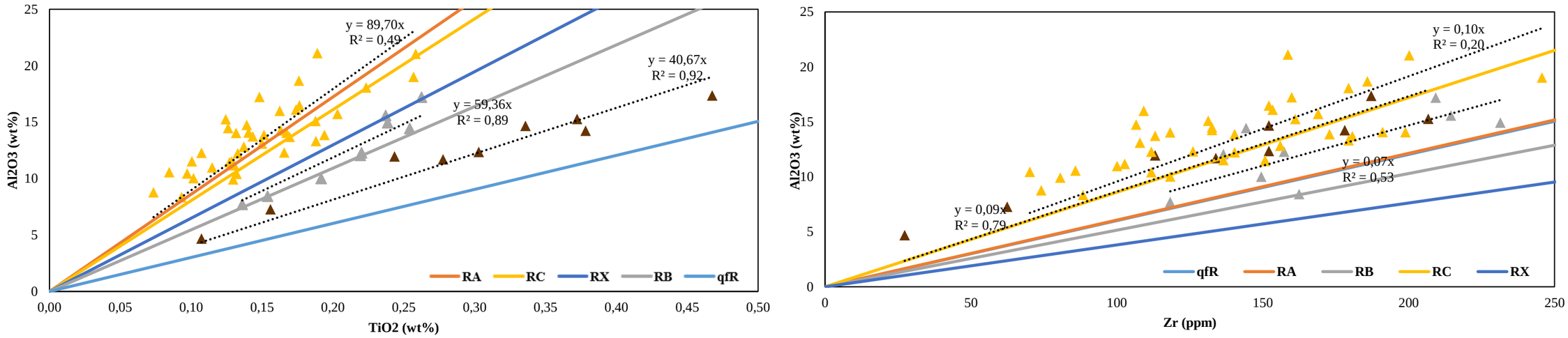

Figure X.6.1 Immobile element plots for MdM01 drill-hole samples. The colored full lines represent the tendency line for each rhyolite type present in Aljustrel (Feitais) host rocks, sampled along drill-holes and nearby outcrops. Triangles (▲) represent samples from Monte das Mesas.

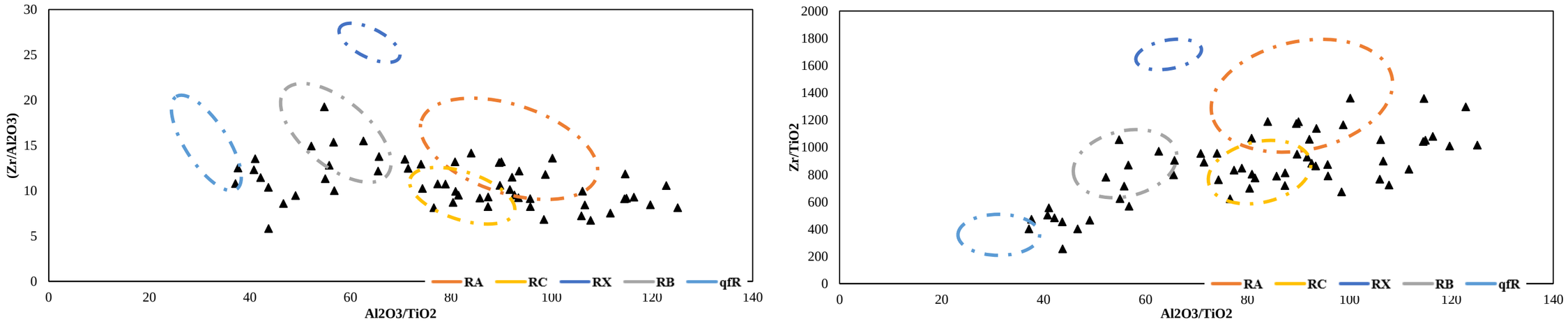

Figure X.6.2 Plot using immobile element ratio on each axis for MdM01 drill hole. The colored areas represent the spread for each rhyolite type present in Aljustrel (Feitais) host rocks, sampled along drill-holes and nearby outcrops. Triangles (▲) represent samples from Monte das Mesas.

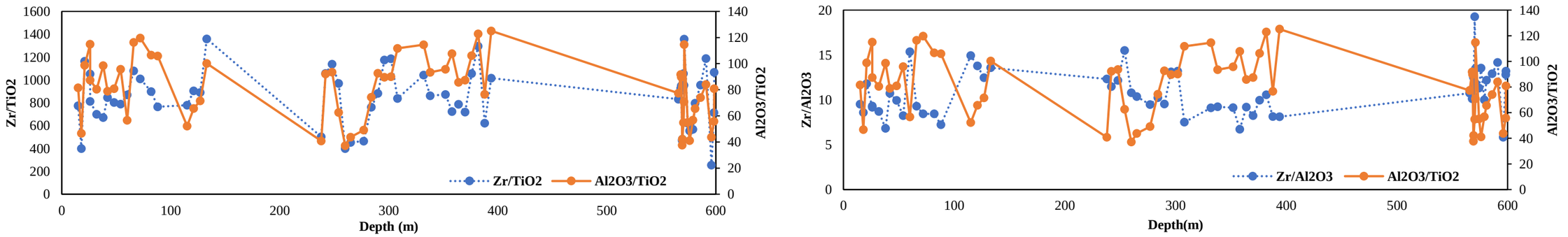

Figure X.6.3 Down-hole chemostratigraphic units for drill hole MdM01. Despite of variations in facies and degree of alteration, the main felsic rock types can be identified

X.7.MdM02

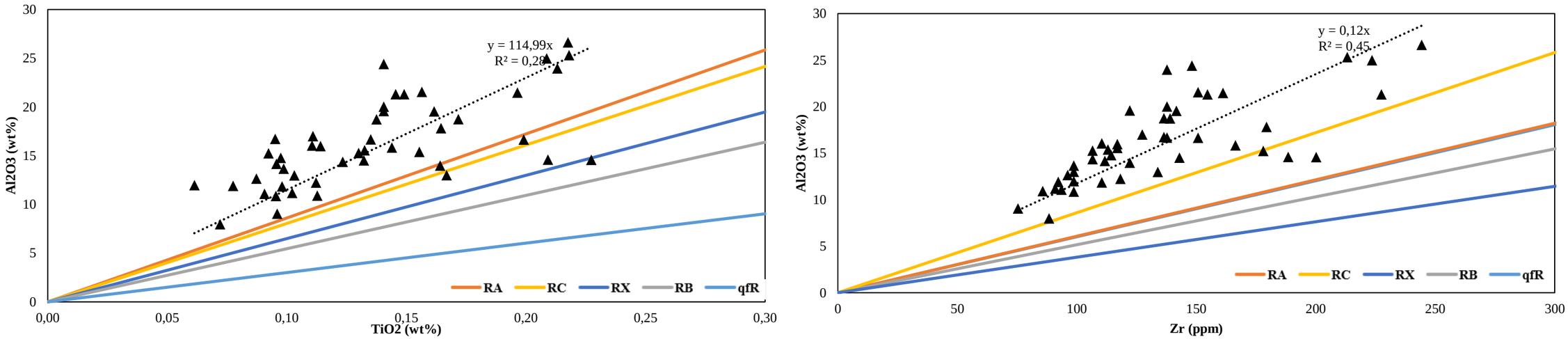

Figure X.7.1 Immobile element plots for MdM02 drill-hole samples. The colored full lines represent the tendency line for each rhyolite type present in Aljustrel (Feitais) host rocks, sampled along drill-holes and nearby outcrops. Triangles (▲) represent samples from Monte das Mesas.

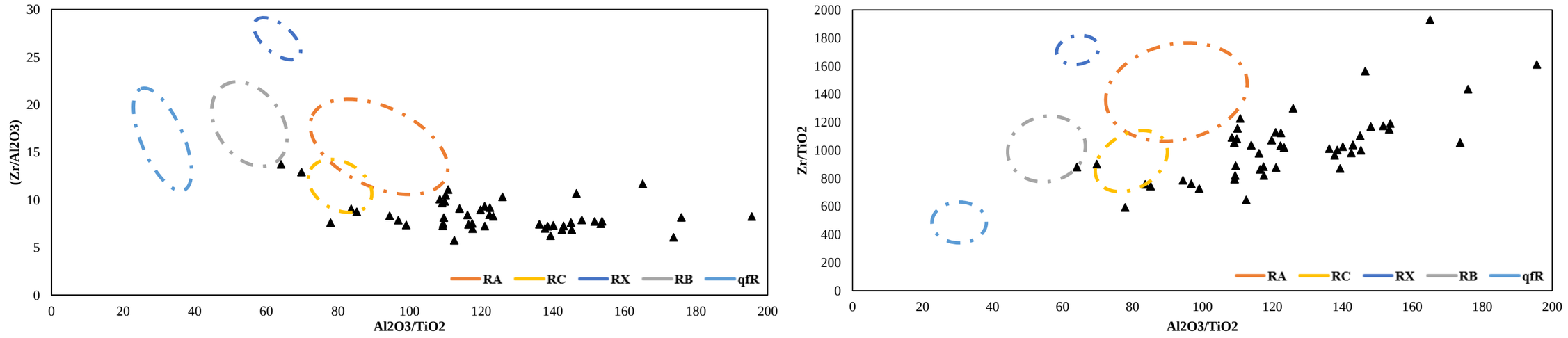

Figure X.7.2 Plot using immobile element ratio on each axis for MdM02 drill hole. The colored areas represent the spread for each rhyolite type present in Aljustrel (Feitais) host rocks, sampled along drill-holes and nearby outcrops. Triangles (▲) represent samples from Monte das Mesas.

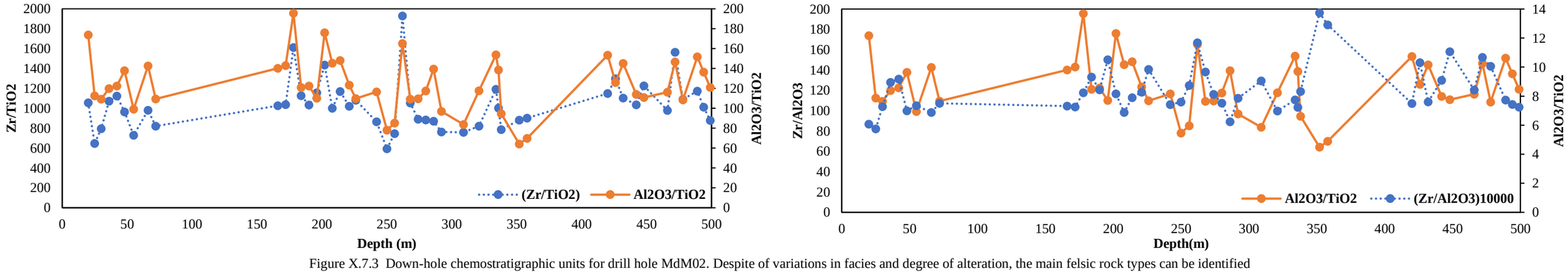

Figure X.7.3 Down-hole chemostratigraphic units for drill hole MdM02. Despite of variations in facies and degree of alteration, the main felsic rock types can be identified

XI. Discussion

In this chapter, the data and information presented in previous sections are interpreted and fully integrated, guiding the discussion towards the answers that driven the work done at the Monte das Mesas prospect.

The volcanic sequence recognized at Monte das Mesas is composed of micro-porphyritic, rhyolitic to dacitic, lavas and compositionally similar volcaniclastic rocks, the latter prevailing over the former and often intercalated with abundant grey-black (occasionally green or purple) metapelites incorporating components of (possible) volcanogenic origin. Intermediate and mafic lava flows are subordinate. Mafic sills/dykes are frequent throughout all the area. *Andesite-like* facies are also identified, comprising primary mineral assemblages *e.g.* pyroxene, amphibole and plagioclase relics along with minor quartz.

Felsic lavas observed at Monte das Mesas are generally composed of micro-phenocrysts of quartz (usually showing reaction golfs) and feldspar *s.l.* (most often revealing effects of significant hydrolysis). The relative abundance of these three mineral phases (quartz, plagioclase and k-feldpar, present not only as micro-phenocrysts but also forming the rock matrix) led to the discrimination between rhyolitic, rhyodacitic and dacitic lavas. The volcanic sequence drilled at the northern part of the Monte das Mesas area proved to be more rhyolitic than the one crossed by the group of drill-holes forming the southern cluster, where rhyodacitic to dacitic terms tend to prevail. The groundmass of these felsic lavas is mostly composed of quartz, feldspar *s.l.* and phyllosilicates (sericite > chlorite). The amount of secondary epidote and titanite is noteworthy in several samples along with minor (vestigial) apatite, zircon, sulfides (pyrite, pyrrhotite, galena, sphalerite and chalcopyrite) and oxides. The intermediate and mafic facies also include clinopyroxene (augite) relics, usually involved/replaced by a late-developed calcic amphibole (actinolite) and, afterwards, by fine-grained aggregates of chlorite and epidote.

Coherent lavas show quite often evidence of *in situ* fracturing and brecciation. The fractures acted as channels, increasing the rock permeability and enhancing fluid circulation. This led to pervasive alteration, precipitating microcrystalline quartz, sericite, chlorite and minor carbonates, frequently originating *breccia-like* textures. All the samples, independently of the cluster of drill-holes, show signs of this alteration, suggesting the development of conditions appropriate to sustain a widespread regional-scale metasomatic event, as documented in many studies performed in other IPB segments (Nehlig *et al*., 1998; Relvas, 2000; Relvas *et al*., 2001 Relvas *et al*., 2006; Rosa, 2007). This early alteration, preceding the ore-forming processes, is marked by the deposition of sericite, locally accompanied by chlorite.

To better constrain, understand and frame the Monte das Mesas VSC sequence, PXRF data analyses were used and compared to the preexisting published data regarding the Aljustrel VSC sequence.

The information obtained based on the concentrations of immobile elements, namely Zr/TiO_2 and *Nb/Y*, documented in Figure X.2, (compositionally) classify most felsic rocks between rhyolitic to dacitic compositions (*i.e.* rhyodacitic) and, minor intermediate rocks. However, Figure X.1, show two very different affinities, regarding the genesis of the magmas that gave rise to the various felsic facies observed at Monte das Mesas. The VSC succession observed in the northern sector (drill-holes MM05, MdM01 and MdM02) is related to tholeiitic magmas whereas the VSC succession at the southern sector (drill-holes MM02, Z1, Z2 and MdM05) shows a calc-alkaline magmatic affinity consistent with many studies on magmatism in the IPB (e.g., Munhá, 1983; Thiéblemont *et al*., 1998; Mitjavilla *et al*., 1997; Carvalho *et al*., 1999). Drill-holes MM02 and MM05 display transitional affinities, related to compositionally intermediate (andesite-like) rocks.

Note that, as discussed in section III.6, PXRF data, although very useful and practical, should always be used with caution due to its associated error. Despite possible systematic and uncorrectable analytical error, the analytical quality of results is enough good to support a trustful comparison with the Aljustrel chemostratigraphy. Also noteworthy, not only "true" lavas were analyzed, volcaniclastic (mostly clast-supported) facies analyses were also considered. The latter rocks may show a slightly different signature due to mixing with siliciclastic material or mixture of material from different volcanic centers (thus different geochemical signatures); however, the deviations caused by the previous factors only produce small and acceptable deviations unaltering the extended chemical interval considered.

After chapter X, minor chemo- and lithostratigraphic similarities remain as to Monte das Mesas VSC correlation with the Aljustrel VSC succession. Only the VSC of the southern sector of Monte das Mesas show faint similar chemical compositions. Felsic rocks in this sector show two major different signatures:

(1) An intermediate composition between qf porphyry and rhyolite B. Petrographic observations exclude a correlation with qf porphyry, the quartz-feldspar megacrystic unit present over much of the central part of the Aljustrel area (Shermerhorn, 1971; Barriga, 1983). On the other hand, petrographic and chemical studies allowed the classification of these rocks as rhyodacites; the dacitic character of these volcanic rocks may explain their chemical behavior when plotted, displaying lower Al_2O_3/TiO_2 and Zr/TiO_2 ratios and frequently higher Zr/Al_2O_3 values.
(2) A well-represented sub-group whose spread is similar to rhyolite A and C, with higher Al_2O_3/TiO_2 values. This group can be divided in two subgroups, according to their affinity to either rhyolite type A or C compositions.

Besides these two major groups, other facies were identified in MM02. A well-marked *andesitic-like* composition is identified towards the end of the drill hole, as described along the relogging, and very rare samples, with very low Al_2O_3/TiO_2, Zr/TiO_2, and Zr/Al_2O_3 values, pointing to to occasional mafic intrusions, also accounted for during the relogging stage.

The VSC section crossed by northern cluster of drill-holes show no relationship with either the section sampled by the southern cluster of drill-holes or the Aljustrel VSC succession described in many works, displaying a major widespread group composed of an internal continuous compositional variation. Exceptionally, volcanic rocks along drill-hole MM05 display frequently an *andesitic-like* character not accounted during re-logging observations, during which most of these rock types were classified as dacites.

The macro and microscopic studies lead to the proposed litho-stratigraphic columns (Figure VII.2). The distinguishing characteristics between the VSC successions drilled at the northern and the southern sectors of Monte das Mesas favored the proposition of two individual lithostratigraphic columns, later supported by the PXRF data, demonstrating very distinctive chemical signatures and magmatic affinities. As mentioned in Chapter VII, when compared to the Aljustrel lithostratigraphic columns, proposed by Shermerhorn (1971), Barriga (1983) and Relvas (1991), the drilled VSC sequence at Monte das Mesas prospect area does not present any particular coarse-grained facies that can be correlated with either the "Megacrystic Tuff Formation" or the "Green Tuff Formation". In addition, the abundance of fine-grained (matrix-supported) volcaniclastic facies over coherent or clast-supported facies and the relative abundance of metapelite rocks, suggests a more distal character.

The presence of voluminous mafic rocks (both intrusive and extrusive) at Monte das Mesas is the most characteristic feature when compared to previously proposed columns. According to Leitão (2014), the mafic rocks represent the last volcanic cycle at Aljustrel. For the Monte das Mesas prospect the same

"relative chronology" is not necessarily true, existing at least two different mafic (extrusive) volcanic impulses: one (β_1) stratigraphically older than several felsic volcanic episodes; and a second (β_2) stratigraphically younger or contemporaneous relatively to the last felsic volcanic episode. However, assuming that these mafic and felsic magmas do not have the same magmatic source (as happens in many other sectors of the IPB), the β_1 and β_2 episodes could be, at some point, contemporaneous to earlier and later felsic volcanic events, respectively. Therefore, two different hypotheses were suggested: (1) the overall VSC sequence intersected at Monte das Mesas correlates to an Upper VSC sequence, and in this case all extrusive mafic episodes are constrained to the upper VSC; or (2) the mafic volcanic episode β_1 refers to a much earlier (mid-lower VSC) volcanic episode, not described by Leitão (2014).

Considering the available observations (at the drill-core scale and petrography) and PXRF results, volcanic rocks in the northern cluster cannot be framed, in any way, with the previous Aljustrel lithostratigraphic columns. However, regarding the southern cluster, a mild correlation can be attempted. The major rhyodacitic subgroup present in this area show no correlation to any unit described by previous authors, on the other hand, the other well-represented subgroup shows chemical similarities to rhyolite A and C. According to Dawson and Caessa (2013), no results regarding rhyolite X, the lowermost volcanic unit, were obtained; still, rhyolite A and C are part of the lower and upper volcanic unit, respectively. For this reason, the VSC succession at the southern sector of Monte das Mesas does not correlate solely with the Upper VCS sequence (as proposed earlier), favoring the second hypothesis anticipated, in which the drilled sequence correlates to a much widespread VSC age range. In this case, β_1 refers to a mid-lower VCS mafic volcanic episode, since it is stratigraphically below the "rhyolite type A", thus pointing to the development of an earlier extrusive mafic episode never described by previous authors in the Aljustrel area.

Although the VSC successions drilled at the northern and southern sectors of Monte das Mesas seem to be independent and conceivably diachronic, both comprise rhyolites (prevailing at North), rhyodacites and dacites (prevailing at South). Assuming that regional petrogenetic relationships are here applicable, these rock types are neither related by fractional crystallization, nor represent differentiation products of basaltic magmas. The different geochemical fingerprints that characterize these different lithologies, evidenced by immobile ratio signatures, suggest that the formation of their protoliths should have comprised distinct degrees of partial crustal (quartz-feldspar) melting without significant mixing or assimilation between these melts. Plus, the existence of *intermediate* rocks suggests a variable admixture of the basaltic magmas with crustal derived felsic melts, indicating a multiphase geodynamic process that involved the rise and emplacement (at different crustal levels) of the mantle-derived basaltic magmas variable modified by crustal contamination. In fact, the IPB geotectonic setting favored the generation of volcanism in confined areas of the thinned continental margin after blocking of subduction to the N. This particular geodynamic evolution allow explain why it was possible to trigger mantle melting able enough to fueling the production of recurrent large volumes of basaltic magmas and simultaneously maintain a high thermal regime throughout the crust for several millions of years. This led to the development of heterogeneous partial melting of the continental crust and/or crustal contamination of basaltic magmas after their fault-controlled rise and emplacement (*e.g.* Munhá, 1983; Thiéblemont *et al*., 1998; Mitjavilla *et al*., 1997; Carvalho et al., 1999; Sisson *et al*., 2005; Annen *et al*., 2006; Jesus *et al*., 2007; Ribeiro *et al*., 2007, 2010; Martin-Izard *et al*., 2015, 2016; Codeço *et al.*, 2018).

The term "volcanic-hosted massive sulfide", or VHMS (sometimes abbreviated as "volcanogenic massive sulfide", VMS), refers to a large family of mainly Cu-Zn (occasionally with minor Pb and Au) deposit types that formed in oceanic lithosphere in either midocean ridge or supra-subduction zone environments, further incorporated into the continental record through accretion events associated with periods of ocean closure and continental assembly/terrane accretion (*e.g.* Meyer, 1988; Barley and

Groves, 1992; Huston *et al*., 2010). In what concerns the IPB, the geological background is somewhat different, because we are dealing with a stretched/thinned continental lithosphere. So, hybrid features between VHMS and sedimentary-exhalative (SEDEX) massive sulfide deposits are common (e.g. Sáez *et al*. 1996, 1999).

In these geological environments, the mineral assemblage that forms as a result of hydrothermal alteration varies as a function of five prevalente factors, namely: (i) temperature, (ii) pressure, (iii) host-rock composition, (iv) fluid composition, and (v) fluid/rock ratio (*e.g*. Robb, 2005). The secondary mineral assemblage at Monte das Mesas is composed of (K-feldspar +) sericite ± chlorite ± carbonates ± sulfides.

Feldspar microphenocrysts are plagioclase, mostly albitic ($Ab_{97.05}An_{1.12}Or_{0.91}$). However, feldspar with the rock groundmass is potassic ($Or_{98.03}Ab_{0.61}An_{0.00}$). This observation is in conformity with typical rhyodacitic magma crystallization; however other secondary alteration/substitution processes could have contributed to the present mineralogical arrangement. Although no alteration halos were observed along the plagioclase phenocrysts, the very reduced groundmass grain size leads to a higher water/rock ratio due to greater surface/volume contact area, favoring the matrix alteration comparatively to the phenocrysts. In this scenario, the rhyodacites show strong enrichment in potassium, specifically adularia replacing plagioclase. This substitution is in conformity with a regional scale oceanic metasomatic event, featuring a virtual total *Na* leaching from the plagioclase crystalline structure, according to the reaction: $K^+_{aq} + NaAlSi_3O_8 = KAlSi_3O_8 + Na^+_{aq}$. This process is consistent with thermodynamic data for the exchange reaction with ocean water at low temperatures (~140ºC) which favors the growth of adularia (Wolery and Sleep, 1946; Andrews, 1978; Bloch and Bishoff, 1979; Fyfe and Donsdale, 1980; Munhá *et al*., 1980). To confirm this hypothesis X-Ray studies should be conducted, to distinguish high-temperature K-feldspar (sanidine) from low-temperature K-feldspar (adularia) since they have the same composition and only their crystalline structure can discriminate both minerals.

Fine-grained with micas (sericites) show deviations towards phengite compositions, as commonly observed either in hydrothermal settings and low-grade metamorphic environments. No compositional differences were related to lithological, textural or chronological distinct contexts, presenting a quite homogeneous composition independent of the context (Table IX.5 and Table IX.6)

When unmetamorphosed to weakly metamorphosed, as in the IPB, differences in *Fe/(Fe+Mg)* ratios in chlorite minerals with distance from the sulfide ores can be observed. High *Fe/(Fe+Mg)* typically occurs in cores of feeder zones and low *Fe/(Mg+Fe)* chlorite occurs along the margins (*e.g.* Robb, 2005).

The analytical results obtained for chlorite show deviations towards the amesite or sudoite (Figure IX.7) compositions along the clinochlore-chamosite line (); chlorites richer in Fe (closer to the chamosite ideal composition) are subordinate. These *Fe*-rich chlorites are present exclusively in samples Z2#15 and MdM02#72. In sample MdM02#72, *Fe*-rich chlorites, although very rare, come along with (also very rare and fine-grained) sulfides, namely galena and chalcopyrite; this secondary mineral assemblage, observed in a highly silicified black metapelite, is a positive and interesting indicator regarding ore-bearing hydrothermal alteration. On the other hand, in sample Z2#15, Fe-rich chlorites show lower *Fe/(Fe+Mg)* but no strict relationship with any textural context, accompanied mostly by pyrite and pyrrhotite; this reflects most probably the influence of local chemical gradients that favored the incorporation of *Fe* in the chlorite structure.

Previously, Barriga (1983) and Relvas (1991), published chlorite analytical results regarding Aljustrel (Feitais) and Gavião, respectively. These results confirm the compositional variability expected for

chlorites generated either during the regional alteration episode (*e.g*. mine tuff, Barriga, 1983; Chlorite I, Relvas, 1991) or in the course of hydrothermal alteration processes related to the massive sulfide formation (*e.g.* stockwork rocks and sulfide ore, Barriga, 1983; Chlorite II, Relvas, 1991). The available results for chlorite from samples Z2#15, MdM02#72 and the remaining Mg-rich chlorites present in samples from Monte das Mesas show a similar composition variability (Table XI.1).

Table XI.1. Statistical median and standard deviation of Mg/Fe and Fe/(Fe+Mg) in chlorite analyses. Chlorite I refers to alteration type 2 and 3, while Chlorite II refers to alteration type 1 (see chapter II.1.4).

			Mg/Fe	***stdev***	***Fe/(Fe+Mg)***	***stdev***
Barriga (1983)	Aljustrel volcanic	Quartz-eye tuff	0.308	0,047	0.765	0,027
		Mine tuff	1.710	0.004	0.369	0,000
	Feitais ore-body	Outer stockwork rocks	0.253	0.022	0.798	0.014
		Stockwork rocks	0.503	0.00	0.666	0.086
		Sulfide ore	0.549	0.284	0.646	0.134
		Hanging-wall Mine Tuffs	0.822	0.350	0.549	0.082
		Metalliferous Sediments	0.049	0.024	0.953	0.022
Relvas (1991)	Chlorite I		2.002	0.543	0.333	0.250
	Chlorite II		0.411	0.177	0.709	0.081
Monte das Mesas	MdM02#72		0.235	0.030	0.810	0.020
	Z2#15		0.545	0.017	0.647	0.007
	Mg-rich		2.760	0.286	0.325	0.035

According to the chlorite-based geothermometers of Jowett (1991), Bourdelle *et al*., (2015), and Vidal *et al*., (2001), the formation temperatures of early (pre-deformation) chlorite in Monte das Mesas rocks vary from ~220 to 380°C, 280 to 470°C and 135 to 400°C, respectively (Table IX.9). Note that two distinct subgroups of pre-deformation chlorite could be delimited according to the temperature estimated on the basis of Vidal *et al*., (2001) approach: 390-400°C and 135-180°C; the lower temperature subgroup can be interpreted as a later stage of a continuous chlorite crystallization, or a result of late chemical readjustments. Since there was no way to resolve late overgrowthing in chlorite aggregates (optically and in high magnification images gathered with electron microprobe), the latter interpretation was initially favored.

To better understand and frame the formation temperatures obtained for pre-deformation chlorite from Monte das Mesas rocks, published analytical results of chlorite from Aljustrel (Feitais) and Gavião (Barriga, 1983; Relvas, 1991) were numerically re-processed to directly compare pre-deformation chlorite temperature formation during the regional alteration or in the course of hydrothermal alteration processes related to the massive sulfide formation (Table XI.2). In fact, the temperature range of pre-deformation chlorite in Monte das Mesas is (generally) consistent with results obtained for chlorite ascribed to regional alteration patterns in Aljustrel and Gavião. This excludes chlorites from samples MdM02#72 and Z2#15, which point to higher formation temperatures comparable with those indicated by chlorites related to ore-bearing hydrothermal alteration at Aljustrel and Gavião.

Luz *et al*., (2019) presents data regarding multi-elemental geochemistry of metassediments from drill-hole MdM02, at similar stratigraphic positioning as sample MdM02#72, interpreted as hydrothermal/mineralization alteration (i) potentionally synchronous of massive sulfide formation and/or (ii) due to late Variscan propagation/reactiviation of strike-slip faults (Figure XI.1). On the other hand, chlorite present in sample MdM02#72 indicates temperature conditions between ~340-390ºC, reflecting conditions slightly below peaking temperatures documented for Variscan metamorphic recrystallization (typical of greenschist facies, 370–450 °C Munhá, 1983, 1990), suggesting an ore-

bearing hydrothermal event stratigraphically above known mineralizations (Paraíso Formation, upper VSC). This conclusion is based on the interpretation of geological cross-section presented in chapter VI.

Table XI.2 Summary of results obtained for chlorite temperature formation (ºC) using different approaches including data from Aljustrel (Barriga, 1983) and Gavião (Relvas, 1991).

Context			**Median**	**STDEV**
Jowett (1991)				
Barriga (1983)	Aljustrel volcanic	Quartz-eye tuff	370	14
		Mine tuff	306	6
	Feitais ore-body	Outer stockwork rocks	408	35
		Stockwork rocks	392	61
		Sulfide ore	362	32
		Hanging-wall Mine Tuffs	342	37
		Metalliferous Sediments	376	6
Relvas (1991)	Chlorite I		302	34
	Chlorite II		364	16
Monte das Mesas	MdM02#72		344	13
	Z2#15		332	7
Vidal *et al.* (2011)				
Barriga (1983)	Aljustrel volcanic	Quartz-eye tuff	464	73
		Mine tuff	164	4
	Feitais ore-body	Outer stockwork rocks	557	58
		Stockwork rocks	437	69
		Sulfide ore	311	53
		Hanging-wall Mine Tuffs	280	37
		Metalliferous Sediments	488	57
Relvas (1991)	Chlorite I		179	42
	Chlorite II		426	56

Monte das Mesas	MdM02#72		-	-
	Z2#15		384	15
Bourdelle et al. (20013)				
Barriga (1983)	Aljustrel volcanic	Quartz-eye tuff	457	49
		Mine tuff	417	15
	Feitais ore-body	Outer stockwork rocks	359	11
		Stockwork rocks	321	42
		Sulfide ore	344	24
		Hanging-wall Mine Tuffs	282	21
		Metalliferous Sediments	-	-
Relvas (1991)	Chlorite I		284	48
	Chlorite II		299	58
Monte das Mesas	MdM02#72		386	56
	Z2#15		443	58

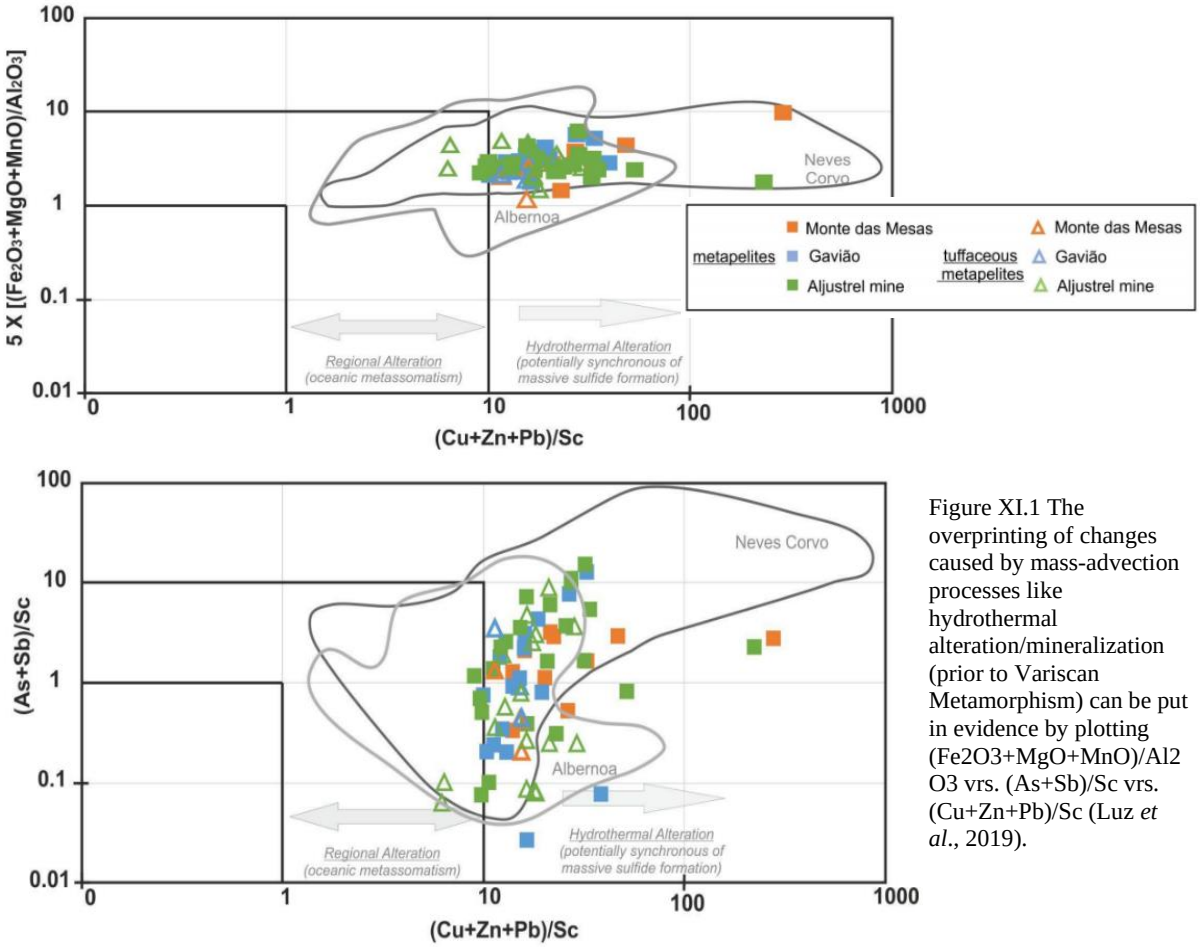

Figure XI.1 The overprinting of changes caused by mass-advection processes like hydrothermal alteration/mineralization (prior to Variscan Metamorphism) can be put in evidence by plotting (Fe2O3+MgO+MnO)/Al2 O3 vrs. (As+Sb)/Sc vrs. (Cu+Zn+Pb)/Sc (Luz *et al*., 2019).

Both sea-floor metasomatic and hydrothermal alteration are subsequently affected by Variscan metamorphic recrystallization; consequently, several compositional features recorded by secondary mineral phases might be obliterated by regional metamorphism, leading to the deviation of sericite towards the phengite series and the compositional re-homogenization of several minerals, in particular the chlorite group.

Also, post-deformation (non-oriented) muscovite and chlorite aggregates (mostly composing the matrix, infilling fractures, crisscrossing Variscan fabrics and feldspar hydrolysis) and post-deformation carbonates were examined; the chlorite geothermometer of Vidal *et al*., (2001) indicate formation temperatures between 130 and 180°C, suggesting that some volcanic rock domains were affected by late fracturing under lower-temperature conditions, possibly during the declining fase of the Variscan metamorphism and deformation.

XII. Concluding remarks

The Monte das Mesas prospect area includes two distinct and independent volcanic centers; however, their spatial and chronological relationships remain unknown. These two VSC successions include sequences of bimodal volcanism, comprising felsic and mafic (with minor intermediate) rock types.

Following the available literature for the IPB, rhyolitic and dacitic facies are nor related to the *andesitic-like* facies by any fractionation processes nor present any evidence of resulting from the differentiation of basaltic magmas. The large diversity of rhyolitic rocks likely results from different degrees of partial melting of the continental (quartz-feldspathic) crust, induced by multiple basaltic pulses of different magnitude and emplaced at various depths. If so, the rhyodacite, dacite and intermediate rocks reflect different crustal contamination degrees of the basaltic magmas.

Incompatible trace element ratios show that felsic volcanic rocks composing the Northen VSC succession of Monte das Mesas present a toleiitic affinity whereas those in the Southern VSC succession display a calc-alkaline affinity, similar to equivalent rock types in Aljustrel. Immobile element ratios together with lithoestratigraphic information supported on interpretative geological crossections proved that, in contrast to the available literature, extrusive mafic volcanic episodes are nor exclusive to the upper VCS in Aljustrel; some of the intersected spilitic lava flows should be part of the early-mid VSC succession.

The majority of the volcanic rocks denote mineralogical evidence of metasomatic and/or hydrothermal activity prior to the Varican orogeny. The typical secondary mineral assemblage is composed of k-feldspar, phyllosilicates (sericite>>chlorite), epidote, carbonates and minor to trace amounts of sulfides (*e.g.* pyrite, pyrrhotite, sphalerite, galena, and chalcopyrite).

At the Monte das Mesas prospect, the chlorite geothermometers point to temperatures between 400-390°C and 180-135°C for pre-deformation chlorites (considering the numerical approach reported in Vidal (2004). All the higher temperatures refer to chlorite aggregates associated to sulfide phases; these chlorites display high *Fe/(Fe+Mg)* ratios and were found in a unique sample (MdM02#72), pointing to temperature conditions between ~340-390ºC; These temperatures reflect conditions slightly below the peaking temperatures documented for Variscan metamorphic recrystallization, suggesting an ore-bearing hydrothermal event stratigraphically above known mineralizations (Paraíso Formation, upper VSC), that should be further investigated.

Data obtained throughout this work indicate that no close parallelism can be made with the Aljustrel ore centre, denoting an independent geological setting, and evidence no proximity to a (typical) massive sulfide feeder zone.

These facts reinforce that, although the IPB is a metallogenetic province of excellence worldwide, continuously explored and studied, its geological setting developed a vast diversity of very different metallogenetic settings. Therefore, there is a need to search and develop innovative methods and models capable of defining new mineralogical and geochemical criteria to serve as guides for suitable mineral exploration in the IPB context.

XIII. References

Almodóvar, G.R., Sáez, R., Pons, J., Maestre, A., Toscano, M., and Pascual, E. (1998). *Geology and genesis of the Aznalcóllar massive sulphide deposits, Iberian Pyrite Belt, Spain*, Mineralium Deposita, 33, 111-136.

Andrews, A.J. (1978). *Petrology and geochemistry of alteration in layer 2 basalts, DSDP leg 37*. Doctoral Thesis, University of Western Ontario.

Annen, C., Blundy, J.D., Sparks, R.S.J., (2006). *The genesis of intermediate and silicicmagmas in deep crustal hot zones*, Journal of Petrology 47, 505–539.

Armbruster, T.; Bonazzi, P.; Akasaka, M.; Bermanec, V.; Chopin, C.; Gieré, R.; Heuss-Assbichler, S.; Menchetti, S.; Pan, Y. and Pasero, M. (2006). *Recommended nomenclature of epidote-group minerals*, European Journal of Mineralogy, 18, 551–567.

Bailey, S.W. (1984). *Crystal chemistry of true micas*. In: Micas (S.W. Bailey, .eds), Mineralogical Society of America, Reviews in Mineralogy 13, 347-403.

Barley, M.E. and Groves, D.I. (1992*). Supercontinent cycles and distribution of metal deposits through time*, Geology, 20, 291-94.

Barriga, F.J.A.S. (1983). *Hydrothermal Metamorphism and Ore genesis at Aljustrel, Portugal*. Unpublished PhD thesis, University of Western Ontario, 386 pp.

Barriga, F. (1990). *Metallogenesis in the Iberian Pyrite Belt*. In: Dallmeyer, R.D. & Martinez García, E., (Eds.), *Pre-Mesozoic Geology of Iberia*, Berlin: Springer-Verlag, 369-79.

Barriga, F. and Carvalho, D. (1983). *Carboniferous Volcanogenic Sulphide Mineralizations in South Portugal (Iberian Pyrite Belt)*, Memórias dos Serviços Geológicos de Portugal, Nova Série. - Nº 29 (1983), 99-113.

Barriga, F., Carvalho, D. and Ribeiro, A. (1997). *Introduction to the Iberian Pyrite Belt. In: Barriga, F., Carvalho, D., eds, Geology and VMS Deposits of the Iberian Pyrite Belt*, Society of Economic Geologists Guidebook Series, 27, 1-20.

Barriga, F. and Fyfe, W. (1988). *Giant pyritic base-metal deposits: The example of Feitais (Aljustrel, Portugal)*, Chemical Geology, 69, 331-43.

Barrett, T.J. (1999). *Stratigraphic and Alteration Relations at the Feitais VMS Deposit, Aljustrel, Portugal*. Unpublished report commissioned by EuroZinc Mining Corporation.

Barrett, T.J. (2009). *Geology and Chemostratigraphy of Selected 2008 Drillholes at the Gavião, Feitais and Lousal Deposits, Portugal*. Unplublished report commissioned by Lundin Mining Corporation.

Barrett, T.J., Dawson, G.L., and MacLean, W.H. (2008). *Volcanic stratigraphy, alteration, and sea-floor setting of the Paleozoic Feitais massive sulfide deposit, Aljustrel, Portugal*, Economic Geology, 103, 215-39.

Barrett, T.J. and MacLean, W.H. (1991), *Chemical, mass, and oxygen isotope changes during extreme hydrothermal alteration of an Archean rhyolite, Noranda, Quebec*, Economic Geology, 86, 406–14.

Barrett, T.J. and MacLean, W.H. (1994). *Chemostratigraphy and hydrothermal alteration in exploration for VHMS deposits in greenstones and younger volcanic rocks*, Geological Association of Canada Short Course Notes, 11, 433–67.

Barrett, T.J. and Maclean, W.H. (1999). *Geological Relations at the Feitais VMS Deposit and in some areas at Aljustrel, Portugal.* Unpublished report commissioned by EuroZinc Mining Corporation.

Barrett, T.J., MacLean, W.H., and Tennant, S.C. (2001), *Volcanic sequence and alteration at the Parys Mountain volcanic-hosted massive sulfide deposit, Wales, United Kingdom: Applications of immobile element lithogeochemistry*, Economic Geology, 96, 1279–305.

Barrie, C.T., Amelin, Y., and Pascual, E. (2002). *U-Pb geochronology of VMS mineralization in the Iberian Pyrite Belt*, Mineralium Deposita, 37, 684-703.

Bayliss, P. (1975). *Nomenclature of the trioctahedral chlorites*, Canadian Mineralogist 13, 178-180.

Bloch S and Bishop J.L. (1979). *The effect of low-temperature alteration of basalt on the oceanic budget of potassium*, Geology, 7,193-96.

Boogaard, M. and Schermerhorn, L.J.G. (1981). *Conodont faunas from Portugal and southwestern Spain. Part 6. A Lower Famenian conodont fauna at Monte do Forno da Cal (South Portugal)*, Scripta Geologica 63, 1-16.

Bourdelle, F., Parra, T., Chopin, C., Beyssac, O. (2013). *A new chlorite geothermometer for diagenetic to low-grade metamorphic conditions*, Contributions to Mineralogy and Petrology, 165, 723–35.

Caritat, P., Hutcheon, I. and Walshe, L. (1993). *Chlorite Geothermometry: A review*, Clays and Clay Minerals, 41, n2, 219-39.

Carvalho, D. (1979). *Geologia, metalogenia e metodologia da investigação de sulfuretos polimetálicos do Sul de Portugal*, Comunicações dos Serviços Geológicos de Portugal, 65, 169-91.

Carvalho, D., Barriga, F.J.A.S. & Munhá, J. (1999). *Bimodal Siliciclastic systems: The case of the Iberian Pyrite Belt. In: Volcanic associated massive sulfide deposits*, In *Processes and examples in modern and ancient settings* (C.T. Barrie & M.D. Hannington, eds.), Reviews Economic Geology, 375-408.

Cathelineau, M. (1988). *Cation site occupancy in chlorites and illites as a function of temperature*, Clays and Clay Mineralogy 23, 471-485.

Cathelineau, M. and Nieva, D. (1985). *A chlorite solid solution geothermometer. The Los Azufres (Mexico) geothermal system*, Contributions to Mineralogy and Petrology 91, 235-44.

Claiborne L.E., Miller C.F., Walker B.A., Wooden J.L., Mazdab F.K., Bea F. (2006). *Tracking magmatic processes through Zr/Hf ratios in rocks and Hf and Ti zoning in zircons: An example from the Spirit Mountain batholith, Nevada*, Mineralogical Magazine 70, 517-43.

Codeço, M. (2015). *Estudo comparativo das sequências vulcânicas constituintes dos eixos Ervidel-Roxo e Figueirinha-Albernoa (Faixa Piritosa Ibérica) e respectiva relevância na prospecção de sulfuretos maciços polimetálicos*. MSc thesis, Lisbon University, 253.

Codeço, M., Mateus, A., Figueiras, J., Rodrigues, P. and Gonçalves, L. (2018). *Development of the Ervidel-Roxo and Figueirinha-Albernoa volcanic sequences in the Iberian pyrite Belt, Portugal: Metallogenic and geodynamic implications*, Ore Geology Reviews, 98, 80-108.

Codeço, M., Mateus, A., Figueiras, J., Rodrigues, P. and Gonçalves, L. (2018). *Zircon Saturation and Ti-in-Zircon Thermometry Applied to Felsic Volcanics of the Iberian Pyrite Belt; Useful Exploration Guides to Massive Sulphide Ores?*, Ore Geology Reviews, 98, 80-108.

Dawson, G.L. & Caessa P. (2003). *Geology of the Aljustrel Mine area, southern Portugal (Aljustrel Field Trip Guide)*.

Deer, W.A., Howie, R.A., and Zussman, J. (2008). *Minerais constituintes das rochas – uma introdução*. Tradução de C. A. R. Macedo. Fundação Calouste Gulbenkian, 727.

Eden, C. F. (1991). *Tectonostratigraphic analysis of the northern extent of the oceanic exotic terrane, northwestern Huelva Province, Spain*. PhD Thesis, University of Southampton, 281.

Ferry J.M. and Watson E.B. (2007). *New thermodynamic models and revised calibrations for the Ti-in-zircon and Zr-in-rutile thermometers,* Contributions to Mineralogy and Petrology 154, 429-37.

Fonseca, P. and Ribeiro, A. (1993). *Tectonics of the Beja-Acebuches Ophiolite: a major structure in the Iberina Variscan Foldbelt*. Geologisches Rundschau 82, 440-47.

Fyfe, W.S., and Lonsdale, P. (1981). *Ocean floor hydrothermal activity*, In *The Sea*, 7, (C. Emiliani edited), John Wiley & Sons, New York, 589-638.

Gandhi, S.M. and Sarkar, B.C. (2016). *Essentials of Mineral Exploration and Evaluation*, 410.

Grosch EG, Vidal O, Abu-Alam T, and McLoughlin, N. (2012). *PTconstraints on the metamorphic evolution of the Paleoarchean Kromberg type-section, Barberton Greenstone Belt, South Africa*, Journal of Petrology 53, 513–45.

Harrison, T.M.; Watson, E.B. and Aikman, A.B. (2007). *Temperature spectra of zircon crystallization in plutonic rocks,* Geology 35, 365-68.

Huston, D. L., Pehrsson, S., Eglington, B. M. and Zaw, K. (2010). *The geology and metallogeny of volcanic-hosted massive sulfide deposits: variations through geologic time and with tectonic setting*, Economic Geology, 105, 571–91

Inoue, A., Meunier, A., Patrier-Mas, P., Rigault, C., Beaufort, D. and Vieillard, P. (2009). *Application of chemical geothermometry to low-temperature trioctahedral chlorites*, Clays and Clay Mineralogy, 57, 371–82.

Inverno, C., Díez-Montes, A., Rosa, C., García-Crespo, J., Matos, J., García-Lobón, J.L., Carvalho, J., Bellido, F., Castello.Branco, J.M., Ayala, C., Batista, M.J., Rubio, F., Granado, I., Oliveira, J.T., Rey, C., Araújo, V., Sánchez-García, T., Pereira, Z., Represas, P., Solá, R. and Sousa, P. (2015*). Introduction and Geolocial Setting of the Iberian Pyrite Belt*., In Weihed, P. (eds) *3D, 4D and Predictive Modelling of Major Mineral Belts in Europe*.

Ishikawa, Y., Sawaguchi, T., Iwaya, S., and Horiuchi, M. (1976). *Delineation of prospecting targets for Kuroko deposits based on modes of volcanism of underlying dacite and alteration halos,* Mining Geology, 26, 105–17.

Jesus, A.; Munhá, J.; Mateus, A.; Tassinari, C. and Nutman, A. (2007). *The Beja layered gabbroic sequence (Ossa–Morena Zone, Southern Portugal): geochronology and geodynamic implications*, Geodinamica Acta 20, 139-57.

Jorge, R. (2000). *Estudo mineralógico e metalogenético do depósito manganesífero de Soloviejo, Huelva, Espanha*. Master Thesis, Universidade de Lisboa, 134.

Jorge R., Pinto A., Tassinari C., Relvas J., Munhá J. and Andrew C. (2007). *VHMS metal sources in the Iberian Pyrite Belt: new insights from Pb isotope data*, Proceedings of the 9th Biennial SGA Meeting, 1097-1100.

Jowett, E.C. (1991). *Fitting iron and magnesium into the hydrothermal chlorite geothermometer*, GAC/MAC/SEG Joint Annual Meeting (Toronto, May 27-29, 1991), Program with Abstracts 16, A62.

Kranidiotis, P. and MacLean, W. H. (1987). *Systematics of chlorite alteration at the Phelps Dodge massive sulfide deposit, Matagami, Quebec,* Economic Geology 82, 1898–911.

Laird, J. (1988). *Chlorites: metamorphic petrology,* In *Hydrous Phyllosilicates (Exclusive of Micas)* (S.W. Bailey, eds.), Reviews in Mineralogy 19, Mineral Society of America, 405-53.

Lanari, P., Wagner, T. and Vidal, O. (2014). *A thermodynamic model for di-trioctahedral chlorite from experimental and natural data in the system MgO–FeO–Al2O3–SiO2–H2O: applications to P–T sections and geothermometry*, Contributions to Mineralogy and Petrology, 167, 968.

Large, R.R., Gemmerl, J.B., Paulick, H., and Huston, D.L. (2001). *The alteration box plot: a simple approach to understanding the relationship between alteration mineralogy and litogeochemistry associated with volcanichosted massive sulphide deposits*, Economic Geology, 96, 957-71.

Leake, B, Woolley, A., Birch, W.D., Burke, E.A.J., Ferraris, G, Grice, J.D., Howthorne, F.C., Kisch, H.J., Krivovichev, V.G., Schumacher, J.C., Stephenson, N.C. and Whittaker, E.J.W. (2004). *Nomenclature of amphiboles: Additions and revisions to the International Mineralogical Association's amphibole nomenclature*, American Mineralogist 89, 883-887

Leca, X., Ribeiro, A., Oliveira, J.T., Silva, J.B., Albouy, L., Carvalho, D., and Merino, F. (1983). *Cadre Géologique des Mineralisations de Neves Corvo (Baixo Alentejo, Portugal)*, Lithostratigraphie, Paléologéographie et Tectonique. Mémoire nº 21 du Bureau de Recherches Géologiques et Minières.

Leistel, J.M., Bonijoly, D., Braux, C., Freyssinet, P., Kosakevitch, A., Leca, X., Lescuyer, J.L., Marcoux, E., Milési, J.P., Piantone, P., Sobol, F., Tegyey, M., Thiéblemont, D. and Viallefond, L. (1994). *The massive sulphide deposits of the South Iberian Pyrite Province: geological setting and exploration criteria*, BRGM, Doc. 234, 236.

Leistel, J.M., Marcoux, E., Thiéblemont, D., Quesada, C., Sánchez A., Almodóvar, G.R., Pascual, E., and Sáez, R., (1998). *The Volcanic-hosted massive sulphide deposits of the Iberian Pyrite Belt*, Mineralium Deposita, 33, 2-30.

Leitão, J.C.R., (2014). *Architecture of the Aljustrel volcanic-sedimentary basin*, Comunicações Geológicas (2014) 101, Especial I, 469-74.

Luz, F., Mateus, A., and Figueiras, J (2018). *Elemental geochemistry of metasediments from the Aljustrel area, Iberian Pyrite Belt (IBP), Portugal: Implications for mineral exploration*, SEG Conference: Metals, Minerals, and Society Keystone, Colorado, USA, September 22-25th.

Luz, F**.**, Mateus, A., Figueiras, J., Tassinari, C.C.G., Ferreira, E. and Gonçalves, L., *(*2019). *Recognizing metasedimentary sequences potentially hosting concealed massive sulfide accumulations in the Iberian Pyrite Belt using geochemical fingerprints*, Ore Geology Reviews, 107, 937-98.

MacLean, W.H., and Kranidiotis, P. (1989.) *Immobile elements as monitors of mass transfer in hydrothermal alteration: Phelps Dodge massive sulfide deposit, Matagami, Quebec*, Economic Geology, 82, 951–62.

MacLean, W.H. (1990). *Mass change calculations in altered rock series*, Mineralium Deposita, 25, 44–9.

Martin-Izard, A., Arias, D., Arias, M., Gumiel, P., Sanderson, D.J., Castañon, C., Lavandeira, A. and Sanchez, J. (2015). *A new 3D geological model and interpretation ofstructural evolution of the world-class Rio Tinto VMS deposit, Iberian Pyrite Belt (Spain)*, Ore Geology Reviews 71, 457–76.

Martín-Izard, A., Arias, D., Arias, M., Gumiel, P., Sanderson, D.J., Castañon, C. and Sanchez, J. (2016). *Ore deposit types and tectonic evolution of the Iberian Pyrite Belt: fromtranstensional basins and magmatism to transpression and inversion tectonics*, Ore Geology Reviews 79, 254–67.

Mateus, A. (1996). *A variabilidade composicional das micas potássicas dioctaédricas como indicador das condições P-T de deformação; ensaio de aplicação às fácies graníticas sinorogénicas adjacentes ao segmento sul do troço transmontano da falha da Vilariça (NE de Portugal)*, Gaia 13, 9-41.

Mateus, A., Figueiras, J., Monteiro Santos, F., Luz, F., Khalil, M., Codeço, M., Gonçalves, S., Godinho, E., Farzamian, M., Moreira, B., Rodrigues, P., Jorge, R.C.G.S. and Henriques, C. (2015). *Prospecção mineral no "Polígono Albernoa" (Faixa Piritosa Ibérica, Portugal); avaliação integrada de três áreas prioritárias recorrendo a dados multidisciplinares e follow up*. Relatório Final apresentado à Empresa Portuguesa de Obras Subterrâneas S.A., FCUL, Lisboa, 291.

Mathur, R.; Ruiz, J. and Tornos, F. (1999). *Age and sources of the ore at Tharsis and Rio Tinto, Iberian Pyrite belt, from Re-Os isotopes*, Mineralium Deposita 34, 790-93.

McPhie, J., Doyle and Allen., R. (1993). *Volcanic textures: a guide to the interpretation of textures in volcanic rocks*, Centre for Ore Deposit and Exploration Studies, University of Tasmania, 198.

Meyer, C. (1988). *Ore deposits as guides to the geologic hstory of Earth*, Annual Reviews in Earth Planetary Science, 16, 147-71.

Mitjavila, J., Marti, J. and Soriano, C. (1997). *Magmatic evolution and tectonic setting of the Iberian Pyrite Belt volcanism*, Journal of Petrology 38, 727-55.

Morimoto, N., Fabries, J., Ferguson, A.K., Ginzburg, I.V., Ross, M., Seifert, F.A. and Zussman J. (1988). *Nomenclature of pyroxenes*, American Mineralogist 73, 1123-33.

Munhá, J. (1976). *Nota preliminar sobre o metamorfismo na Faixa Piritosa Portuguesa*, Comunicações dos Serviços Geológicos Portugueses 60, 151 – 61.

Munhá, J., Fyfe, W.S., and Kerrich (1980). *Adularia, the Characteristic Mineral of Felsic Spilites*, Contributions to Mineralogy and Petrology, 75, 15-19.

Munhá, J. (1981). *Igneous and Metamorphic petrology of the Iberian Pyrite Belt Volcanic Rocks*. Unpublished PhD thesis, University of Western Ontario, 710.

Munhá, J. (1983). *Low-grade regional metamorphism in the Iberian Pyrite Belt*, Comunicações Serviços Geológicos Portugal, 69, 3-35.

Munhá, J., Relvas, J.M.R.S., Barriga, F.J.A.S., Conceição, P., Jorge, R.C.G.S., Mathur, R., Ruiz, J. and Tassinari, C.C.G. (2005). *Osmium isotope systematics in the Iberian Pyrite Belt*, In Mineral deposit research: Meeting the Global Challenge (J. Mao& F.P. Bierlein, eds.). Springer, Berlin, 663-66.

Nehlig P., Cassard, D. and Marcoux, E. (1998). *Geometry and Genesis of Feeder Zones of Massive Sulfide Deposits: Constrains From Rio Tionto Ore Deposit (Spain)*, Mineral Deposita, 33, 137-49.

Oliveira, J. T. (1983). T*he marine Carboniferous of South Portugal: a stratigraphic and sedimentologic approach*, In: Sousa, M., Oliveira, J.T. (eds.), *The Carboniferous of Portugal*, Memória dos Serviços Geológicos de Portugal, 29, 3-37.

Oliveira, J.T. (1990). *Stratigraphy and syn-sedimentary tectonism in the South Portuguese Zone*, In Dallmeyer, R.D., Martínez García, E. (eds.), *Pre-Mesozoic Geology of Iberia*, Springer, Berlin, 334-47.

Oliveira, J.T.; Relvas, J.M.R.S.; Pereira, Z.; Matos, J.X.; Rosa, C.J.; Rosa, D.; Munhá, J.M.; Jorge, R.C.G.S., and Pinto, A.M.M. (2006). *O Complexo Vulcano-Sedimentar da Faixa Piritosa Ibérica:*

estratigrafia, vulcanismo, mineralizações associadas e evolução tectonoestratigráfica no contexto da Zona Sul Portuguesa, In *Geologia de Portugal na Ibéria* (R. Dias, A. Araújo, P. Terrinha and J.C. Kullberg, eds.), VII Congresso Nacional de Geologia, Univ. Évora, Portugal, 207-44.

Oliveira, T., Relvas, J., Pereira, Z., Matos, J., Rosa, C., Rosa, D., Munhá, J., Fernandes, P., Jorge, R. and Pinto, A. (2013). *Geologia da Zona Sul Portuguesa, com ênfase na estratigrafia e na vulcanologia física, química e mineralizações da Faixa Piritosa*, In Araújo, A., Dias, R., Kullberg, J.C. andTerrinha, P., Geologia de Portugal, 1, 765-973.

Oliveira, J.T., Rey, C., Araújo, V., Sánchez-García, T., Pereira, Z., Represas, P., Solá, A.R. and Sousa P. (2015). *Introduction and Geological Setting of the Iberian Pyrite Belt*, Mineral Resource Reviews, 191-208.

Pereira, Z., Matos, J., Fernandes, P. and Oliveira J.T. (2008). *Palynostratigraphy and Systematic Palynology of the Devonian and Carboniferous Successions of the South Portuguese Zone, Portugal*, Memória Nº 34 do INETI, 1-176.

Quesada, C., Fonseca, P., Munhá, J., Oliveira, J. and Ribeiro, A. (1994). *The Beja-Acebuches Ophiolite (Southern Iberia Variscan fold belt): geological characterization and geodynamic significance*, Boletín Geológico y Minero 105-1, 3-49.

Radoslovich, E.W. (1960). *The structure of muscovite* $KAl_2(AlSi_2O_{10})(OH)_2$, Acta Crystallographica, 13, 919-32.

Relvas J.M.R.S. (1991). *Estudo Geológico e Metalogenético da área do Gavião, Baixo Alentejo*. Unpublished MSc thesis, Portugal, University of Lisbon, 250.

Relvas, J.M.R.S. (2000). *Geology and metallogenesis at the Neves-Corvo deposit, Portugal*, Unpublished Doctoral Thesis, Portugal, University of Lisbon, 319.

Relvas, J.M.RS., Tassinari, J., Munhá, J. and Barriga, F.J.A.S. (2001). *Multiple sources for ore-forming fluids in the Neves Corvo VHMS deposit of the Iberian Pyrite Belt (Portugal): strontium, neodymium and lead isotope evidence*, Mineral Deposita, 36, 416-27.

Relvas, J.M.R.S., Barriga, F.J.A.S., Ferreira, A., Noiva, P.C., Pacheco, N,, and Barriga, G. (2006ª). *Hydrothermal alteration and mineralization in the Neves-Corvo volcanic-hosted massive sulfide deposit, Portugal I, Geology, mineralogy, and geochemistry*, Economic Geology 101, 753- 90.

Relvas, J.M.R.S., Barriga, F.J.A.S., and Longstaffe, F.J., (2006b). *Hydrothermal alteration and mineralization in the Neves-Corvo volcanic-hosted massive sulfide deposit, Portugal II, Oxygen, hydrogen, and carbon isotopes*, Economic Geology 101, 791-804.

Relvas, J., Barriga, F., Carvalho, J., Pinto, A., Matos, J., Rosa, C. and Pereira, Z. (2011). *Structure, stratigraphy and hydrothermal alteration at the Gavião orebodies, Aljustrel: reconstruction of a dismembered ore-forming system at the Iberian Pyrite Belt and implications for exploration*, 11th SGA Biennial Meeting, Let's Talk Ore Deposits, 772-74.

Ribeiro, A., Quesada, C. and Dallmeyer, R. D. (1990*). Geodynamic evolution of the Iberian Massif*, In *PreMesozoic Geology of Iberia* (R. D. Dallmeyer & E. Martínez García, eds), Berlin: Springer-Verlag, 334-47.

Ribeiro, A. and Silva, J.B. (1983). *Structure of south portuguese zone*, In: Sousa, M.J.L. and Oliveira, J.T. (Eds.), *The Carboniferous of Portugal*, Memórias dos Serviços Geológicos de Portugal, 29: 91-7.

Ribeiro, A., Munhá, J., Dias, D., Mateus, A., Pereira, E., Ribeiro, L., Fonseca, P., Araújo, A., Oliveira, J.T., Romão, J., Chaminé, H., Coke, C. and Pedro, J. (2007). *Geodynamicevolution of the SW Europe Variscides*, Tectonics 26, TC6009.

Ribeiro, A., Munhá, J., Fonseca, P.E., Araújo, A., Pedro, J.C., Mateus, A., Tassinari, C., Machado, G. and Jesus, A.P. (2010). *Variscan ophiolite belts in the Ossa-Morena Zone (Southwest Iberia): geological characterization and geodynamic significance*, Gondwana Research 17, 408–21.

Rosa, D., Inverno, C., Oliveira, V., and Rosa., C. (2004). *Geochemistry of Volcanic Rocks, Albernoa Area, Iberian Pyrite Belt, Portugal*, International Geology Reviews 46(4), 366-83.

Rosa, C. (2007). *Facies Architecture of the Volcanic Sedimentary Complex of the Iberian Pyrite Belt, Portugal and Spain*, PhD thesis, University of Tasmania.

Rosa D., Finch A.; Andersen, T. and Inverno, C. (2009). *U–Pb geochronology and Hf isotope ratios of magmatic zircons from the Iberian Pyrite Belt*, Mineralogy and Petrology 95, 47–69

Sáez. R. and Almodóvar, G.R. (1993). Na *introduction to the Ore Geology of the Iberian Pyrite Belt. 2nd Biennal SGA Meeting, Granada*, Field Trip Guide Book: 1-17.

Sáez, R., Almodóvar, G.R. and Pascual, E., (1996). *Geological constrains on massive sulphide genesis in the Iberian Pyrite Belt*, Ore Geology Reviews 11, 429-51.

Sáez, R., Pascual, E., Toscano, M. and Almodóval, G.R. (1999). *The Iberian type of volcano-sedimentary massive sulphide deposits*, Mineralium Deposita 34, 549-70.

Saéz, R., Moreno, C., González, F. and Almodóvar, G.R. (2011). *Black shales and massive sulfide deposits: causal or casual relationships? Insights from Rammelsberg, Tharsis, and Draa Sfar*, Mineralium Deposita, 46, nº 5-6, 585-614.

Schermerhorn, L.J.G. (1971). *An outline stratigraphy of the Iberian Pyrite Belt*, Boletín Geológico y Minero, 82 (3/4): 239-68.

Schermerhorn, L.J.G. (1975). *Spilites, regional metamorphism and subduction in the Iberian Pyrite Belt: Some comments*, Geologie en Mijnbouw, 54, 23-35.

Schermerhorn, L.J.G. and Stanton, W.I. (1969). *Folded overthrusts at Aljustrel (south Portugal)*, Geological Magazine 106, 130-41.

Silva, J.B., Oliveira, J.T. and Ribeiro, A. (1990). *South Portuguese Zone. Part VI. Structural outline*, In Dallmeyer, R.D., Martínez García, E. (eds.), *Pre-Mesozoic Geology of Iberia*, 348-362.

Silva, J.B. and Pereira, M.F. (2004). *Transcurrent continental tectonics model for the Ossa-Morena Zone Neoproterozoic–Paleozoic evolution, SW Iberian Massif, Portugal*, Internation Journal of Earth Sciences (Geol. Rundsch) 93, 886-96.

Sisson, T.W., Ratajeski, K., Harkins, W.B. and Galzner, A.F. (2005). *Voluminous graniticmagmas from common basaltic sources*, Contributions to Mineralogy and Petrology 148, 635–61.

Solomon, M., Tornos, F., Large, R.R., Badham, J.N.P., Both, R.A. and Zaw, K. (2004). *Zn-Pb-Cu volcanic-hosted massive sulphide deposits: criteria for distinguishing brine pool-type from black smoker-type sulphide deposition*, Ore Geology Reviews, 25, 259-83.

Strauss, G.K. and Madel, J. (1974). *Geology of Massive Sulphide Deposits in the Spanish-Portuguese Pyrite Belt*, Geol. Rundsch 63(1), 191-211.

Strauss, G.K., Madel, J. and Fernandez Alonso, F. (1977). *Exploration practice for stratabound volcanogenic sulphide deposits in the Spanish-Portuguese Pyrite Belt: geology, geophysics and geochemistry*, In Klem, D.D., and Schneider, H.J. eds *Time and stratabound ore deposits*, Berlin Springer-Verlarg, 55-93.

Thiéblemont, D and Tégyey, M. (1994). *Une discrimination géochimique des roches différenciées témoin de la diversité d'origine et de situation tectonique des magmas calco-alcalins,* C.R. Acad. Sci. Paris, T. 319 (série II), 87-94.

Thiéblemont, D., Pascual, E. and Stein, G. (1998). *Magmatism in the Iberian Pyrite Belt: petrological constraints on a metallogenetic model*, Mineralium Deposita 33, 98-110.

Tornos, F., Conde, C., Solomon, M. and Spiro, B. (2003). *Effects of oxic/anoxic seafloor on the formation and preservation of shale-hosted massive sulphides, Iberian Pyrite Belt*, Mineral Exploration and Sutainable Development, 191-94.

Tornos, F. (2006). *Environment of formation and styles of volcanogenic massive sulfides: The Iberian Pyrite Belt*, Ore Geology Reviews, 28, 259–307.

Tornos, F., Casquet, C. and Relvas., J (2005). *Transpressional tectonics, lower crust decoupling and intrusion of deep mafic sills: A model for the unusual metallogenesis of SW Iberia*, 27, 133-63.

Tornos, F., Peter, J.M., Allen, R. and Conde, C. (2015). Controls on the siting and style of volcanogenic massive sulphide deposits, Ore Geology Reviews, 68, 142-63.

Vidal, O., Parra, T., Trotet, F. (2001). *A thermodynamic model for Fe-Mg aluminous chlorite using data from phase equilibrium experiments and natural pelitic assemblages in the 100 to 600ºC, 1 to 25 kb range*, American Journal of Science 301, 557-92.

Vidal, O. Parra, T. and Vieillard, P. (2005). *Thermodynamic properties of the Tschermak solid solution in Fechlorite: Application to natural examples and possible role of oxidation*, American Mineralogist 90, 347-58.

Vidal, O., Andrade, V., Lewin, E., Munoz, M., Parra, T. and Pascarelli, S. (2006). *P-T-deformation-Fe^{3+}/Fe^{2+} mapping at the thin section scale and comparison with XANES mapping: Application to a garnetbearing metapelite from the Sambagawa metamorphic belt (Japan)*, Journal of Metamorphic Geology 24, 669-83.

Walshe, J.L. (1986). *A six-component chlorite solid solution model and the conditions of chlorite formation in hydrothermal and geothermal systems*, Economic Geology, 81, 681–703.

Watson E.B., Wark D.A. and Thomas J.B. (2006). *Crystallization thermometers for zircon and rutile*, Contributions to Mineralogy and Petrology 151, 413-33.

Whitney, D.L. and Evans, B. W. (2010). *Abbreviations for names of rock-forming minerals*, American Mineralogist, 95, 185–87.

Wolery TJ and Sleep N.H. (1976). *Hydrothermal circulation and geochemical flux at mid-ocean ridges*, Journal of Geology, 84, 249-75.

Zane, A., Sassi, R. and Guidotti, C.V. (1998). *New data on metamorphic chlorite as petrogenetic indicator mineral, with special regard to greenshist-facies rocks*, The Canadian Mineralogist, 36, 713-26.

Zang, W. and Fyfe, W.S. (1995). *Chloritization of the hydrothermally altered bedrock at the Igarapá Bahia gold deposit, Carajás, Brazil*. Mineralium Deposita, 30, 30–38.

APPENDIX

Appendix I Detection limits and analytical condition of the microprobe for each mineral group.

Element	Crystals	Standards	Detection limit (ppm)
		FELDSPAR	
Mn	PETJ	Bustamite	367
Al	TAP	Pyrope	201
Fe	LIFH	Almandine	279
F	TAP	Fluorite	559
Cl	PETH	Tugtupite	91
Si	PETH	Sanidine	95
Mn	PETJ	Bustamite	230
Na	TAP	Tugtupite	97
		PYROXENE	
Cr	PETJ	Chromium Oxide	168
Fe	LIFH	Almandine	172
Mg	TAP	Diopside	91
Zn	LIFH	Sphalerite	497
K	PETH	Sanidine	57
Al	TAP	Plagioclase	94
Ca	PETJ	Diopside	67
		AMPHIBOLE	
Ti	PETJ	Rutile	249
Al	TAP	Plagioclase	103
Mg	TAP	Diopside	102
Na	TAP	Jadeite	111
F	TAP		1352
Zn	LIF	Sphalerite	746
Cr	PETJ	Chromium Oxide	230
Cl	PETJ	Tugtupite	103
Fe	LIFH	Almandine	238
Ca	PETH	Diopside	86
K	PETH	Sanidine	78
Si	PETH	Diopside	113
		MICA	
Si	PETJ	Olivine	273
Rb	PETH	CAL.STD	499
Ti	PETJ	Rutile	211
Na	TAP	Jadeite	115
K	PETH	Sanidine	61
Cr	PETJ	Chromium Oxide	182
Mg	TAP	Chlorite	109
Cs	PETJ	Pollucite	351
Ba	LIFH	Barite	328
Mn	PETJ	Bustamite	244
Al	TAP	Almandine	126
Ni	LIF	Nickel Silicide	380
Fe	LIFH	Kaersutite	186
F	TAP	Fluorite	770
Cl	PETJ	Tugtupide	106
F	TAP	Fluorite	938
		CHLORITE	
Ca	PETJ	Bustamite	134
Si	PETH	Pyrope	115
Cr	PETJ	Chromium Oxide	199
Na	TAP	Jadeite	114
Cs	PETJ	Pollucite	336
K	PETH	Sanidine	66
Mn	PETJ	Bustamite	252
Mg	TAP	Chlorite	103
Zn	LIF	Sphalerite	568
Fe	LIFH	Almandine	187
Al	TAP	Chlorite	120
Ni	LIF	Nickel Sulfide	403
Ba	LIFH	Benitoite	423
		EPIDOTE	
Ta	LIF	LiTa03	1571
Nd	LIF	REE 6	640
Sm	LIF		1404
Pr	LIF		4513
Y	TAP	Yttrium Al Garn	498
Si	TAP	Bustamite	193
Mg	TAP	Diopside	160
Na	TAP	Jadeite	169

F	TAP		1690
Al	TAP		171
Mn	PETJ	Bustamite	396
Ce	PETJ	Monazite	615
La	PETJ	Monazite	668
Ti	PETJ	Rutile	337
Ca	PETJ	Bustamite	188
Nb	PETJ	LiNbO3	640
Fe	LIFH	Haematite	291
Cr	LIFH	Crocoite	270
V	LIFH	V	299
Ba	LIFH	Benitoite	564
Th	PETH	Monazite	390
Zr	PETH	Zirconia	271
	ZIRCON		
La	PETJ	Monazite	444
Ca	PETJ	Apatite	165
Ti	PETJ		233
Al	TAP	Almandine	154
Mg	TAP	Periclase	114
F	TAP		909
Zr	TAP		393
Ce	LIF	Monazite	1237
Th	PETJ	Monazite	1016
P	PETJ	Apatite	372
Fe	LIFH	Almandine	239
Nd	LIFH	REE 6	434
Hf	LIFH		610
Si	PETH		195
	TITANITE		
Ta	LIF	LiTa03	1162
Sm	LIF	REE 2	993
Pr	LIF	Monazite	2272
Nd	LIF	REE 6	736
Ce	LIF	Monazite	1131
Si	TAP	Bustamite	134
Al	TAP	Plagioclase	100
Mg	TAP	Periclase	90
Na	TAP	Jadeite	115
F	TAP		766
Mn	PETJ	Bustamite	265
La	PETJ	Monazite	468
Ti	PETJ	Rutile	247
Ca	PETJ	Diopside	153
Nb	PETJ	LiNbO3	457
Fe	LIFH	Haematite	183
Cr	LIFH	Chromium Oxide	189
V	LIFH	V	186
Ba	LIFH	Barite	452
K	PETH	Sanidine	66
Zr	PETH	Zirconia	207
	CARBONATE		
Mg	TAP	Almandine	122
Ca	PETJ	Calcite	146
Fe	LIFH	Magnetite	213
Mn	PETJ	Bustamite	290
Zn	LIFH	Sphalerite	390
Sr	PETH	Celestite	234
Ba	PETJ	Barite	441
Na	TAP	Jadaite	107
Ti	PETJ	Rutile	236
Ce	PETJ	Monazite	515
La	PETJ	Monazite	459
	APATITE		
F	TAP	Apatite	871
Sr	PETJ	Celestite	605
P	PETH	Apatite	131
Nd	PETJ	REE 6	417
Na	TAP	Jadeite	124
Ce	LIF	Monazite	964
Ca	PETH	Diopside	77
Mn	PETJ	Bustamite	249
Mg	TAP	Periclase	87
Cl	PETJ	Tugtupite	96
Fe	LIFH	Almandine	191
	RUTILE		

P	PETJ	Apatite	301
Na	TAP	Jadeite	111
S	PETJ	Stibnite	234
Ba	LIFH	Benitoite	496
Bi	PETJ	Bismuth Selenide	690
Mg	TAP	Periclase	89
Pb	PETJ	Galena	457
V	LIFH	V	195
Ag	PETJ	Ag	282
As	TAP	Galium Arsenide	339
K	PETJ	Sanidine	137
Cr	LIFH	Chromium Oxide	202
Ca	PETJ	Diopside	158
Al	TAP	Plagioclase	100
Sn	PETJ	Cassiterite	361
Fe	LIFH	Haematite	201
Zn	LIF	Willemite	637
Si	TAP	Diopside	135
Ti	PETJ	Rutile	249
Ni	LIFH	Nickel Silicide	260
Ta	LIF	LiTaO3	1117
Zr	TAP	Zirconia	268
Mn	PETJ	Rhodonite	284
Cu	LIFH	Cuprite	304
Co	LIF	Skutterudite	302
Nb	TAP	Metallic Nb	293
W	LIF	Metallic W	1195
Au	PETH	Au	239
	SULFIDES		
S	PETH	Pyrite	99
Fe	LIFH	Pyrite	283
Cu	LIFH	Cuprite	470
Zn	LIF	Sphalerite	1040
Pb	PETJ	Galena	861
As	TAP	Galium Arsenide	344
Sb	PETJ	Stibnite	416
Ni	LIF	Pentlandite	594
Sn	PETJ	Metallic Sn	359
Co	LIFH	Skutterudite	288
Mn	PETJ	Bustamite	386
Au	PETH	Au	411
Ag	PETJ	Ag	359
Bi	PETJ	Bismuth Selenide	3931
Ge	TAP	Metallic Ge	291
Se	TAP	Bismuth Selenide	244
In	PETJ	Metallic In	414
Cd	PETJ	Cd	366
Mo	PETH	Molybdenite	594
Ga	TAP	Metallic Ga	241
Te	PETJ	CAL-STD	392

Appendix II Analytical data quality obtained from the use of a 316 stainless steel alloy as reference (n=18).

	316 SS (%)	Mean (%)	Diff (%)	RSD (%)
Si	1	0,584	-0,416	10,20
Al	0	2,347	2,347	5,48
Fe	65,345	62,156	-3,189	0,86
Mg	0	4,558	4,558	16,55
K	0	0,847	0,847	3,28
Ca	0	0,129	0,129	3,34
Mn	2	2,022	0,022	1,32
P	0,045	0,09	0,045	8,82
S	0,03	1,16	1,13	4,34
Cr	17	14,763	-2,237	0,62
V	0	0,03	0,03	8,56
Ni	12	8,784	-3,216	1,37
Cu	0	0,464	0,464	2,74
Mo	2,5	1,875	-0,625	1,37
W	0	0,11	0,11	5,46
Total	99,92	99,919	-0,001	

Appendix III %Diff median per element

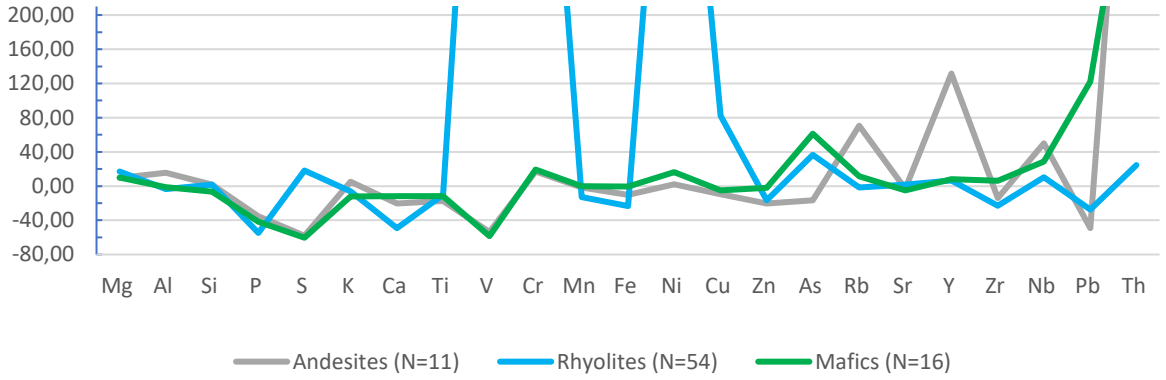

Appendix IV Correction factors for each element.

	%Diff median	Correction factor
Mg	17,16	0,85
Al	-3,62	1,04
Si	1,62	0,98
P	-54,76	2,21
S	18,25	0,85
K	-6,01	1,06
Ca	-49,21	1,97
Ti	-10,25	1,11
V	826,67	0,11
Cr	690,00	0,13
Mn	-12,82	1,15
Fe	-23,43	1,31
Ni	664,71	0,13
Cu	82,15	0,55
Zn	-16,70	1,20
As	36,36	0,73
Rb	-1,77	1,02
Sr	1,59	0,98
Y	6,65	0,94
Zr	-22,79	1,30
Nb	10,19	0,91
Pb	-27,51	1,38
Th	24,61	0,80

Appendix V List of all the polished thin sections studied, providing information on their geographical location, depth and classification.

Reference	**Coord. (**ETRS89 PT-TM06)	**Depth**	**Classification**
MM02#2	X:-6935; Y:-198314	450.00 m	Felsic Volcaniclastic
MM02#3	X:-6935; Y:-198314	460.00 m	Felsic Volcaniclastic
MM02#5	X:-6935; Y:-198314	471.30 m	Intrusive Mafic
MM02#6	X:-6935; Y:-198314	527.00 m	Intermediate Lava
Z1#9	X:-7856.40; Y:-197189.20	285.50 m	Rhyolitic Lava
Z2#15	X:-7436.40; Y:-197419.19	213.80 m	Rhyolitic Lava
Z2#16	X:-7436.40; Y:-197419.19	229.15 m	Felsic Volcaniclastic
Z2#18	X:-7436.40; Y:-197419.19	272.70 m	Felsic Volcaniclastic
Z2#19	X:-7436.40; Y:-197419.19	297.00 m	Dacitic(?) Lava
MM05#24	X=-7600; Y=-194450	88.00 m	Rhyolitic Lava
MM05#26	X=-7600; Y=-194450	131.45 m	Rhyodacitic Lava
MM05#28	X=-7600; Y=-194450	169.35 m	Volcaniclastic/Metapelite Contact
MM05#30	X=-7600; Y=-194450	212.15 m	Rhyodacitic Lava
MM05#31	X=-7600; Y=-194450	268.60 m	Intrusive Mafic
MM05#34	X=-7600; Y=-194450	94.20 m	Metapelite
MM05#36	X=-7600; Y=-194450	228.90 m	Intrusive Mafic
MM05#37	X=-7600; Y=-194450	258.25 m	Intrusive Mafic
MdM05#38	X:-7151.88; Y:-196917.85	70.50 m	Metapelite
MdM05#40	X:-7151.88; Y:-196917.85	155.00 m	Metapelite
MdM05#42	X:-7151.88; Y:-196917.85	530.75 m	Extrusive Mafic
MdM05#43	X:-7151.88; Y:-196917.85	579.65 m	Rhyolitic/Dacitic Lava Contact
MdM05#44	X:-7151.88; Y:-196917.85	594.65 m	Intrusive Mafic
MdM05#45	X:-7151.88; Y:-196917.85	682.65 m	Intrusive Mafic
MdM05#49	X:-7151.88; Y:-196917.85	740.10 m	Felsic Volcaniclastic
MdM05#50	X:-7151.88; Y:-196917.85	802.05 m	Rhyodacitic Lava
MdM05#51	X:-7151.88; Y:-196917.85	848.60 m	Rhyodacitic Lava
MdM05#52	X:-7151.88; Y:-196917.85	863.10 m	Metapelite
MdM05#53	X:-7151.88; Y:-196917.85	888.75 m	Rhyolitic Lava
MdM01#54	X:-8189.26; Y:-193427.02	41.00 m	Felsic Volcaniclastic
MdM01#58	X:-8189.26; Y:-193427.02	261.00 m	Felsic Volcaniclastic
MdM01#59	X:-8189.26; Y:-193427.02	293.35 m	Rhyolitic Lava
MdM01#60	X:-8189.26; Y:-193427.02	307.15 m	Felsic Volcaniclastic
MdM01#64	X:-8189.26; Y:-193427.02	365.90 m	Rhyolitic Lava
MdM01#65	X:-8189.26; Y:-193427.02	373.80 m	Felsic Volcaniclastic
MdM01#68	X:-8189.26; Y:-193427.02	566.80 m	Felsic Volcaniclastic
MdM01#69	X:-8189.26; Y:-193427.02	597.65 m	Rhyolitic Lava
MdM01#70	X:-8189.26; Y:-193427.02	610.10 m	Rhyolitic Lava
MdM02#71	X:-9154.87; Y:-193552.26	117.80 m	Felsic Volcaniclastic
MdM02#72	X:-9154.87; Y:-193552.26	138.60 m	Metapelite
MdM02#74	X:-9154.87; Y:-193552.26	253.40 m	Rhyolitic Lava
MdM02#76	X:-9154.87; Y:-193552.26	163.80 m	Felsic Volcaniclastic
MdM02#80	X:-9154.87; Y:-193552.26	501.00 m	Rhyolitic Lava

Appendix VI List of the 80 samples collected from the observed drill-cores along with a synthetic description of their prevalent macroscopic features and indication of the selection done for subsequent petrography work (29 polished thin-sections).

Sample	Synthetic Description (macroscopic features)
MM01#1 535.00 m	Purple metapelite with significant fine-grained sandy component (mostly feldspar and quartz – volcanogenic contribution?). Very deformed inter-fingered layer of dark-colored metapelite.
MM02#2 320.75 m Polished thin-section	Grey, volcaniclastic felsic rock slightly foliated. Fine-grained matrix, commonly dark-grey to black in color, conceivably dominated by sericite and chlorite but including as well quartz and feldspar clasts besides disseminated (euhedral and anhedral) pyrite grains.
MM02#3 451.00 m Polished thin-section	Mostly dark-green metapelite with lighter inter-fingered layers due to unequal abundance of chlorite, epidote and fine-grained mica components. Common carbonate vesicle infillings in the matrix and in lenses subparallel to foliation. Very fine, hematitic venules also running subparallel to foliation.
MM02#4 453.85 m	Dark-green intrusive mafic rock slightly foliated. The dark-green color is due to intense sericitization and chloritization. Presence of fine-grained feldspar and amphibole(?); also disseminated carbonates and very fine and rare hematite.
MM02#5 471.20 m Polished thin-section	Dark-green intrusive mafic foliated rock similar to MM02#4 although slightly darker in color; plus some epidote. Very fine and rare disseminated sulfides (pyrite?). Carbonate lenses subparallel to foliation.
MM02#6 526.89 m Polished thin section	Light-green, coherent intermediate rock. Very fine and rare sulfides (pyrite?). The petrographic study confirmed this classification since accessory amounts of quartz are also present, despite the presence of pyroxene and amphibole relics, supporting its classification as intermediate
Z1#7 199.80 m	Fine, compact and homogeneous green colored rock enriched in epidote and chlorite, presenting some degree of silicification. Pillow-lava structure (?). Spilite(?). Enriched in carbonate, fine hematite and (mm) subhedral pyrite.
Z1#8 263.05 m	Light-grey, felsic volcanic rock with quartz and feldspar phenocrysts (rhyolite?). Very rare and fine sulfides (pyrite?).
Z1#9 285.50 m Polished thin-section	Rhyolitic lava presenting brecciated texture due to chlorite (± carbonate) veining in which some domains are enriched in massive pyrrhotite ± pyrite. Also, moderate disseminations in rock groundmass of pyrrhotite ± pyrite.
Z1#10 294.80 m	Dark green-grey, volcaniclastic felsic foliated rock. Abundant quartz and feldspar mineraloclasts. Sericite and chlorite rich matrix. Sulfides (pyrrhotite + pyrite) weakly disseminated.
Z1#11 321.50 m	Green, fine-grained mafic volcanic rock. Sericite (sericitization), feldspar and titanite (?) are the main components. Frequent dark chlorite aggregates. Trace amounts of very fine disseminated sulfides (possibly pyrrhotite) mostly texturally related to chlorite.
Z1#12 401.30 m	Green, medium-grained mafic volcanic rock. Sericite, chlorite, feldspar and titanite(?) and some trace amounts of very fine disseminated sulfides (possibly pyrrhotite). Similar to Z1#11 but coarser grained.
Z2#13 169.40 m	Green, very fine-grained mafic volcanic rock. Sericite, feldspar, chlorite and titanite(?) are the main components. Frequent fine, dark-tabular chlorite grains also occur. Trace amounts of very fine disseminated sulfides (possibly pyrrhotite). Very similar to Z1#11 however finer grained.
Z2#14 173.50 m	Green, medium-grain mafic volcanic rock. Feldspar, titanite(?) and biotite form the original rock that appears to be obliterated by an anastomosed mesh of sericite and chlorite. Very similar to Z1#12.
Z2#15 213.80 m Polished thin-section	Dark-grey felsic volcanic rock (rhyolitic lava). Silica rich matrix with abundant feldspar ± quartz phenocrysts. Several feldspar generations. Sericitization of feldspars from the core domains. Elongated, dark chlorite tracing a poor-developed foliation. Very fine and rare sulfides (pyrite ± pyrrhotite).
Z2#16 229.15 m Polished thin-section	Dark-brownish, slightly foliated volcaniclastic felsic rock. With feldspar ± quartz mineraloclasts. Broken feldspars, some sericitized. Quartz veining. Dark chlorite veining. Sulfides, pyrite + pyrrhotite, disseminated but mostly in masses associated with the chlorite veining and along fractures.
Z2#17 246.00 m	Grey felsic volcanic rock (rhyolite?). Feldspar + quartz phenocrysts. Feldspars are cut by small chorite + sericite veinlets and some phenocrysts show effects of sericitization. Dark elongated chlorite is frequent. Matrix enriched in sericite and chlorite.
Z2#18 272.65 m Polished thin-section	Light-grey, foliated volcaniclastic felsic rock. Feldspar + quartz mineraloclasts ± titanite. Sericitization of the feldspars. Intercalation between domains unequally rich in sericite, resulting in a “chromatic layering”.
Z2#19 296.90 m Polished thin-section	Light green-grey felsic volcanic rock (thin section observation points to a more dacitic composition). Feldspar phenocrysts corroded and showing sericite-rich envelops. Small, dark chlorite aggregates; within rock groundmass, the relative abundance of chlorite increases along discontinuities tracing structural weaknesses. Very rare disseminated pyrite.

Z2#20 302.00 m	Green, fine-grained mafic volcanic rock strongly sericitized and chloritized. Frequent small pyrrhotite aggregates disseminated in the rock groundmass and within carbonate + chlorite + sericite veinlets.
Z2#21 330.50 m	Green, medium-grained mafic volcanic rock strongly sericitized and chloritized. Rare disseminations of very fine pyrrhotite.
Z2#22 362.80 m	Dark grey, fine-grained volcaniclastic felsic rock. Feldspar clasts some of them showing effects of hydrolysis. Matrix enriched in chlorite and sericite. Fine-grained, euhedral pyrite disseminated in the rock groundmass, usually forming millimeter-sized aggregates. Pyrrhotite(?) venules.
MM05#23=MM05#33 67.30 m	Green, medium-grained mafic volcanic rock showing evidence of strong sericitization and chloritization. The primary mineral assemblage is still recognizable, including biotite and feldspar. Dissemination of very fine-grained sulfides.
MM05#24 88.00 m Polished thin-section	Light green-grey, fine-grained volcanic felsic rock. Small feldspar + quartz + titanite phenocrysts in sericite rich, slightly foliated, matrix. Quartz + chlorite veining. Very fine chlorite venules tracing the foliation. Fractures subparallel to foliation with occasional tiny sulfides.
MM05#25=MM05#35 107.00 m	Dark grey metapelite displaying a significant sandy (volcanogenic?) component, mostly feldspar and quartz in a sericite and chlorite enriched groundmass. Fine sulfides (pyrite) along foliation.
MM05#26 131.46 m Polished thin-section	Light-green, fine-grained felsic volcanic (dacitic?) rock with brecciated texture. Small phenocrysts of feldspar ± quartz. Strong chloritization. The brecciated texture is due to chlorite veining, especially along fractures.
MM05#27 162.30 m	Inter-fingering between black and grey metapelite with significant fine-grained sandy component, mostly feldspar and quartz (volcanogenic contribution?). Very deformed sample. Pyrite lenses/nodules and disseminated pyrite along foliation.
MM05#28 169.35 m Polished thin-section	Depositional contact between a volcaniclastic rock and a black metapelite enriched in a possible volcanogenic component (displaying a sericite-/chlorite-rich matrix). The possible volcanogenic component is composed of fragmented (white and pink) feldspar and quartz clasts. Fine-grained pyrite "masses" are disseminated along the black metapelite. Silica rich veining is frequently accompanied by very fine-grained sulfides (pyrite ± pyrrhotite?)
MM05#29 179.60 m	Dark metapelite with significant (possible) volcanogenic contribution. Quartz and feldspar fragmented mineraloclasts with alteration halos. Foliated. Sericite and chlorite enriched matrix.
MM05#30 212.15 m Polished thin-section	Light colored and fine-grained felsic volcanic rock with brecciated texture. Very small phenocrysts of feldspar. Abundant titanite. Strong chloritization. The brecciated texture is due to chlorite veining, especially along fractures. Pyrite is disseminated but mostly along the chlorite veining. Depositional contact with black metapelite.
MM05#31 268.30 m Polished thin-section	Green, medium-grained mafic intrusive rock. Feldspar is the most abundant mineral + amphibole. Effects of moderate chloritization and sericitization. Fine-grained sulfides (pyrite ± pyrrhotite ± chalcopyrite) usually associated to the black mineral – chlorite. Chlorite veining.
MM05#32 324.80 m	Purple metapelite locally discolored, mainly along discontinuities representing structural weaknesses. Rare pyrite lenses.
MM05#34 94.20 m Polished thin-section	Dark grey metapelite with very fine-grained sandy component, mostly feldspar + quartz (volcanogenic contribution?). Evident deformation. Pyrite is very abundant, disseminated along foliation planes and along deformed venules.
MM05#36 228.90 m Polished thin-section	Dark-green mafic volcanic rock. Evidence of strong chloritization and sericitization. Very similar to sample MM05#37.
MM05#37 258.25 m Polished thin-section	Green, medium- to fine-grained mafic volcanic rock. Abundant feldspar and a pyroxene frequently altered (amphibole?). Evidence of strong chloritization and sericitization. No sulfides. Possibly related to MM05#31 but recording effects of more intense alteration.
MdM05#38 70.50 m Polished thin-section	Brownish metapelite (weathered?). Fine-grained sandy component and carbonate venules. Highly deformed (folded and fractured).
MdM05#39 154.00 m	Black metapelite including a very fine-grained sandy component (detritus or volcanogenic??). Abundant fine pyrite disseminated in the matrix and along foliation. Quartz (± calcite) veining with abundant pyrite (sometimes euhedral); these discontinuities are subparallel to foliation and frequently folded.
MdM05#40 155.00 m Polished thin-section	Black metapelite with strong disseminated medium to fine-grained pyrite. Quartz + pyrite ± calcite venules displaying incipient effects of boudinage.
MdM05#41 513.40 m	Medium to fine-grained green rock enriched in epidote and chlorite. Possible pillow-lava structure (?). Frequent (vesicle?) carbonate infillings(?). Purplish-reddish domains due to hematite dissemination (?). Alteration effects conceivably due to the progression of oceanic metasomatism.
MdM05#42 530.75 m Polished thin-section	Fine-grained green rock enriched in epidote and chlorite. Abundant carbonate and purplish-reddish domains possible due to hematite dissemination. Similar to MdM-05#41 however darker (richer in chlorite and less epidote?).

MdM05#43 579.65 m Polished thin-section	Contact between a felsic volcanic rock and a very fine-grained mafic rock (petrography confirmed two different compositions, but the latter is dacitic). The rhyolitic rock has a silica-rich groundmass that becomes more sericitic and chloritic towards the top. Contacts with a very fine-grained altered dacitic rock (feldspar + titanite) with brecciated texture and frequent pyrite in fractures. Carbonate + quartz + chlorite veining that crisscrosses both rock types.
MdM05#44 594.65 m Polished thin-section	Fine-grained green mafic volcanic rock mostly composed of feldspar + titanite(?) + chlorite + sericite. Small rounded chlorite aggregates frequently accompanied by pyrrhotite. Common calcite ± chlorite venules with massive pyrrhotite aggregates; the development of these venules is conceivably controlled by preexistent structural weaknesses.
MdM05#45 682.65 m	Fine-grained, mafic coherent volcanic rock affected by an anastomosed network that determines the relative intensity of sericitization ± chloritization. Chlorite + pyrrhotite within fractures.
MdM05#46 693.55 m	Medium to fine-grained mafic coherent volcanic rock. Primary feldspar + titanite ± biotite are still recognizable. Strong sericitization ± chloritization enveloping the anastomosed network. Weak dissemination of pyrrhotite disseminated within fractures. Similar to MdM-05#45 but coarser and less altered.
MdM05#47 720.30 m	Fine-grained mafic coherent volcanic rock. Primary feldspar + titanite ± biotite still recognizable. Two generations of feldspar. Calcite + sericite + chlorite ± pyrrhotite venules. Small rounded chlorite aggregates. Weak dissemination of very fine-grained pyrrhotite. Probably even less altered rock than MdM-05#46.
MdM05#48 733.10 m	Light-green, felsic foliated volcaniclastic rock. Broken feldspar (±quartz) clasts displaying evidence of hydrolysis. Strong sericitization ± chloritization. Milky quartz veining along foliation showing morphological irregularities ascribable to incipient boudinage.
MdM05#49 740.10 m Polished thin-section	Dark green-greyish felsic foliated volcaniclastic rock. Broken feldspar (±quartz) clasts displaying evidence of hydrolysis. Strong sericitization ± chloritization.
MdM05#50 802.05 m Polished thin-section	Light greyish volcanic rock slightly foliated (petrography points to a rhyodacitic to dacitic lava composition). Feldspar (± quartz) phenocrysts with evident sericitization. Two feldspar generations. Abundant titanite. Sericitization ± chloritization. Very rare and small disseminated pyrite + pyrrhotite.
MdM05#51 848.60 m Polished thin-section	Very light colored felsic volcanic rock. Mostly feldspar + quartz phenocrysts in a sericite-rich groundmass crossed by an anastomosed fracture mesh of chlorite ± pyrrhotite that yields brecciated-like texture.
MdM05#52 Polished thin-section	Gradual contact between a very fine metapelite rich in very small (possibly) volcanogenic clasts and a volcaniclastic rock with coarser and more abundant quartz and feldspar clasts of the same origin. Very fine sulfides (pyrite) disseminated and along foliation.
MdM05#53 Polished thin-section	Grey to blueish volcanic rock (petrography points to a rhyolitic composition). Silica rich groundmass with quartz + feldspar porphyroblasts.
MdM01#54 40.75 m Polished thin-section	Felsic volcaniclastic rock with feldspar + quartz mineraloclasts. Feldspar clasts are broken and show evidence of sericitization. Strong sericitization and chloritization. Quartz +chlorite veining that crisscross the secondary mineral assemblage tracing a previous alteration event.
MdM01#55 48.95 m	Dark green-grey felsic volcanic rock with feldspar + quartz phenocrysts in a silica rich groundmass. Chlorite + sericite + quartz infillings of discrete fractures. Delicate dissemination of tiny sulfides (pyrrhotite?).
MdM01#56 78.90 m	Reddish (oxidized/weathered?) felsic volcaniclastic rock mostly composed of rounded feldspar and quartz mineraloclasts and recording silicification of moderate intensity. Significant, late (post-silicification) chlorite + quartz veining.
MdM01#57 169.80 m Polished thin-section	Dark-grey to black metapelite including a significant sandy component, mostly feldspar and quartz, possibly distal volcanogenic contribution. Very fine and weak pyrite ± chalcopyrite.
MdM01#58 260.90 m Polished thin-section	Black (folded) volcaniclastic rock preserving inter-fingerings between domains with very little and fine volcanogenic component and very fine-grained pyrite along foliation and domains richer in coarser quartz and feldspar (white to pinkish) clasts. The latter domains are also enriched in pyrite, however developing larger and massive colomorphic aggregates. Quartz + pyrite venules subparallel to foliation can also be observed.
MdM01#59 293.25 m Polished thin-section	Green-grey felsic volcanic rock (rhyolitic lava). Small feldspar phenocrysts in a silica rich groundmass crisscrossed by small fractures with very fine-grained oxidized sulfides. Abundant carbonates.
MdM01#60 307.05 m Polished thin-section	Grey felsic volcaniclastic rock with small feldspar + quartz clasts in a silica and sericite enriched matrix. Disseminations of tiny pyrite grains can be observed, often following a preferential orientation.
MdM01#61 322.70 m	Green-grey, coherent felsic volcanic rock (rhyolitic lava?). Feldspar and quartz phenocrysts in a silica-dominant groundmass. Some feldspars show evidence of sericitization. Chlorite infillings of very small fractures (locally resembling a brecciated texture) accompanied by fine pyrite.
MdM01#62 355.95 m	Grey, coherent felsic volcanic rock (rhyolitic lava?). Feldspar phenocrysts in a silica rich groundmass locally including sericite and chlorite.
MdM01#63 360.70 m	Grey, coherent felsic volcanic rock (rhyolitic lava?). Feldspar phenocrysts in a silica rich groundmass locally including sericite and chlorite. Quartz + chlorite veining.

MdM01#64 365.80 m Polished thin-section	Light grey, felsic volcanic rock (rhyolitic lava). Feldspar phenocrysts in a silica rich groundmas locally including sericite and chlorite. Quartz veining. Carbonates along fractures.
MdM01#65 373.00 m Polished thin-section	Grey, coherent felsic volcanic rock. Feldspar phenocrysts in a silica rich groundmass. Centimeter-thick chlorite-rich vein. Smaller feldspar + quartz + chlorite ± pyrite veining along with minor fractures that also cut cross the large chlorite vein. (Thin-section observation showed that the "chlorite-rich vein" is actually a contact with a different volcanic rock highly altered, which made impossible to infer its protolith.)
MdM01#66 427.15 m	Fine-grained, mafic, coherent volcanic rock. Primary feldspar + titanite ± biotite are still recognizable. Sericitization and chloritization of moderate intensity. Chlorite aggregates, sericite and carbonates forming the prevalent fracture infillings. Weak dissemination of fine-grained sulfides (pyrrhotite ± pyrite).
MdM01#67 477.95 m	Coarse-grained, mafic, coherent volcanic rock. Primary feldspar + titanite ± biotite still recognizable. Sericitization and chloritization of moderate intensity. Chlorite fracture infillings. Frequent disseminated pyrrhotite. Similar to MdM-01#66 but coarser-grained.
MdM01#68 566.80 m Polished thin-section	Green-grey, felsic volcaniclastic rock. Feldspar ± quartz clasts in a sericite-rich matrix. Fine-grained pyrrhotite + pyrite + sphalerite + galena within quartz veins and forming fracture infillings.
MdM01#69 597.65 m Polished thin-section	Rhyolitic lava with quartz + feldspar phenocrysts. Evidence of sericitic and carbonate alteration. Sulfides (pyrite + galena + sphalerite) along fractures.
MdM01#70 610.00 m Polished thin-section	Grey, felsic volcanic rock (rhyolite) with feldspar ± quartz phenocrysts in a sericitized matrix. Very fine-grained sulfides (pyrite) forming small aggregates, mostly as infillings of small fractures but also along (incipient developed) foliation planes.
MdM02#71 117.70 m Polished thin-section	Felsic volcaniclastic rock with rounded to angular broken and sericitized feldspar grains, quartz and clasts within a green phyllosilicate enriched matrix (possibly due to strong chloritization ± sericitization). The reddish (hematite rich) domains are richer in very fine-grained sulfides (pyrite ± arsenopyrite).
MdM02#72 138.45 m Polished thin-section	Apparent brecciated texture with variable size "clasts" of a very fine-grained felsic rock (mostly a quartz groundmass and some tiny quartz phenocrystals) involved in a black phyllosilicate-rich cement; no penetrative schistosity can be observed. Very rare and fine-grained pyrite associated with the phyllosilicate-rich cement, but also in fracture infillings. Quite small, late veinlets showing white to pink carbonates can also be observed.
MdM02#73 180.05 m	Rhyolitic lava with quartz (±feldspar white and beige) phenocrystals in a silica-rich groundmass. The feldspars display corroded/reabsorbed rims. Very small beige-yellow secondary mineral phase (neoformed feldspar?). Very small chlorite(?) aggregates filling discrete (micro)fractures.
MdM02#74 253.30 m Polished thin-section	Rhyolitic lava with quartz (±feldspar) phenocrystals in a beige-colored, silica rich matrix. Chlorite along discrete (micro)fractures; very fine and rare pyrite associated with chlorite aggregates. Late quartz veins including a beige-colored carbonate phase and a green-yellow "saccharide" mineral (?)
MdM02#75 259.05 m	Rhyolitic lava with feldspar and quartz phenocrystals in a silica rich groundmass. Very fine and weakly disseminated pyrite. Very fine-grained chlorite sealing fractures. Yellowish, secondary feldspar(?). Late veining enriched in quartz and calcite also with chlorite and a yellow-orange (some kind of carbonate?). Possibly, a less altered protolith of MdM02#74.
MdM02#76 163.60 m Polished thin-section	Grey, felsic and strongly foliated volcaniclastic rock with broken and rounded feldspar + quartz clasts in a phyllosilicate rich (sericite) matrix. Minor amounts of magnetite developing arrays subparallel to foliation whose late oxidation (hematite) might justify the reddish-colored layers also affected by foliation.
MdM02#77 310.80 m	Rhyolitic lava with feldspar phenocrystals. Early stages of fracture-infillings traced by chlorite and sericite, locally developing spatial arrays resembling a brecciated texture. Late vein infillings of quartz + calcite + chlorite + (very oxidized) sulfide(?) + pyrite. Sub-idiomorphic grains of pyrite disseminated in the rock groundmass (controlled by discrete fractures or other kind of secondary discontinuities?). Secondary yellowish feldspar(?).
MdM02#78 479.45 m	Rhyolitic lava with feldspar phenocrystals. Small fractures filled with quartz + chlorite + sericite(?). Alteration effects less evident than those observed in MdM02#77; possibly closer to the protolith.
MdM02#79 490.55 m	Felsic volcanic rock (rhyolite?) including abundant rounded quartz phenocrysts along with abundant and strongly sericitized felspar phenocrysts in a phyllosilicate rich matrix (sericite + chlorite) (alteration).
MdM02#80 499.80 m Polished thin-section	Rhyolitic lava with small quartz and feldspar phenocrystals in silica a rich groundmass. Fine veining network, locally developing a brecciated texture and including discontinuities filled with quartz, sericite and very fine-grained sulfides (pyrite ± chalcopyrite).

Appendix VII Representative analysis of the Feldspar group in a.p.u.f.

	Feldspato			
	Plagioclase		Feldspato-K	
Ti4+	0.000	0.000	0.000	0.000
Si4+	3.010	3.020	3.003	3.015
Fe3+	0.000	0.000	0.000	0.000
Al3+	0.990	0.970	0.993	0.977
Fe2+	0.000	0.010	0.001	0.001
Total	4.000	4.000	3.997	3.992
Ba2+	0.000	0.000	0.002	0.004
Sr2+	0.000	0.000	0.000	0.000
Fe2+	0.000	0.000	0.000	0.000
Ca2+	0.010	0.010	0.002	0.005
Mg2+	0.000	0.000	0.000	0.000
K+	0.010	0.000	0.983	0.980
Na+	0.970	0.980	0.013	0.012
Total	0.990	0.990	1.001	1.001

Appendix VIII Representative analysis of the Pyroxene group in a.p.u.f.

	Pyroxene	
Si4+	1.880	1.896
Al3+	0.120	0.105
Total	2.000	2.000
Ti4+	0.005	0.000
Cr3+	0.008	0.004
Ti3+	0.045	0.046
Al3+	0.081	0.079
Fe2+	0.099	0.111
Mg2+	0.761	0.760
Total	1.000	1.000
Fe2+	0.122	0.121
Mn2+	0.004	0.005
Ca2+	0.850	0.850
Na+	0.025	0.024
Total	1.000	1.000

Appendix IX Representative analysis of the Amphibole group in a.p.u.f.

	Amphibole	
Si4+	7.973	7.864
Al3+	0.027	0.136
Total	8.000	8.000
Ti4+	0.003	0.002
Fe3+	0.000	0.020
Cr3+	0.036	0.034
Al3+	0.170	0.087
Zn2+	0.005	0.008
Fe2+	1.299	1.090
Mn2+	0.023	0.010
Mg2+	3.383	3.749
Total	4.917	5.000
Mn2+	0.000	0.015
Ca2+	1.971	1.960
Na+	0.030	0.024
Total	2.000	2.000
K+	0.009	0.008
Na+	0.008	0.011
Total	0.018	0.019

Appendix X Representative analysis of the Mica group in a.p.u.f.

	Pre-deformation mica		Post-deformation mica	
Si4+	3.336	3.288	3.334	3.349
Al3+	0.664	0.712	0.667	0.651
Total	4.000	4.000	4.000	4.000
Ti4+	0.018	0.021	0.009	0.011
Cr3+	0.019	0.025	0.004	0.003
Al3+	1.581	1.574	1.571	1.599
Fe2+	0.205	0.218	0.234	0.207
Mg2+	0.200	0.204	0.218	0.193
Total	2.023	2.042	2.038	2.016
Ba2+	0.000	0.003	0.001	0.003
Ca2+	0.007	0.006	0.000	0.003
K+	0.957	0.966	0.980	0.98
Na+	0.009	0.006	0.015	0.008
Total	0.973	0.980	0.996	0.996

Appendix XI Representative analysis of the Chlorite group in a.p.u.f.

	Pre-deformation chlorite		Post-deformation chlorite	
	Mg rich	Fe Rich		
Si4+	2.916	2.797	2.869	2.836
Al3+	1.084	1.203	1.131	1.164
Total	4.000	4.000	4.000	4.000
Ti4+	0.000	0.003	0.000	0.000
Cr3+	0.007	0.010	0.005	0.009
Al3+	1.125	1.281	1.143	1.175
Ba2+	0.000	0.001	0.002	0.000
Zn2+	0.002	0.003	0.003	0.001
Ni2+	0.005	0.002	0.000	0.002
Fe2+	1.179	3.765	1.569	1.523
Mn2+	0.009	0.036	0.022	0.022
Ca2+	0.005	0.000	0.003	0.002
Mg2+	3.642	0.852	3.245	3.256
K+	0.002	0.000	0.001	0.001
Na+	0.002	0.000	0.000	0.000
Total	5.977	5.953	5.992	5.991

Appendix XII Representative analysis of the epidote group in a.p.u.f.

	Epidote	
Si4+	2.964	2.9429
Al3+	0.036	0.0571
Total	3.000	3.000
Zr4+	0.001	0.000
Ti4+	0.001	0.002
Fe3+	0.340	0.516
Mn3+	0.003	0.003
Cr3+	0.001	0.000
V3+	0.004	0.006
Al3+	2.653	2.471
Fe2+	0.000	0.000
Mn2+	0.000	0.000
Mg2+	0.003	0.007
Total	3.005	3.005
Ta5+	0.004	0.000
Nb5+	0.000	0.000
Th4+	0.000	0.000
Sm3+	0.000	0.000
Nd3+	0.000	0.002
Pr3+	0.000	0.002
Ce3+	0.000	0.002
La3+	0.000	0.002
Ba2+	0.000	0.001
Zn2+	0.001	0.004
Mn2+	0.000	0.000
Ca2+	2.000	2.004
Na+	0.002	0.003
Total	2.007	2.020

Appendix XIII Representative analysis of the zircon group in a.p.u.f.

	Zircon	
P5+	0.035	0.029
Si4+	4.022	4.034
Total	4.057	4.062
U6+	0.000	0.002
Th4+	0.001	0.006
Hf4+	0.042	0.038
Zr4+	3.881	3.877
Ti4+	0.001	0.000
Nd3+	0.003	0.000
Ce3+	0.005	0.000
La3+	0.001	0.000
Fe3+	0.004	0.004
Al3+	0.000	0.000
Mn2+	0.000	0.001
Ca2+	0.001	0.004
Mg2+	0.001	0.000
Total	3.939	3.933

Appendix XIV Representative analysis of the titanite group in a.p.u.f.

	Titanite	
Si4+	3.9304	4.021
Al3+	0.070	0.000
Total	4.000	4.021
Zr4+	0.003	0.008
V4+	0.004	0.006
Ti4+	2.580	2.602
Fe3+	0.079	0.126
Mn3+	0.000	0.001
Cr3+	0.001	0.000
Al3+	1.312	1.195
Total	3.980	3.937
Ta5+	0.001	0.000
Nb5+	0.009	0.011
Sm3+	0.000	0.002
Nd3+	0.001	0.012
Pr3+	0.000	0.000
Ce3+	0.000	0.009
La3+	0.000	0.002
Ba2+	0.007	0.005
Zn2+	0.000	0.000
Fe2+	0.000	0.000
Mn2+	0.000	0.000
Ca2+	4.053	3.986
Mg2+	0.000	0.017
K+	0.000	0.009
Na+	0.001	0.005
Total	4.070	4.060

Appendix XV Representative analysis of the carbonate group in a.p.u.f.

	Carbonate					
	Calcite		**Siderite**		**Dolomite-Ankerite**	
C4+	1.000	1.000	1.000	1.000	1.019	1.015
Total	1.000	1.000	1.000	1.000	1.019	1.015
Ba2+	0.000	0.000	0.000	0.000	0.000	0.000
Sr2+	0.000	0.000	0.0001	0.000	0.000	0.000
Zn2+	0.000	0.000	0.0003	0.0004	0.000	0.000
Fe2+	0.001	0.003	0.657	0.6601	0.187	0.188
Mn2+	0.001	0.031	0.0124	0.0121	0.007	0.008
Ca2+	0.998	0.953	0.0945	0.1009	0.542	0.550
Mg2+	0.000	0.012	0.2357	0.2265	0.225	0.223
Total	1.000	0.999	1.000	1.000	0.961	0.969
Ce3+	0.000	0.001	0.000	0.000	0.000	0.000
La3+	0.000	0.000	0.000	0.000	0.000	0.000
Na+	0.001	0.000	0.001	0.002	0.001	0.000
Total	0.001	0.001	0.0012	0.002	0.001	0.000

Appendix XVI Representative analysis of the apatite group in a.p.u.f.

	Apatite	
P5+	3.000	3.010
Total	3.000	3.010
Nd3+	0.000	0.010
Ce3+	0.000	0.010
La3+	0.000	0.000
Fe3+	0.000	0.000
Mn3+	0.000	0.000
Sr2+	0.000	0.000
Fe2+	0.000	0.080
Mn2+	0.000	0.010
Ca2+	5.000	4.830
Mg2+	0.000	0.020
Na+	0.000	0.020
Total	5.000	4.970

Appendix XVII Representative analysis of the rutile group in a.p.u.f.

	Rutile	
W6+	0.001	0.001
Ta5+	0.000	0.001
Nb5+	0.001	0.001
As5+	0.000	0.000
V5+	0.001	0.000
P5+	0.000	0.000
Pb4+	0.000	0.000
Sn4+	0.001	0.000
Zr4+	0.001	0.000
Mn4+	0.000	0.000
Ti4+	0.987	0.977
Si4+	0.003	0.010
Ce3+	0.000	0.000
Ni3+	0.000	0.000
Co3+	0.000	0.000
Fe3+	0.003	0.005
Cr3+	0.001	0.001
Al3+	0.001	0.005
Fe2+	0.000	0.000
Mn2+	0.000	0.000
Total	1.000	1.002
Ba2+	0.001	0.000
Zn2+	0.001	0.000
Cu2+	0.000	0.000
Ca2+	0.007	0.003
Mg2+	0.000	0.005
K+	0.001	0.001
Na+	0.000	0.000
Total	0.010	0.009

Appendix XVIII Representative analysis of the Pyrite group in a.p.u.f.

	Pyrite	
Bi-	0.000	0.000
Te-	0.000	0.000
Sb-	0.000	0.000
Se-	0.001	0.000
As-	0.001	0.001
S-	1.997	1.999
Total	1.998	2.000
Mo6+	0.000	0.001
Sn4+	0.000	0.000
Ge4+	0.000	0.000
In3+	0.000	0.000
Pb2+	0.001	0.000
Cd2+	0.001	0.001
Zn2+	0.000	0.006
Cu2+	0.000	0.000
Ni2+	0.001	0.000
Co2+	0.001	0.001
Fe2+	0.997	0.990
Mn2+	0.000	0.000
Au+	0.000	0.000
Ag+	0.001	0.000
Total	1.002	1.000

Appendix XIX Representative analysis of the pyrrhotite group in a.p.u.f.

	Pyrrhotite	
S6+	1.000	1.000
Total	1.000	1.000
As5+	0.000	0.000
Sn4+	0.000	0.000
Se4+	0.000	0.000
Ge4+	0.000	0.000
Sb3+	0.000	0.000
In3+	0.000	0.000
Fe3+	0.865	0.860
Pb2+	0.000	0.000
Cd2+	0.000	0.000
Zn2+	0.000	0.001
Cu2+	0.000	0.000
Ni2+	0.000	0.007
Co2+	0.001	0.003
Mn2+	0.000	0.000
Au+	0.000	0.000
Ag+	0.000	0.000
Total	0.867	0.872

Appendix XX Representative analysis of the sphalerite group in a.p.u.f.

	Sphalerite	
Te2-	0.000	0.000
Sb2-	0.000	0.000
Se2-	0.000	0.000
S2-	1.003	1.011
Total	1.003	1.011
Mo6+	0.001	0.001
As5+	0.000	0.000
Sn4+	0.000	0.000
Ge4+	0.000	0.000
Bi3+	0.000	0.000
In3+	0.000	0.000
Pb2+	0.001	0.000
Cd2+	0.002	0.003
Zn2+	0.933	0.967
Cu2+	0.000	0.001
Ni2+	0.000	0.000
Co2+	0.000	0.000
Fe2+	0.060	0.016
Mn2+	0.000	0.000
Au+	0.000	0.000
Ag+	0.000	0.001
Total	0.997	0.989

Appendix XXI Representative analysis of the Galena group in a.p.u.f.

	Galena	
Te2-	0.000	0.001
Sb2-	0.000	0.002
Se2-	0.000	0.000
S2-	0.994	1.001
Total	0.994	1.004
As5+	0.000	0.000
Sn4+	0.000	0.000
Ge4+	0.001	0.001
In3+	0.001	0.000
Ga3+	0.000	0.000
Pb2+	0.991	0.987
Zn2+	0.001	0.004
Cu2+	0.000	0.000
Ni2+	0.000	0.000
Co2+	0.000	0.000
Fe2+	0.011	0.000
Mn2+	0.000	0.003
Ag+	0.000	0.000
Total	1.006	0.996

Appendix XXII Representative analysis of the Chalcopyrite group in a.p.u.f.

	Chalcopyrite	
Pb2+	0.001	0.000
Co2+	0.001	0.000
Cu+	0.990	0.981
Total	0.991	0.981
Mo6+	0.002	0.001
As5+	0.000	0.000
Bi3+	0.000	0.001
Sb3+	0.000	0.000
In3+	0.001	0.000
Fe3+	1.000	0.992
Cd2+	0.000	0.000
Zn2+	0.002	0.002
Mn2+	0.001	0.000
Total	1.005	0.995